

**Supersymmetric Dark Matter in the NMSSM and  
 $E_6$ SSM**

**Sophie Underwood**

**A thesis submitted for the degree of Doctor of Philosophy**

**The University of Adelaide**

**May 2016**



---

# Declaration

---

I certify that this work contains no material which has been accepted for the award of any other degree or diploma in my name, in any university or other tertiary institution and, to the best of my knowledge and belief, contains no material previously published or written by another person, except where due reference has been made in the text. In addition, I certify that no part of this work will, in the future, be used in a submission in my name, for any other degree or diploma in any university or other tertiary institution without the prior approval of the University of Adelaide and where applicable, any partner institution responsible for the joint-award of this degree.

I give consent to this copy of my thesis, when deposited in the University Library, being made available for loan and photocopying, subject to the provisions of the Copyright Act 1968.

I also give permission for the digital version of my thesis to be made available on the web, via the University's digital research repository, the Library Search and also through web search engines, unless permission has been granted by the University to restrict access for a period of time.

Sophie Underwood

May 2016



---

# Acknowledgements

---

Thank you to my supervisors and colleagues - Anthony Thomas, Ross Young, Peter Athron, Martin White and Joel Giedt - for all of the help, advice, support and understanding that you have given me throughout my candidature. I also thank Lewis Tunstall, Nathan Hall and Ben Farmer for the conversations and advice on supersymmetry and coding we have shared with each other.

Thank you also to IT expert and wizard Ramona Adorjan for your help throughout the years, especially for recently recovering a failed hard disk!

Thank you to my many friends for the much-needed laughter, the video game and board game evenings, the hot chocolate breaks and the shoulder to lean on. Thank you to my family and family friends for your steady support (that includes my two beautiful cats Socks and Sheba, both now dearly departed and deeply missed after the end of their long lives, whose soothing presence and furry cuddles provided much comfort while I was writing this thesis).

My biggest thanks go to my amazing parents: my mum Donna Underwood for your endless and selfless love, nurturing and support, and Michèle Saint-Yves for your “warrior woman” guidance, wisdom and love. You have both made me the person that I am today, and I will always be incredibly grateful.



---

# Abstract

---

Supersymmetric extensions of the standard model may resolve the outstanding dark matter problem by producing viable dark matter candidates, including a stable weakly interacting particle called a neutralino. The next-to-minimal supersymmetric standard model (NMSSM) is first explored with a scan of the parameter space for neutralino-hadron scattering using an updated value for the strange quark sigma commutator.

This is followed by an extensive exploration of the parameter space of the  $E_6$ -inspired supersymmetric standard model ( $E_6$ SSM). It is demonstrated that this model still provides neutralino dark matter candidates that may be detected in the near-future by upcoming experiments, despite tightening experimental constraints.



---

# Contents

---

<b>Declaration</b>	<b>iii</b>
<b>Acknowledgements</b>	<b>v</b>
<b>Abstract</b>	<b>vii</b>
<b>1 Introduction</b>	<b>1</b>
<b>2 Dark Matter</b>	<b>5</b>
2.1 Experimental Evidence . . . . .	5
2.1.1 Zwicky’s ‘dunkle Materie’ . . . . .	5
2.1.2 Rotation curves . . . . .	6
2.1.3 Gravitational lensing . . . . .	8
2.1.4 The Cosmic Microwave Background . . . . .	9
2.2 Dark Matter Candidates . . . . .	12
2.2.1 MACHO Dark Matter . . . . .	12
2.2.2 Modified Newtonian Dynamics . . . . .	13
2.2.3 WIMP Dark Matter . . . . .	13
2.2.4 Other candidates . . . . .	14
2.3 Dark matter relic density . . . . .	14
2.4 Current Detection Efforts . . . . .	16
2.4.1 Direct Detection . . . . .	17
2.4.2 Indirect Detection . . . . .	21
2.5 Summary . . . . .	23
<b>3 The Standard Model</b>	<b>25</b>
3.1 Fundamental matter and forces . . . . .	25
3.1.1 Fermions . . . . .	27
3.1.2 Gauge bosons . . . . .	29

---

3.2	Electroweak symmetry breaking and the Higgs mechanism . . . . .	30
3.3	Outstanding problems of the standard model . . . . .	34
<b>4</b>	<b>Supersymmetry</b>	<b>37</b>
4.1	Poincaré algebra, No Go theorems and Supermultiplets . . . . .	37
4.2	Superspace and superfields . . . . .	40
4.3	Supersymmetry breaking . . . . .	44
4.3.1	$D$ -type supersymmetry breaking . . . . .	44
4.3.2	$F$ -type supersymmetry breaking . . . . .	45
4.3.3	Soft supersymmetry breaking . . . . .	46
4.4	The Minimal Supersymmetric Standard Model . . . . .	47
4.5	MSSM Lagrangian . . . . .	49
4.6	Neutralinos and charginos . . . . .	50
4.7	R-parity . . . . .	51
<b>5</b>	<b>The NMSSM</b>	<b>53</b>
5.1	The NMSSM . . . . .	54
5.2	Spin-independent neutralino-hadron cross section . . . . .	56
5.3	Results and Discussion . . . . .	59
<b>6</b>	<b>The <math>E_6</math>SSM</b>	<b>65</b>
6.1	The $E_6$ SSM . . . . .	66
6.1.1	$Z_2$ symmetries and the EZSSM . . . . .	68
6.1.2	Squarks, sleptons, gluinos and Higgsinos . . . . .	69
6.1.3	Neutralino and chargino mass mixing matrices . . . . .	70
6.1.4	Neutralino dark matter and previous benchmarks . . . . .	71
<b>7</b>	<b>Programs and Interfaces: micrOMEGAs, FlexibleSUSY and MultiNest</b>	<b>75</b>
7.1	micrOMEGAs . . . . .	75
7.2	FlexibleSUSY . . . . .	80
7.3	Interfacing FlexibleSUSY and MicrOMEGAs . . . . .	85
7.4	MultiNest . . . . .	86

---

<b>8</b>	<b>Results of the <math>E_6</math>SSM Parameter Scan</b>	<b>93</b>
8.1	The MultiNest Likelihood . . . . .	94
8.2	Experimental constraints . . . . .	95
8.3	Neutralino content mixing and masses . . . . .	104
8.4	Colour contours of SI cross sections . . . . .	109
8.5	Benchmark points and discussion . . . . .	112
8.5.1	<b>BM1</b> and <b>BM2</b> : inert Higgsino dark matter . . . . .	118
8.5.2	<b>BM3</b> and <b>BM4</b> : mixed Higgsino and inert Higgsino dark matter . .	119
8.5.3	<b>BM5</b> and <b>BM6</b> : Higgsino dark matter . . . . .	119
8.5.4	<b>BM7</b> , <b>BM8</b> and <b>BM9</b> : bino dark matter . . . . .	120
8.5.5	<b>BM10</b> , <b>BM11</b> and <b>BM12</b> : mixed bino, Higgsino and inert Higgsino dark matter . . . . .	120
8.5.6	Light neutralino dark matter . . . . .	121
8.6	Relic density discussion . . . . .	121
8.7	Outlook . . . . .	125
<b>9</b>	<b>Summary and outlook</b>	<b>133</b>
	<b>Bibliography</b>	<b>135</b>



---

# List of Figures

---

2.1	Expected rotation curve of a galaxy. . . . .	7
2.2	A plot from [5] displaying stellar mean velocities as a function of linear distance from the nucleus of 21 Sc galaxies. . . . .	7
2.3	The gravitational lensing effect [9]. . . . .	8
2.4	The bullet cluster, from [13]. The green lines are mass contours, indicating the presence of dark matter (observed by gravitational lensing). The white regions are two sources of hot, X-ray emitting plasma gas. . . . .	10
2.5	A map of the universe's temperature distribution from WMAP [17]. . . . .	10
2.6	Direct vs indirection detection [34]. . . . .	17
2.7	A schematic of the LUX detection chamber . . . . .	19
2.8	The predicted WIMP-nucleon elastic scattering rates for various target nuclei, from [54]. . . . .	20
2.9	Constraints on spin-independent WIMP-nucleon cross sections from the LUX experiment (figure from [55]). This is an update on 2013 limits on the WIMP-nucleon cross section from [56]. . . . .	20
2.10	From the Fermi LAT collaboration [57], this image is the result of a 5 year survey of the entire sky at gamma ray energies over 1 GeV. . . . .	21
3.1	A diagram illustrating quark color confinement. Attempting to pull two quarks apart results in the production of more bound quarks. . . . .	29
3.2	Feynman diagram depicting electron-electron scattering and virtual photon exchange. . . . .	30
3.3	The Mexican hat potential and modes of stability. . . . .	32
3.4	Running of the gauge couplings in the SM with energy [72]. It is hoped that a complete grand unified theory of physics will unify these forces at high energy. . . . .	36

---

4.1	Various potentials demonstrating the breaking (or not) of internal symmetries and SUSY . . . . .	45
5.1	A neutralino-nucleon collision via Higgs exchange. . . . .	57
5.2	Regions in the space of universal spin-1/2 and spin-0 masses allowed by relic density constraints. . . . .	60
5.3	Cross sections for the spin-independent neutralino-neucleon cross section for the parameter sets illustrated in Fig. 5.2(a) and Fig. 5.2(b). . . . .	61
7.1	micrOMEGAs, FlexibleSUSY and MultiNest working together. . . . .	76
7.2	Flow chart of micrOMEGAs. . . . .	77
7.3	Graphical illustration of the calculation of $\mathcal{Z}$ . . . . .	89
8.1	The LUX exclusion limit on neutralino-hadron scattering cross section used in this scan. This has since been superceded by an updated limit, but it does not impact the viability of the benchmark points obtained in this chapter. . . . .	94
8.2	Gaussian probability centred on $m_{h_1} = 125.3$ GeV and $\Omega h^2 = 0.1196$ . Low heat map values represent high likelihood. . . . .	96
8.3	The SI cross section plotted against the neutralino mass as a function of the fake likelihood. The curve follows the LUX constraint for neutralino masses between 300 GeV and 1 TeV, but at this point curves sharply downwards to favour neutralino masses at 1 TeV. . . . .	96
8.4	ATLAS figure (from [126]) displaying the lower bound on the gluino mass in the cMSSM/mSUGRA model. . . . .	97
8.5	Maximum gluino masses plotted against $m_0$ and $M_{1/2}$ . $m_{\tilde{g}}$ has a linear dependence on $M_{1/2}$ . . . . .	99
8.6	Binned values of the Higgs mass and relic density closest to 125.3 GeV and 0.1196 respectively, plotted against $m_0$ and $M_{1/2}$ . . . . .	99
8.7	Binned maximum values of $m_{\tilde{u}_L}$ plotted against $m_0$ and $M_{1/2}$ . These are mostly well beyond the scope of the LHC. . . . .	100
8.8	Binned maximum values of $m_{\tilde{t}_1}$ plotted against $m_0$ and $M_{1/2}$ . These are smaller than the first and generation squark masses, but are still mostly beyond the scope of the LHC. . . . .	100

---

8.9	Maximum binned values of the left-hand first generation squark masses plotted against $\lambda$ and $s$ . Plots of the other first and second generation squarks, $m_{\tilde{d}_r}$ , $m_{\tilde{u}_l}$ and $m_{\tilde{u}_r}$ , look extremely similar, so for the sake of brevity only one plot has been printed. The majority of points sampled are not only well above established lower bounds on the squark masses, but also beyond being detected in current runs of the LHC, particularly for $s > 20$ TeV. . . . .	101
8.10	Maximum binned samples of the third generation squark mass $m_{\tilde{b}_1}$ plotted against $\lambda$ and $s$ . As in the case of the first and second generation squarks, the majority of points sampled are well above LHC limits and detectability. . . . .	102
8.11	Plotting minimum binned values of $m_{\tilde{b}_1}$ , demonstrating the range of squark masses that may be obtained for a given value of $s$ . . . . .	102
8.12	Binned maximum values of $M_{Z'}$ plotted against $m_0$ and $M_{1/2}$ . . . . .	103
8.13	Neutralino mixing content. . . . .	105
8.14	Inert Higgsino content. . . . .	106
8.15	Maximum binned plots of the inert Higgsino content, showing its correlation with $\lambda_{11}$ , $\lambda_{22}$ and $s$ . . . . .	107
8.16	Maximum binned plots of the inert Higgsino content, showing its correlation with $\lambda_{11}$ and $\lambda_{22}$ together. . . . .	107
8.17	The frequency of sampled points containing Higgsino and inert Higgsino content respectively on a scale between 0 (no Higgsino content) and 1 (full Higgsino content). . . . .	108
8.18	The SI cross section plotted against bino, Higgsino and inert Higgsino content respectively. This cross section tends to be largest with an admixture of bino and Higgsino content in the lightest neutralino. . . . .	108
8.19	Maximum binned plots of the SI cross section from sweeps across $x_{u2}$ , $x_{u1}$ , $x_{d2}$ and $x_{d1}$ , with other parameters free to vary. . . . .	109
8.20	Repeating plots with the maximum binned $\sigma_{SI}$ limited to lie above $6 \times 10^{-45}$ cm <sup>2</sup> , demonstrating more clearly that larger cross sections tend to be found for higher values of $x_{d1}$ and $x_{d2}$ and lower values of $x_{u1}$ and $x_{u2}$ . . . . .	110
8.21	Maximum binned plots of the SI cross section from sweeps across $\lambda_{11}$ , with other parameters free to vary. . . . .	111

---

8.22	Plotting maximum binned values of the SI cross section against $x_{u1}$ and $m_{\tilde{\chi}_1^0}$ .	112
8.23	Maximum binned plots of the SI cross section from sweeps across $\lambda_{22}$ , with other parameters free to vary. . . . .	113
8.24	Maximum binned plot of the SI cross section, with $\lambda_{11}$ and $\lambda_{22}$ plotted against each other. . . . .	114
8.25	Mapping the maximum binned likelihood against $\lambda_{11}$ and $\lambda_{22}$ . . . . .	114
8.26	The maximum binned value of SI cross section plotted against $m_0$ and $M_{1/2}$ . A narrow band of $M_{1/2}$ values up to 9 TeV are favoured for cross sections above $20 \times 10^{-46} \text{ cm}^2$ , with the highest cross sections found between 3 and 7 TeV. . . . .	115
8.27	Maximum binned $\sigma_{\text{SI}}$ plotted against $s$ and $\tan\beta$ . . . . .	115
8.28	$\mu_{\text{eff}}$ vs $A_0$ . High cross sections heavily correspond to low values of $\mu_{\text{eff}}$ . . . . .	116
8.29	$\lambda$ vs $x_{u1}$ . High cross sections correspond with lower values of $\lambda$ . . . . .	116
8.30	Plotting the $A_0$ trilinear alongside neutralino mass to ascertain regions that have been ruled out by LUX. . . . .	117
8.31	Benchmark points and the WIMP-nucleon SI cross section limit. (a) shows each of the ten benchmarks plotted relative to the LUX dark matter exclusion line used in these scans. (b) directly overlays this exclusion line and the ten benchmark points with the highest SI cross section over the LUX plot from [56]. Only <b>BM10</b> is in the blue exclusion region. Using updated figures from December 2015, <b>BM3</b> and <b>BM9</b> fall within the new blue region, but are still yet to be ruled out. . . . .	118
8.32	$s$ -channel LSP annihilation to a $Z$ boson. . . . .	122
8.33	A plot from the XENON collaboration [134] demonstrating the XENON1T sensitivity (with 90% c.l.) compared to past experiments. This is a sensitivity easily great enough to detect most of the benchmark points given in this chapter. . . . .	126

---

# Introduction

---

*“This is a tale of an elusive matter that I have chosen to relay in verse;  
It fills the stretches of empty space- one quarter of the universe!  
It seems to be clumpy, slow-moving, dark and not the slightest bit rare.  
In galaxies, in clusters and the spaces between - wherever you look, it’s there!  
How can we detect this elusive foe? We must journey underground.  
With detectors at ultra-cool temperatures it may in the future be found.  
But how to describe it? Just what is it? We must have a decent description!  
Equipped with a theorist’s trustworthy tools, we will find the right prescription.  
A new model of physics may do the job, so we’ll give each quark a twin!  
We’ll double the leptons and forces too, but each with different spin.  
Now armed with code and computer power, we’ve gained a neat prediction.  
If dark matter exists as a superpartner, it gives us a new direction:  
We’ll know what to look for and what to expect, and hopefully it’ll come to pass,  
That in the depths of detection chambers, we’ll find dark matter at last!”*

- Me.

The introductory verse above is a summary of this thesis and a succinct description of my research activities carried out at the University of Adelaide during the course of my candidature. My work has focused on dark matter and explanations for its existence in supersymmetric physics that lie beyond the standard model (SM). In particular, I have explored dark matter as a neutralino particle in two models of supersymmetry: the Next-to-Minimal Supersymmetric Standard Model (NMSSM) and the  $E_6$ -inspired Supersymmetric Standard Model ( $E_6$ SSM).

Chapter 2 describes relevant background information on the “missing matter of the

universe,” dark matter. A review of the best available evidence for its existence is presented, including weakly interacting massive particles (WIMPs), massive astronomical compact halo objects (MACHOs) and modified Newtonian dynamics (MOND). Relatively slow-moving WIMPs are currently the best candidate based on information from the cosmic microwave background (CMB), the anisotropy of which gives clues about the existence of early density fluctuations in the universe (this fine structure would have been destroyed if dark matter were too ‘hot’ or fast-moving). The concept of dark matter relic density is explained, and the chapter concludes with a summary of current ongoing dark matter detection efforts (both directly and indirectly).

Chapter 3 is also composed of background material, detailing the status of the current standard model and its particle zoo (quarks, leptons, bosons, etc). Electroweak symmetry breaking and the Higgs mechanism are explained. Although it is a highly successful model, there are many areas in which it is incomplete:

- It still does not adequately describe dark matter; ordinary baryonic matter accounts for only 4% of the universe’s mass-energy budget.
- Gravity has not yet been successfully unified with the other three fundamental forces (weak, strong and electromagnetic).
- There are various hierarchy problems that present issues of ‘naturalness.’ For example, the bare Higgs mass must be fine-tuned to a very high degree in order to keep the mass of the Higgs close to the masses of the  $W^\pm$  and  $Z$  bosons, and yet in the standard model there is no physical explanation for this fine-tuning.
- Charge-parity symmetry presents another problem of fine-tuning, given that experimentally we do not observe breaking of CP for quantum chromodynamic (QCD) interactions even though there is a term in the QCD Lagrangian perfectly capable of breaking CP - hence, it must be fine-tuned to lie close to zero, but the standard model does not yet have a physical explanation for why this must be so.

These gaps motivate physicists to seek new physics beyond the standard model, leading me to the next chapter.

Chapter 4 introduces the theory of supersymmetry, which in its purest essence is an

---

extension of the standard model's Poincaré algebra to include a greater symmetry between matter particles and force particles. The result is that the particles we know in the standard model are embedded in supermultiplets with a spectrum of new particles dubbed their 'superpartners' (with squarks being the superpartners of quarks, sleptons being the superpartners of leptons, and so on). The relevance of supersymmetry to the outstanding problem of dark matter is that as a consequence of R-parity preservation, the lightest supersymmetric particle (LSP) is both stable and weakly interacting. In supersymmetric theories, neutralino particles are composite states of several neutral gauginos (superpartners of gauge bosons, such as the bino, which is the superpartner of the U(1) gauge field). The lightest neutralino is frequently the LSP, making it a suitable candidate for dark matter. Hence, my work concentrates on dark matter as a neutralino WIMP.

Chapter 5 presents original work investigating spin-independent cross sections for neutralino-nucleon scattering in the NMSSM, carried out primarily with collaborator Joel Giedt of Rensselaer Polytechnic Institute under the supervision of my primary supervisor Anthony Thomas and co-supervisor Ross Young. Although the SI cross section can possibly take a wide range of values depending on the composition of the lightest neutralino, applying the latest relic density constraints from WMAP results in a drastic reduction of regions in the NMSSM parameter space for which neutralino dark matter is viable for detection. This work was published in Physical Review D.

Chapter 6 introduces the next supersymmetric model that I focus on in this thesis, the  $E_6$ SSM, which seeks to both solve the  $\mu$  problem of the MSSM while eliminating the drawbacks (such as cosmological domain wall problems) found in other supersymmetric models like the NMSSM. This part of my thesis builds on work primarily undertaken by Peter Athron, Jonathan Hall, Stephen King, Roman Nevzorov, Dominik Stöckinger and Alexander Voigt.

Chapter 7 serves as an exploration of the programs and tools used for the second part of my thesis, which is an exploration of the spin-independent cross section of  $E_6$ SSM neutralinos with nucleons, undertaken with Peter Athron and Martin White. These programs include MultiNest, micrOMEGAs and FlexibleSUSY. Original work is presented exploring the interfacing that was undertaken to get the three programs to work as one unit.

Chapter 8 presents more original work: the largest parameter scan of the  $E_6$ SSM to

date, complete with plots and twelve benchmark models satisfying current experimental constraints. The work presented in chapters 7 and 8 is also presently being written up for future publication.

Chapter 9 is the concluding chapter, and contains an outlook for the future of the  $E_6$ SSM and NMSSM.

---

# Dark Matter

---

Unfortunately for scientists, the nature of the bulk of the universe is still an enigmatic puzzle. The outstanding mystery of dark matter is one of the most pressing concerns of modern physics, as it is thought to constitute 26% of the universe’s mass-energy. By contrast, the baryonic matter described by the current standard model of physics comprises a paltry 5%. The remaining 69% is dark energy, which is beyond the scope of this thesis.

Evidence for the abundance of dark matter comes from a wealth of sources [1]. The following section details some of the more compelling examples of “missing matter” that have led physicists to view dark matter as such a pressing mystery. Experimental detection efforts (both direct and indirect) that are currently underway are also described.

This will eventually lead in a later chapter to a discussion of supersymmetry and why it may provide an excellent dark matter candidate (although it will first be prudent for the basic standard model to be outlined).

## 2.1 Experimental Evidence

### 2.1.1 Zwicky’s ‘dunkle Materie’

The first clue that the universe holds more mass than what is strictly visible came in 1933 during the Swiss astronomer Fritz Zwicky’s observations of the Coma Cluster (Abell 1656), a large cluster with a galaxy count in excess of a thousand [2]. This particular cluster had previously been imaged by the Schmidt Telescope on Mount Palomar, giving a distribution of luminosity and associated matter content consistent with what one might expect based on theoretical predictions of gravitationally bound isothermal gas.

However, calculations of the cluster’s mass based on its galaxy distribution and velocities via the application of the Virial Theorem from classical mechanics paint a rather

different picture. If we treat each galaxy as a particle, we may obtain an expression for the total kinetic energy  $\langle T \rangle$  of a system of  $n$  particles in terms of the forces acting on each particle,

$$2 \langle T \rangle = - \sum_{i=1}^N \langle \mathbf{F}_i \cdot \mathbf{r}_i \rangle, \quad (2.1)$$

where  $\mathbf{F}_i$  is the net force on the  $i$ th particle situated at location  $\mathbf{r}_i$ .

By determining the speeds of the galaxies from their Doppler shifted spectra, Zwicky obtained a lower bound estimate on the average mass of the constituent galaxies of  $4.5 \times 10^{10} M_{\odot}$  ( $M_{\odot}$  = one solar mass), and thus a cluster mass of  $4.5 \times 10^{13} M_{\odot}$  (given that it has roughly 1000 galaxies). This is at odds with the mass obtained from luminosity-based estimates. Zwicky coined this missing matter ‘dunkle Materie’ (dark matter), and attributed it to low energy stars, low luminosity solid bodies and gases which may have also diminished the galaxy cluster’s luminosity.

### 2.1.2 Rotation curves

However, the recognition of dark matter as an outstanding problem of the standard model of physics didn’t truly gain momentum until the work of the American astrophysicist Vera Rubin on galactic rotation curves, beginning in 1970 with an analysis of the orbital rotation of the Andromeda galaxy conducted with Kent Ford [3].

The rotation curve of a galaxy is a plot of the orbital speeds of visible stars and gases against their radial distance from the galaxy’s centre. For a star of mass  $m$  a distance  $r$  from the galaxy’s centre with a total mass  $M$  inside its orbit, treating gravitational force as a centripetal force gives us the following relationship between  $v$  and  $r$ :

$$\frac{mv^2}{r} = \frac{mMG}{r^2}. \quad (2.2)$$

Now, for a star contained within the central hub of a spiral galaxy we expect that the mass contained within its orbit should increase as  $M \propto r^3$ , giving us  $v \propto r$ , whereas for a star located within its disc the contained mass is (relatively) constant, giving us  $M = \text{constant}$  and thus  $v \propto r^{-\frac{1}{2}}$ . This should give a spiral galaxy rotation curve that looks like Fig. 2.1.

However, this is not what is typically observed. In 1980, research on 21 Sc galaxies

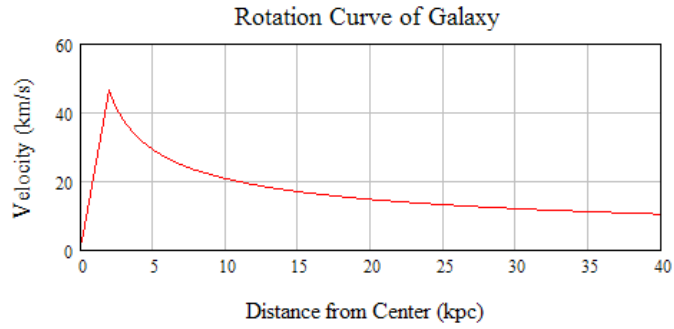


**Figure 2.1:** Expected rotation curve of a galaxy from applying Kepler's Law [4].

demonstrated that rotation curves tend to be remarkably flat, indicating that stars move at near-constant speed independent of their distance from the centre of the galaxy [5]. These rotation curves are displayed in Fig. 2.2.

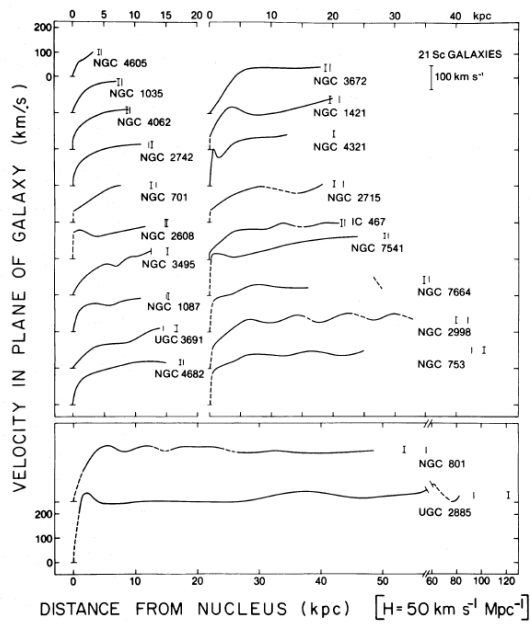


**Figure 2.2:** A plot from [5] displaying stellar mean velocities as a function of linear distance from the nucleus of 21 Sc galaxies.

This deviation from the expected rotation curve based on the luminous matter density of spiral galaxies is strong evidence for hidden (non-luminous) matter interspersed between the stars in a spherical halo centred on the galactic bulge and extending out beyond the galactic disk.

The structure of cold dark matter halos was explored by [6] using N-body simulations,

leading to the well-known Navarro-Frenk-White (NFW) profile,

$$\rho(r) = \frac{\rho_{crit}\lambda_c}{\frac{r}{R_s} \left(1 + \frac{r}{R_s}\right)^2}, \quad (2.3)$$

where  $\rho_{crit} = \frac{3H^2}{8\pi G}$  is the critical density,  $R_s$  is a scale radius and  $\lambda_c$  is a dimensionless parameter; the latter two parameters vary from halo to halo. This describes dark matter as a spherical halo with a central ‘cusp’.

However, since this does not appear to fit all galaxies (see, for instance, [7]), other models have been developed that may be used to describe dark matter density structures. For example, [8] conducted a survey of 240 halo objects (including red giant stars, globular clusters and satellite galaxies) to ascertain constraints for our own galaxy’s mass, fitting the velocities of these objects to both NFW and truncated flat (TF) profiles and finding that both are consistent with the calculated dark matter density of the Milky Way Galaxy.

### 2.1.3 Gravitational lensing

The principle behind gravitational lensing is that light is bent by the gravitational field of a massive object. The greater the mass of the object, the greater the gravitational distortion of space and thus magnitude of the light’s deflection from its original path. This can reveal the presence of dark matter that is otherwise undetectable by radiation, as shown by Fig. 2.3.

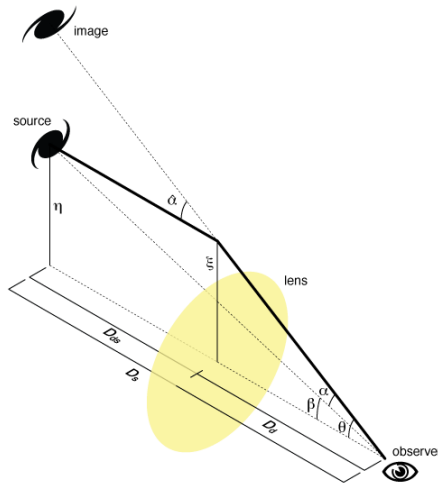


**Figure 2.3:** The gravitational lensing effect [9].

---

Gravitational lensing is sorted into three types: strong lensing, weak lensing and microlensing [10]. Strong gravitational lensing results in highly visible distortions, such as arcs or multiple images. Weak gravitational lensing is rather more difficult to discern, as it involves much more minor distortions [11]. In order to use the weak gravitational lensing effect to calculate the rough dark matter content of a particular galaxy cluster, astronomers observe the appearance of the distant background galaxies. Although galaxies can take many different elliptical shapes, the shear deformation as a result of massive foreground objects can be measured as a coordinate transformation from the statistical average of galaxy orientations (deviations from the average expected from a completely random assortment of galaxy orientations are assumed to result from gravitational lensing). Finally, microlensing refers to gravitational lensing by stars [12].

Particularly compelling evidence for the existence of dark matter was found by [13] during observations of the object 1E0657-558 (known as the ‘bullet cluster’, which is in fact two galaxy clusters passing through each other). The total matter distribution of the cluster was mapped by gravitational lensing, and found to be concentrated in two distinct regions. However, the hot baryonic matter was mapped using the Chandra X-ray satellite, and found to be clustered in two very different regions from the dark matter. This is strong evidence for dark matter as a weakly interacting substance; due to its weakly interacting nature, dark matter passes through the collision largely unimpeded, whereas the baryonic plasma is slowed down by tidal and electromagnetic forces, leading to spatial separation of the two kinds of matter. This is also evidence against modified Newtonian dynamics (MOND) as an alternative explanation for dark matter, since it does not accurately predict this phenomenon.

#### **2.1.4 The Cosmic Microwave Background**

Evidence for dark matter may also be gleaned by studying the cosmic microwave background (CMB) [14].

The CMB is the radiative remnant of the Big Bang, from a time in which the early universe was filled with hot, dense plasma comprised of baryons, photons and dark matter. Initially, photons were effectively “bound” within the primordial plasma, as they could not propagate any great distance without being scattered and reflected from free-moving

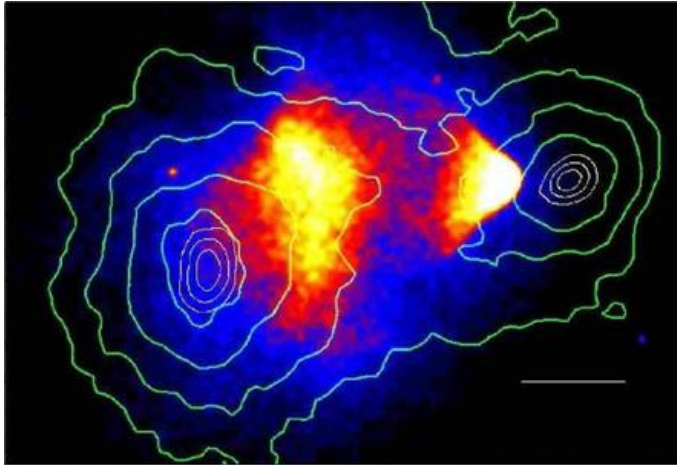


**Figure 2.4:** The bullet cluster, from [13]. The green lines are mass contours, indicating the presence of dark matter (observed by gravitational lensing). The white regions are two sources of hot, X-ray emitting plasma gas.

matter particles. Roughly 380,000 years into the universe's expansion, the first atoms formed; the mean free path of wandering photons increased as they could move more freely through space, and thus photons gradually became decoupled from baryonic matter. This is known as the last scattering surface of the CMB. As the universe expanded, this radiation cooled adiabatically; today, its thermal blackbody spectrum indicates that the universe has a radiative temperature  $T = 2.7260 \pm 0.0013$  K [15, 16].

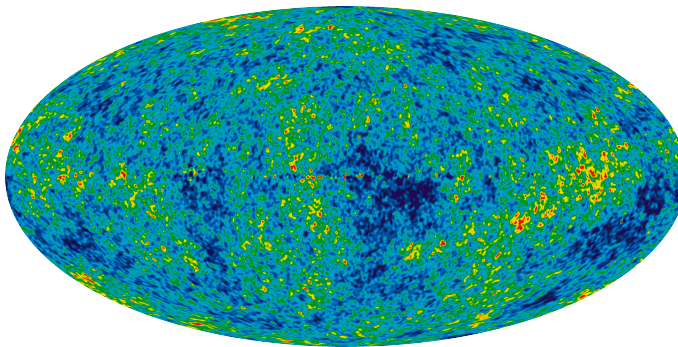


**Figure 2.5:** A map of the universe's temperature distribution from WMAP [17].

However, although the CMB is mostly isotropic it is not entirely smooth, since very minute fluctuations can be detected with appropriately sensitive instruments such as the Wilkinson Microwave Anisotropy Probe (WMAP) (see Fig. 2.5) [17]. In part, these small-scale deviations from the radiative pattern originate from small-scale fluctuations in density in the early universe. By studying the magnitude of these anisotropies, we can gain

---

insight into the conditions of the early universe, and consequently the evolution of larger scale structures that formed from smaller ones as the universe expanded. Whenever a region of space had a slightly higher concentration of matter, gravitational attraction resulted in the coalescence of more matter, gradually giving rise to the formation of stars and galaxies; this is known as hierarchal structure formation.

Surveys of the universe have indicated that galaxies are not uniformly spread throughout space, but instead tend to align along “strings” surrounding bubbles or voids of near-empty space [18]. The presence of dark matter in galactic formation scenarios greatly changes the time scale and nature of the creation of these large structures. For instance, we find from the CMB that deviations from the average density are  $\partial\rho/\rho \approx 0.3-1.4 \times 10^{-4}$ . This is considerably lower (by about two orders of magnitude) than expected from theoretical arguments of cosmological nucleosynthesis predicting that gravitational collapse of a region occurs when  $\partial\rho/\rho \approx 1$ . If dark matter that has little interaction with radiation was sufficiently abundant, pockets of high dark matter could accumulate without appearing as variations in density in the CMB’s “photograph” of the early universe.

Another observation that dark matter must be consistent with is the observation that large-scale matter densities often tend to be spaced apart at intervals of roughly 490 million light-years; this is such a consistent feature of the universe that it is used as a standard candle for measuring cosmological distances [19]. This particular feature is thought to have been triggered by baryonic acoustic oscillations (BAO) in the early universe, and correlate with acoustic peaks in the CMB spectrum. If we describe  $d_H$  as the acoustic horizon distance at decoupling, it has a relationship with matter density  $\Omega_M$  that is described as:

$$d_H \propto \frac{1}{\sqrt{\Omega_M}}. \quad (2.4)$$

The most favoured cosmological model in the present day is the Lambda-Cold Dark Matter ( $\Lambda$ CDM) model, which has been shown to be consistent with BAO, CMB anisotropies and large-scale structures [20].

Within the  $\Lambda$ CDM model, the dark matter mass density parameter is given as the ratio of dark matter to the critical mass density of the Friedman universe,  $\Omega_{DM} = \frac{\rho_{DM}}{\rho_{crit}}$ . Here,  $\rho_{crit}$  determines the shape of the universe:  $\Omega_{TOT} = 1$  describes a flat universe

---

(in which the expansion of the universe decelerates in the absence of dark energy but eventually accelerates if dark energy is present), while  $\Omega_{\text{TOT}} > 1$  is a closed universe (gravitational attraction overcomes the universe's expansion) and  $\Omega_{\text{TOT}} < 1$  is an open universe (the universe's expansion continues forever). The current best measurement is  $\Omega_{DM} = 0.265(11)$ , while the dark energy density is  $\Omega_{\Lambda} = 0.685^{+0.017}_{-0.016}$  [21].

## 2.2 Dark Matter Candidates

### 2.2.1 MACHO Dark Matter

This fundamental mismatch between luminous matter and mass based on gravitational interactions suggests that a large portion of the universe's matter content is unaccounted for and does not interact electromagnetically (hence “dark”). However, it was still an open question as to whether or not this matter is non-baryonic or can be accounted for in the Standard Model. One theory is that dark matter consists of Massive Astronomical Compact Halo Objects (MACHOs) - that is, large, cool bodies such as brown dwarfs, planets, black holes and very faint red dwarfs.

However, this idea has fallen out of favour on both theoretical and experimental grounds [22, 23]. The amount of baryonic matter in the universe in predictive models cannot account for the proportion that would be necessary to account for missing matter in the form of faint bodies; a dark matter composed predominantly of baryons is also in contradiction with the observations of the CMB previously discussed. Furthermore, it is inconsistent with microlensing experiments, such as those by MACHO and EROS, which conducted surveys of star systems in the Large Magellanic Cloud (LMC). If a MACHO object passes between Earth and a distant star, the apparent brightness of the star will dim slightly, but then flare as the gravitational field of the dim object bends and focuses the light from the star around it. The quantity of MACHO objects in the Milky Way Galaxy found by gravitational lensing surveys is insufficient to explain our galaxy's flat rotation curve.

### 2.2.2 Modified Newtonian Dynamics

Modified Newtonian Dynamics (MOND) is an explanation for dark matter that moves away from providing a candidate in the form of ‘missing matter,’ and instead postulates that Newton’s Laws themselves must be modified to account for the mass discrepancy [24]. In this theory, the relationship between force and acceleration is modified by a new fundamental constant,  $a_0$ , and an interpolating function,  $\mu$ :

$$\vec{F} = m\mu\frac{a}{a_0}\vec{a}. \quad (2.5)$$

At high accelerations as typically encountered in the solar system ( $a \gg \gg a_0$ ),  $\mu \approx 1$ , which means that classical Newtonian mechanics is restored. For much lower accelerations (as typically encountered in galaxy dynamics), the physics is governed by the MOND regime.

MOND has had some success in accounting for galaxy dynamics, such as the behaviour of low surface brightness galaxies [25, 26]. However, as explained in an earlier section, MOND fails to be consistent with the dark matter mass distribution of the observed Bullet cluster, and still does not completely account for mass discrepancies in galaxy clusters. For these reasons, it has generally fallen out of favour as an explanation for dark matter.

### 2.2.3 WIMP Dark Matter

Weakly interacting massive particles (WIMPs) are dark matter candidates with the following properties:

1. They have a relatively large mass compared to standard particles
2. They interact only via the gravitational force (slightly) and the weak nuclear force

Any theoretical model involving WIMPs must be consistent with both CMB perturbations and the structure of the universe observed today. For instance, models favouring “hot” WIMPs (that is, dark matter consisting of particles moving at relativistic speeds) have been disfavoured on the basis that such fast-moving particles impedes hierarchal structure formation by smoothing out clumps of dense matter in the early universe. In such a scenario, the only way that recognisable smaller scale structures could form is by

“top-down” methods, in which giant super-clusters of matter gradually fragment over time to fall smaller pockets of high matter density. This is inconsistent with the observed CMB, which features anisotropies in the early universe. On the other hand, “warm” and “cold” WIMPs are consistent with hierarchal structure building, and so have gained favour in dark matter models.

Examples of theoretical WIMPs include supersymmetric (SUSY) particles such as gravitinos, axinos, sneutrinos and neutralinos - the last of these will be the focus of this thesis, and will be explained in an upcoming chapter. WIMP candidates may also be derived from theories of extra dimensions. In these models, the lightest Kaluza Klein particle is also potentially a good dark matter candidate [27], since it is stable as a result of a Kaluza-Klein parity.

#### 2.2.4 Other candidates

After WIMPs, the most favoured dark matter candidate is the axion, a theoretical neutral particle that is the pseudo Nambu-Goldstone boson generated from a spontaneously broken Peccei-Quinn symmetry. This was originally proposed by Steven Weinberg and Frank Wilczek in the late 1970s [28, 29]. The axion potentially makes for a good dark matter candidate because of its predicted properties: electrically neutral, light (less than  $1 \text{ eV}/c^2$ ) and weakly interacting. The supersymmetric partner of an axion, the axino, may also be the lightest supersymmetric particle (LSP) in certain SUSY models.

Another hypothetical particle is the sterile neutrino, which are distinguished from the known active neutrinos in that they do not interact with any other particles via fundamental interactions with the exception of gravity, thus fulfilling the ‘weakly interacting’ condition of a good dark matter candidate. These exist as right-handed degrees of freedom, requiring an extension of the standard model, and may have been produced in the early universe through decays of heavy bosons. Further details on sterile neutrinos as dark matter are described by [30].

### 2.3 Dark matter relic density

A concept that will feature heavily in the coming chapters is that of dark matter relic density. In the early universe, energetic particle collisions were frequent. However, as the

universe expanded, particle collisions became less and less frequent (since the probability of two WIMPs meeting each other to annihilate was reduced), and lighter particles no longer had the required thermal energy to create heavier particles. As a result, the WIMP number density,  $n_\chi$ , became (roughly) constant, being further decreased only by the expansion of space itself. This is called the ‘freeze out’ point, and the final number density of dark matter particles is said to be the relic abundance [31,32].

The evolution of  $n_\chi$  with time  $t$  is governed by Boltzmann’s equation:

$$\frac{dn_\chi}{dt} = -\langle\sigma v\rangle (n_\chi^2 - n_{\chi,eq}^2) - 3Hn_\chi, \quad (2.6)$$

where  $\sigma$  is the annihilation cross section,  $v$  is the relative velocity,  $H$  is Hubble’s constant and  $n_{\chi,eq}$  is the number density at equilibrium. The first term accounts for interactions between WIMPs (both annihilation, which decreases WIMP count, and creation from the inverse process, which increases WIMP count), while the second term accounts for the expansion rate of the universe. This may be rewritten in terms of the co-moving number density,  $Y = n_\chi/s$  (where  $s$  is entropy density), and  $x = m_\chi/T$  (where  $m_\chi$  is the mass of the WIMP and  $T$  is temperature). Substituting  $Y$  first leads to the new time derivative:

$$\frac{dY}{dt} = \frac{dn_\chi}{dt} \frac{1}{s} - \frac{n_\chi}{s^2} \frac{ds}{dt}. \quad (2.7)$$

Since  $ds/dt = -3Hs$  (entropy conservation) and  $dn_\chi/dt$  is given by Eq. 2.6,

$$\begin{aligned} \frac{dY}{dt} &= \frac{1}{s}(-\langle\sigma v\rangle s^2 (Y^2 - Y_{eq}^2) - 3Hn_\chi) + \frac{3Hn_\chi}{s} \\ &= -s\langle\sigma v\rangle (Y^2 - Y_{eq}^2). \end{aligned} \quad (2.8)$$

Making the final substitution  $x = m_\chi/T$  leads to:

$$\frac{dY}{dT} = -\frac{m}{x^2} \frac{1}{3H} \frac{ds}{dT} \langle\sigma v\rangle (Y^2 - Y_{eq}^2). \quad (2.9)$$

The WIMP relic density,  $\Omega_\chi$ , is given as the ratio of the dark matter density to the critical density:

$$\Omega_\chi = \frac{\rho_\chi}{\rho_{\text{critical}}}. \quad (2.10)$$

Given that  $\rho_{\text{critical}} = 3H^2/8\pi G$  ( $G = 6.71 \times 10^{-39} \text{ GeV}^{-2}$  being the gravitational constant) and  $\rho_\chi = s_0 Y_0 m_\chi$  ( $s_0 = 2.24 \times 10^{-38} \text{ GeV}^3$  being the current entropy density of the universe), the relic density can be written neatly by factoring out  $h = H/100 \text{ km s}^{-1} \text{ Mpc}^{-1}$  - the final result depends on only two variables, the mass of the WIMP and the present-day ratio of number density to entropy density,  $Y_0$ :

$$\Omega_\chi h^2 = 2.755 \times 10^8 Y_0 \frac{m_\chi}{[\text{GeV}]}. \quad (2.11)$$

$Y_0$  is found by integrating Eq. 2.9, which can be done accurately by using programs such as micrOMEGAs. An approximate solution is:

$$Y_0 = \sqrt{\frac{45G}{\pi g_{\text{eff}}(T_f)} \frac{1}{\langle \sigma v \rangle_{\text{avg}}}}, \quad (2.12)$$

where  $g_{\text{eff}}$  is the number of internal degrees of freedom and the thermally averaged  $\langle \sigma v \rangle$  is:

$$\langle \sigma v \rangle_{\text{avg}} = \int_0^{T_F} \langle \sigma v \rangle(T) dT. \quad (2.13)$$

All dark matter particle detection efforts, elaborated upon in the next section, must yield results that are consistent with the observed relic density, the current best estimate of which is [33]:

$$\Omega h^2 = 0.1196 \pm 0.0031. \quad (2.14)$$

## 2.4 Current Detection Efforts

Evidence for the existence of dark matter so far has come in the form of observation of the cosmos; a dark matter particle has yet to be directly detected. However, there are various searches around the world underway to find such an elusive particle, both directly (including CDMS, DAMA/LIBRA, DRIFT, EDELWEISS, LUX, PICASSO, SIMPLE, WArP, XENON, XMASS and ZEPLIN-III) [35–45] and indirectly (including AMANDA, ANTARES, Fermi-LAT, IceCube and PAMELA) [46–50].

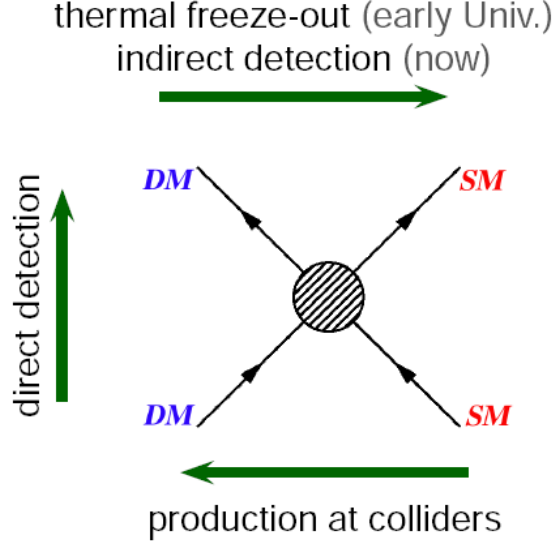


**Figure 2.6:** Direct vs indirect detection [34].

### 2.4.1 Direct Detection

Theoretically, if dark matter permeates the universe and is concentrated in regions of high baryonic density (such as the Milky Way galaxy), we should be able to observe it via direct detection experiments that are sensitive enough to pick up its interaction with other matter. Direct detection of hypothetical WIMPs typically involves detecting recoil energy when a dark matter particle collides with a baryon, such as a neutron or proton. The WIMP flux is given by:

$$\Phi_\chi \approx \frac{\rho_0 \bar{v}_\chi}{m_\chi}. \quad (2.15)$$

If we assume a local WIMP density of  $\rho_0 = 0.3 \text{ GeV}/c^2$  and particle speed of  $\bar{v}_\chi = 270 \text{ km/s}$  [51], then the expected WIMP flux is approximately  $10^5 \text{ s}^{-1}\text{cm}^{-2}$ . When a WIMP elastically scatters from one of the nuclei within the detector, the recoil energy spectrum is measured by

$$\frac{dR}{dQ} = \frac{\sigma_0 \rho_0}{\sqrt{\pi} v_0 m_\chi m_r^2} F^2(Q) T(Q), \quad (2.16)$$

where  $\sigma_0$  is the elastic scattering cross section between the WIMP and nucleus (which, when spin-independent, is proportionate to the WIMP-nucleon scattering cross section  $\sigma_{\chi-p}$  multiplied by the atomic number of the nucleus  $A$  squared),  $m_r = \frac{m_\chi m_N}{m_\chi + m_N}$  is the WIMP-nucleus reduced mass,  $F(Q)$  is the nuclear form factor and  $T(Q)$  is an integral (of zero dimension) over the local WIMP velocity distribution [51].

However, our planet is also bombarded with high energy cosmic rays from sources outside of the solar system at roughly a rate of 100 events per second for each square metre of the planet's surface, which means that any experiment hoping to directly detect dark matter must find a way to minimise any background events that could obscure a positive dark matter detection. Cosmic rays generally tend to disperse into showers of energetic particles upon interaction with the upper atmosphere, and these streams are extremely penetrating. Thus, dark matter detection chambers tend to be located deep underground in order to reduce the number of interfering cosmic ray events to a factor of  $10^{-6}$  of the surface flux.

A typical direct detection experiment consists of a chamber of an inert liquid, such as xenon or argon. For example, the Large Underground Xenon (LUX) experiment is a direct detection facility located in a laboratory one mile beneath the surface of the Earth in South Dakota, USA, consisting of a chamber filled with 370 kg of liquid xenon [52].

When a passing WIMP scatters elastically from a target nucleus, it transfers some of its kinetic energy, resulting in excitation, ionization and recoil (which in turn results in secondary collisions with other atoms in the noble liquid). Flashes of light are released in a process known as primary scintillation (the excited electrons of the target nucleus return to their original state by releasing photons). These photons are collected by photomultiplier tubes at the top and bottom of the liquid chamber.

However, double-phase detectors also pick up secondary scintillation (the subsequent S2 signal; primary scintillation is designated S1). This occurs when the ionized electrons drift upwards as the result of an applied electric field, eventually interacting with a thin layer of noble gas (as shown in Fig. 2.7). The time difference between the S1 and S2 signals allows the depth of the initial WIMP-nucleon interaction in the liquid to be calculated.

WIMP events are differentiated from background events by their weakly interacting nature; since they have a very slim chance of interacting with a target, such a collision is likely to only occur once in the liquid, thus registering as a single event. Other particles, however, will have multiple collisions within the noble liquid.

The advantages of using a liquid of a noble element such as xenon are numerous [53].

1. Noble liquids are cheap and dense (self-shielding), and thus useful for large scale detectors.

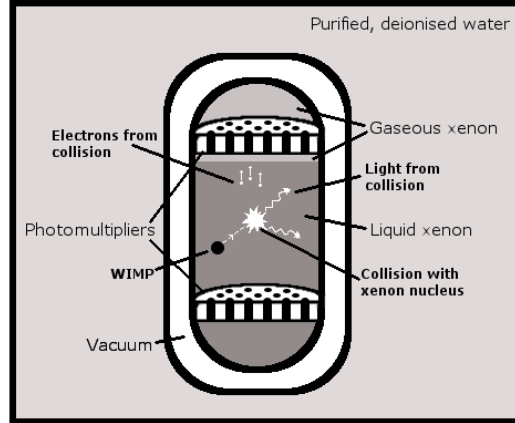


**Figure 2.7:** A schematic of the LUX detection chamber

2. They are easily purified; contaminants like  $^{85}K$  may be removed by techniques such as cryogenic distillation. Xenon in particular lacks long-lived radioisotopes that would otherwise provide unwanted background events (atmospheric argon, on the other hand, contains  $^{39}Ar$  - however, liquid argon is cheaper than xenon and more easily purified).
3. They maximise WIMP-nucleon interaction cross sections, since  $A^2$  is reasonably large.

Unfortunately, WIMP-nucleon cross sections are still incredibly small. Since the expected total scattering rate for a target  $T$  with atomic mass  $A_T$  is

$$R_T = \frac{\sigma_{\chi-N} \Phi_{\chi} N_A}{A_T}, \quad (2.17)$$

where  $N_A$  is Avogadro's number, this results in a maximum of approximately 1 event per 10 years for every kilogram of xenon (and even fewer for argon). Fig. 2.8 shows the predicted WIMP-nucleon elastic scattering rates for various target nuclei [54].

Although no dark matter events have been detected, null results from the LUX experiment have established strong bounds on spin-independent WIMP-nucleon cross sections (dependent on WIMP mass), which are given in Fig. 2.9 (see the lowest black line) from [55]. For WIMP masses just below 100 GeV, the bound on current detection is roughly  $10^{-45} \text{ cm}^2$ .

In addition to noble liquid detectors, there are also cryogenic detectors such as the

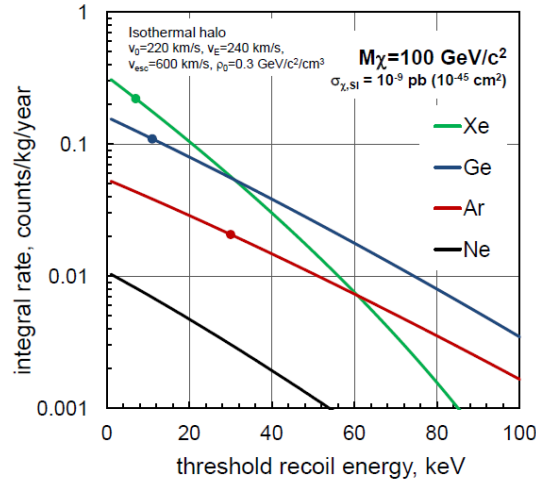


**Figure 2.8:** The predicted WIMP-nucleon elastic scattering rates for various target nuclei, from [54].

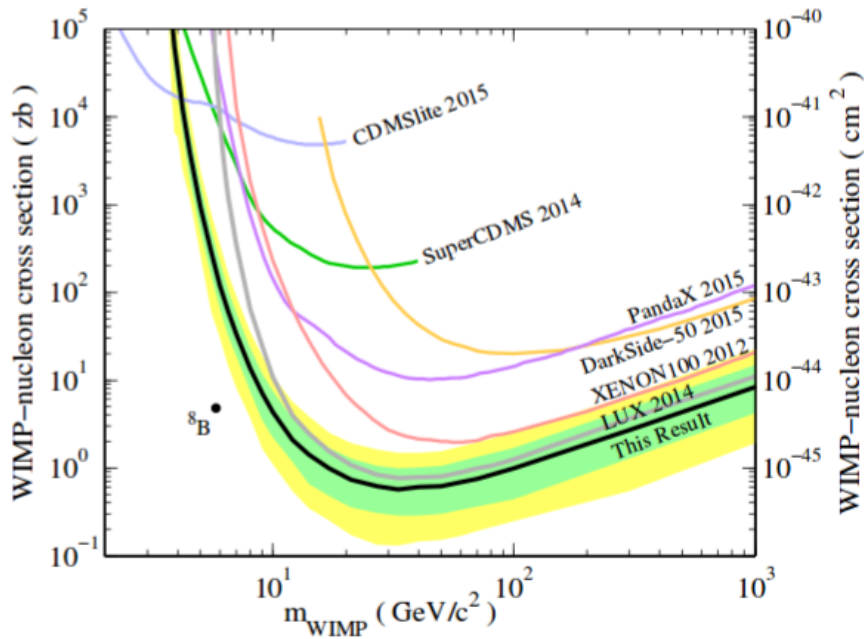


**Figure 2.9:** Constraints on spin-independent WIMP-nucleon cross sections from the LUX experiment (figure from [55]). This is an update on 2013 limits on the WIMP-nucleon cross section from [56].

Cryogenic Dark Matter Search (CDMS) [36]. CDMS (currently in its SuperCDMS phase) consists of a series of semiconductor crystal detectors (with a total mass of approximately 10 kg) located deep underground in Minnesota. These germanium crystals are cooled to millikelvin temperatures in order to ensure that potential dark matter events are as

distinguishable as possible.

When a particle such as a WIMP scatters from a nucleus in the detector, the recoil triggers a series of vibrations (phonons) through the crystal. The energy from the phonons is eventually transferred to electrons moving through tungsten strips which, as they move from a superconducting to a normal state, generate a pulse. Just as with noble liquid detectors, potential WIMP signals must be differentiated from background rates via statistical interpretation.

### 2.4.2 Indirect Detection

Although the scope of this thesis shall be concerned with the direct detection of dark matter, there are also indirect detection efforts that involve searching for the products of WIMP annihilation in the Milky Way galaxy.

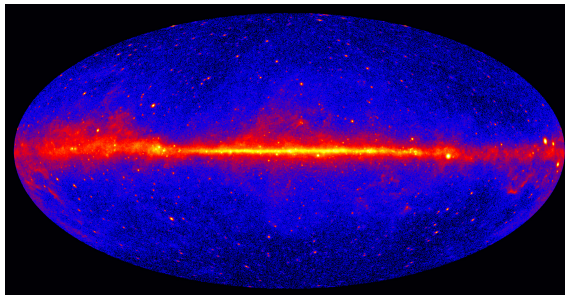


**Figure 2.10:** From the Fermi LAT collaboration [57], this image is the result of a 5 year survey of the entire sky at gamma ray energies over 1 GeV.

Some instruments search for annihilation products in the form of high energy gamma rays, such as the Fermi Gamma-ray Space Telescope (FGST), which has a main instrument called the Large Area Telescope (LAT) [46]. In addition to performing sky surveys (see Fig. 2.10) and probing black holes and pulsars, one key scientific objective of the LAT mission is to search for an excess of gamma rays at the centre of our Milky Way galaxy which may have been produced from dark matter annihilation.

In February 2014, a team of Fermi scientists [58] presented a compelling case for a statistically significant and spherically symmetrical signal extending out to  $10^\circ$  from the galaxy centre (Sgr A\*), consistent with a 31-40 GeV dark matter particle annihilating to  $\bar{b}b$  with an annihilation cross section (multiplied by relative velocity) of  $\sigma v = (1.4 - 2.0) \times$

$10^{-26}$  cm<sup>3</sup>/s. The flux of gamma rays generated by such an event is given by

$$\Phi(E_\gamma, \psi) = \frac{\sigma v}{8\pi m_\chi^2} \frac{dN_\gamma}{dE_\gamma} \int_{\text{los}} \rho^2(r) dl, \quad (2.18)$$

where  $dN_\gamma/dE_\gamma$  is the gamma-ray spectrum produced per annihilation,  $\psi$  is the direction observed and ‘los’ stands for ‘line of sight.’ The density of dark matter,  $\rho(r)$ , is given by a NFW spherical halo profile with a scale radius of 20 kpc.

As the authors note, however, statistically significant signals have also been detected by a number of experiments, including CoGeNT, CDMS, CRESST, DAMA/LIBRA, PAMELA, WMAP, ATIC and INTEGRAL, that have turned out to not have been generated by dark matter but by other causes (both astrophysical and environmental/instrumental). It is speculated that millisecond pulsars may also be responsible for such a gamma-ray excess; however, the extended nature of the signal seems to be inconsistent with the distribution of pulsars in the innermost region of the galaxy.

Some detectors, such as PAMELA (Payload for Antimatter Matter Exploration and Light-nuclei Astrophysics), located on a Russian satellite in orbit, search instead for an excess of high energy cosmic ray positrons as a potential dark matter annihilation signal [47]. In 2008, preliminary data appeared to indicate an excess of high-energy (up to 90 GeV) positrons in the Milky Way galaxy, but without the excess of antiprotons that were predicted from models of dark matter annihilation [59].

High energy neutrino telescopes, such as IceCube and ANTARES, are also searching diligently for dark matter [60,61]. It is thought that WIMPs may be gravitationally bound and concentrated inside more massive objects such as the Sun, thus annihilating with each other at a high rate and producing neutrinos in excess. IceCube, located at the South Pole, is comprised of an array of several thousand photomultiplier tubes deep beneath the surface of the ice (in addition to a surface array detector known as IceTop), which detect Cherenkov radiation - the light equivalent of a ‘sonic boom,’ produced when high-energy particles propagate faster than the phase velocity of photons within a dense dielectric medium - from charged particle products of neutrino-nucleon interactions.

## 2.5 Summary

This chapter has presented known evidence for the existence of dark matter, and demonstrated that the existing standard model of physics cannot account for its abundance. Thus, physics beyond the standard model is required to provide adequate explanatory models, and supersymmetric particles are leading candidates for dark matter. Direct detection experiments provide ways to constrain these models (and are also in turn guided by benchmark points provided by theoretical models, which give motivated masses and cross sections for experimental testing).

The next chapter will underline the present status of the standard model, leading to an explanation of supersymmetry.



---

# The Standard Model

---

The standard model (SM) of modern physics is a quantum field theory that classifies each of the known subatomic particles and the fundamental forces governing their interactions with each other (with the exception of the gravitational force). Although it is incomplete, it is the overarching model that we currently use to describe the world around us. It has been immensely successful at providing experimental predictions, such as the existence of the Higgs boson which was finally discovered at the LHC in 2012 [62, 63].

As a combination of gauge field theories, the SM has been in development since the 1960s, in which the work of Sheldon Glashow, Steven Weinberg and Abdus Salam led to the formation of the electroweak theory, which describes the weak and electromagnetic forces [64–66]. Together with the theory of quantum chromodynamics (QCD) developed in the 1970s, which describes the strong force, these theories form the backbone of the SM. As mentioned, the fourth force of nature, gravity, has yet to be satisfyingly incorporated into the SM.

In the following chapter a brief overview of the SM will be provided, including its particle content, matter and forces, electroweak symmetry breaking and outstanding problems that are yet to be solved. This will lead directly into a discussion on supersymmetry and the ways in which it resolves these flaws in order to build a more complete model of physics that is consistent with our observations of the universe.

## 3.1 Fundamental matter and forces

Prior to the 1960s, it was believed that there were merely four fundamental particles: the electron  $e^-$ , the proton  $p$ , the neutron  $n$  and the neutrino  $\nu$ . However, with the development of the SM and its underlying quantum field theories came an explosion of

new theoretical particles, many of which have been experimentally confirmed.

All particles may be split into two basic categories according to the Pauli Exclusion Principle (PEP): **fermions** and **bosons**. Fermions obey PEP, which means they may not occupy the same quantum state simultaneously; for example, two electrons in the same orbital ‘shell’ around an atom must not have the same spin state. They conform to Fermi-Dirac statistics. Bosons, on the other hand, do not obey PEP and are governed instead by Bose-Einstein statistics. The factor that distinguishes fermions and bosons is a quantity known as spin, which is a form of angular momentum intrinsic to particles. The spin quantum number is given in units of the reduced Planck constant  $\hbar$  by  $s = n/2$ , where  $n$  is an integer  $\geq 0$ ; fermions take half-integer spins (1/2, 3/2, 5/2...), while bosons have whole-integer spins (0, 1, 2...).

If we suppose that we have two identical particles in positions 1 and 2, and then interchange them, the probability of finding one particle in position 1 and the other in position 2 must remain constant (since the particles are identical and cannot be distinguished from each other). As the probability amplitude is given as the square of the particle wavefunction, this means that

$$P(1, 2) = P(2, 1), \quad (3.1)$$

$$\therefore |\Psi(1, 2)|^2 = |\Psi(2, 1)|^2, \quad (3.2)$$

which further implies that  $\Psi(1, 2) = \pm\Psi(2, 1)$ . The wave function of a fermion reverses sign under particle interchange, while that of a boson stays the same.

	Fermions	Bosons
Elementary particles	Quarks ( $u, d, c, s, t, b$ ) Leptons ( $e^-, \nu_e, \mu^-, \nu_\mu, \tau^-, \nu_\tau$ )	Gauge bosons ( $\gamma, g, Z, W^\pm$ ) Higgs ( $H^0$ )
Composite particles (Hadrons)	Baryons ( $qqq$ or $\bar{q}\bar{q}\bar{q}$ )	Mesons ( $q\bar{q}$ )

**Table 3.1:** The classification of fermions and bosons in the SM.

### 3.1.1 Fermions

All known matter is fermionic in nature. Elementary fermions (single particle states) are either **quarks** or **leptons**. Quarks interact with each other via the electromagnetic, weak and strong forces, whereas leptons interact via only the electromagnetic and weak forces. Since quarks experience strong interactions while leptons do not, they have an additional quantum property known as ‘color’, which may be either red (R), blue (B) or green (G) (or antired, antiblue and antigreen in the case of anti-quarks) - these are labels to describe the type of strong charge, rather than a graphical description of each quark!

Quarks and leptons are further categorised into three families, or ‘generations’, each consisting of an ‘up-type’ and a ‘down-type’ particle (the three positively charged up-type quarks, up  $u$ , charm  $c$  and top  $t$ , are up-type) which behave in a general manner under application of the weak force; by emitting or absorbing a  $W$  boson (which will be defined shortly), an up-type quark may change to a down-type quark, and vice versa. Each generation is heavier than the one before (see Table 3.2).

	Particle family	Mass
Quark generation 1	$\begin{pmatrix} u \\ d \end{pmatrix}$	$2.3_{-0.5}^{+0.7}$ MeV $4.8_{-0.3}^{+0.5}$ MeV
Quark generation 2	$\begin{pmatrix} c \\ s \end{pmatrix}$	$1.275 \pm 0.025$ GeV $95 \pm 5$ MeV
Quark generation 3	$\begin{pmatrix} t \\ b \end{pmatrix}$	$173.07 \pm 0.52 \pm 0.72$ GeV $4.18 \pm 0.03$ GeV
Lepton generation 1	$\begin{pmatrix} e \\ \nu_e \end{pmatrix}$	0.511 MeV <2.2 eV
Lepton generation 2	$\begin{pmatrix} \mu \\ \nu_\mu \end{pmatrix}$	105.658 MeV <170 keV
Lepton generation 3	$\begin{pmatrix} \tau \\ \nu_\tau \end{pmatrix}$	$1776.82 \pm 0.16$ MeV <15.5 MeV

**Table 3.2:** Masses of the quarks and leptons.

Noticeably, the masses of the three neutrinos altogether are considerably less well defined than the masses of the electron, muon and tau particles (data from the European Space Agency’s Planck space observatory suggests that the combined mass of the three

neutrino flavors  $\sum m_\nu < 0.23$  eV). According to the SM, the neutrinos are completely massless. However, it can be experimentally verified that they do indeed carry a very small mass. The extension of the SM that is most frequently invoked to explain how neutrinos gain (a tiny) mass involves the addition of heavy right-handed neutrinos. A mass-mixing matrix is developed for the neutrinos with various eigenvalues, some very large and others very small. As the right-handed neutrinos increase in size, the left-handed neutrinos decrease in size, accounting for the small experimentally observed masses of left-handed neutrinos. This is commonly known as the “seesaw mechanism” [67]. This mechanism also predicts that right-handed neutrinos are their own anti-particles.

Particles also have a property known as chirality, which means that particle fields have left-handed and right-handed components that behave differently under the weak force. Only the left-handed components transform under  $SU(2)$  and interact via the weak force. Neutrinos in the SM do not have a right-handed component - however, in models of physics beyond the standard model, right-handed neutrinos may be added.

The properties of quarks and leptons are summarised in Table 3.3.

Flavor	$T_{L,R}^3$ (Weak isospin)	$Q = T^3 + Y$ (EM charge)	$SU(3)_C$ (Color $_{L,R}$ )	$SU(2)$	$U(1)_Y$ (Hypercharge $_{L,R}$ )
$\begin{pmatrix} u \\ d \end{pmatrix}, \begin{pmatrix} c \\ s \end{pmatrix}, \begin{pmatrix} t \\ b \end{pmatrix}$	$\frac{1}{2}, 0$ $-\frac{1}{2}, 0$	$\frac{2}{3}$ $-\frac{1}{3}$	<b>3, <math>\bar{3}</math></b>	<b>2, 1</b>	$\frac{1}{6}, \frac{2}{3}$ $\frac{1}{6}, -\frac{1}{3}$
$\begin{pmatrix} \nu_e \\ e^- \end{pmatrix}, \begin{pmatrix} \nu_\mu \\ \mu^- \end{pmatrix}, \begin{pmatrix} \nu_\tau \\ \tau^- \end{pmatrix}$	$\frac{1}{2}, 0$ $-\frac{1}{2}, 0$	0 -1	<b>1, <math>\bar{1}</math></b>	<b>2, 1</b>	$-\frac{1}{2}, 0$ $-\frac{1}{2}, -1$

**Table 3.3:** Quark and lepton properties.

Quarks exhibit a curious phenomenon known as color confinement, which means they are not typically observed in an isolated state but are instead bound as composite particles consisting of two or more quarks (or anti-quarks) known as **hadrons**. Hadrons comprised of three valence quarks are labelled **baryons**; the proton and neutron, once thought to be elementary themselves, are baryons composed of the first generation of quarks ( $uud$  and  $udd$ , giving them their charges of +1 and 0 respectively). Those with a quark-antiquark pair, however, are called **mesons**. So far, baryons and mesons are the only types of hadrons that we have been able to observe. In both cases, the hadron is color-neutral, ie.  $RGB$  or  $R\bar{R}$ .

The valence quarks of all hadrons are surrounded by a sea of particles consisting of

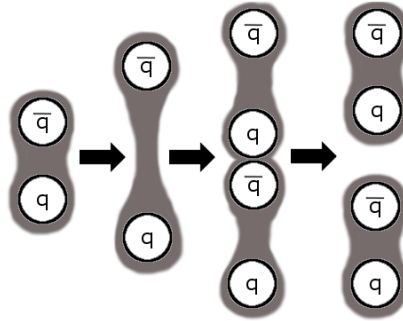


**Figure 3.1:** A diagram illustrating quark color confinement. Attempting to pull two quarks apart results in the production of more bound quarks.

gluons (the force particles governing the interactions between quarks) and many virtual quark-antiquark (up, down or strange) pairs. These quark-antiquarks are generally very unstable compared to the valence quarks, popping spontaneously into existence from a decaying gluon and annihilating with each other almost immediately to produce another gluon.

Free quarks, unbound from hadrons, have not been observed, but the hypothetical case of an extremely hot quark-gluon plasma (consisting of deconfined and free-moving quarks and gluons) was predicted in the early 1970s. This is a result of asymptotic freedom, meaning that the force between quarks and gluons becomes asymptotically weaker with increased energy and distance. In recent years, the properties of quarks and gluons at high temperatures (thought to replicate the cosmic conditions of the very early universe, immediately after the Big Bang) have been explored at the LHC and the Relativistic Heavy Ion Collider (RHIC) by colliding protons with lead and gold nuclei [68]. These experiments have demonstrated that the resultant plasma is actually a strong quark-gluon plasma (sQGP) with fluid-like behaviour instead of a weakly interacting one.

### 3.1.2 Gauge bosons

While matter is composed of fermions, the particles that mediate the fundamental forces of nature are bosons. The fundamental gauge bosons in the SM are:

- The photon  $\gamma$ , an electrically neutral massless spin 1 boson that mediates the electromagnetic force

- The  $W^\pm$  bosons, charged ( $\pm 1$  respectively) spin 1 bosons that mediate the weak force
- The  $Z^0$  boson, a neutral spin 1 boson that also mediates the weak force ( $Z^0$  and  $W^\pm$  are known as the weak or intermediate vector bosons)
- The gluon  $g$ , an electrically neutral massless spin 1 boson that mediates the strong force (there are eight types of gluons, each with a color-anticolor charge)

A boson mediates forces by particle exchange; for example, when two negatively charged particles such as electrons interact, a virtual photon is exchanged between the pair, and the electrons repel (see Fig. 3.2).

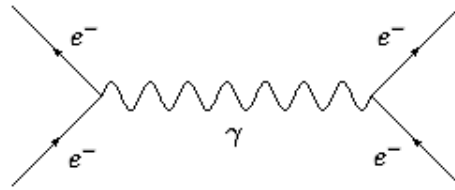


**Figure 3.2:** Feynman diagram depicting electron-electron scattering and virtual photon exchange.

In addition to these force-mediating bosons, there is also a spin 0 boson called the Higgs, which was discovered at the Large Hadron Collider (LHC) in 2012 [62, 63]. This boson is responsible for fermions and gauge bosons gaining mass, as the result of a mechanism which will be outlined in the next subsection.

## 3.2 Electroweak symmetry breaking and the Higgs mechanism

The backbone of the standard model is quantum field theory, in which particles are treated as fields interacting with each other while being governed by a mathematical function known as the Lagrangian. The SM can be split into several sectors: quantum chromodynamics (QCD) governs the theory of interactions between gluons and quarks under a  $SU(3)$  symmetry, while the electromagnetic and weak forces are described by the electroweak sector under symmetry group  $SU(2)_L \times U(1)$ .

The Higgs itself is a complex scalar doublet of  $SU(2)_L$ . This boson was postulated in the 1970s as a mechanism of producing masses for fermions and the weak bosons. It does so via a phenomenon known as spontaneous symmetry breaking (where a ‘symmetry’ of a system is a quantity that remains invariant under some transformation, unless it is broken). To illustrate the basic principle, it is instructive to consider a simple Lagrangian of a set of scalar fields,  $\phi^i(x)$ , with a kinetic term and a potential,

$$\mathcal{L} = \frac{1}{2} (\partial_\mu \phi^i)^2 - V(\phi^i), \quad (3.3)$$

where  $V(\phi^i)$ , the potential, is:

$$V(\phi^i) = -\frac{1}{2} \mu^2 (\phi^i)^2 + \frac{\lambda}{4!} [(\phi^i)^2]^2. \quad (3.4)$$

This potential has a minimum whenever  $(\phi_0^i)^2 = \frac{\mu^2}{\lambda} = v^2$ , where  $v = \frac{\mu}{\sqrt{\lambda}}$  is the vacuum expectation value (VEV). Since we can define the set of scalar fields as a vector with  $n$  components  $(\phi^1, \phi^2, \dots, \phi^n)$ , there are actually any number of solutions that will satisfy this condition, since this is effectively only a constraint on the vector length but not its direction. We can define a new set of fields in terms of their separation from the VEV,  $\sigma^i(x) = (\phi^l(x), v + \sigma(x))$  (with  $l = 1, \dots, n-1$ ), and rewrite the Lagrangian in terms of  $\sigma^i$ :

$$\mathcal{L} = \frac{1}{2} (\partial_\mu \pi^k)^2 + \frac{1}{2} (\partial_\mu \sigma)^2 - \frac{1}{2} (2\mu^2) \sigma^2 - \sqrt{\lambda} \mu \sigma^3 \quad (3.5)$$

$$- \sqrt{\lambda} \mu (\pi^k)^2 \sigma - \frac{\lambda}{4} \sigma^4 - \frac{\lambda}{2} (\pi^k)^2 \sigma^2 - \frac{\lambda}{4} [(\pi^k)]^2. \quad (3.6)$$

We now have a rather interesting situation. The previous Lagrangian had a continuous symmetry in the sense that it remained unchanged under the continuous transformation  $\phi^i \rightarrow R^{ij} \phi^j$ , where  $R^{ij}$  is an  $n \times n$  orthogonal rotation matrix. However, this symmetry has been lost (broken), since the re-written Lagrangian is no longer invariant under  $\sigma^i \rightarrow R^{ij} \sigma^j$ . In addition, instead of a massive field  $\phi$  we now have both a massive field  $\sigma$  and a set of massless  $\pi$  fields.

One can visualise the emergence of these new massless fields by picturing oscillation modes in the potential  $V$  (which is shaped like a Mexican hat - see Fig. 3.3). If a ball is placed upon the central peak, it represents a system that is momentarily symmetric but

unstable. This instability occurs because if it is shifted even slightly closer to one of the troughs (minima), the symmetry is immediately lost as the ball will not return to the peak but will instead roll down to the minimum and up the other side, rolling back and forth. This is a representation of spontaneous supersymmetry breaking. The massive field  $\sigma$  is an oscillation mode in the radial direction. The massless  $\pi$  fields, however, correspond to oscillations along the trough of the potential (picture a ball rolling in a circle at the bottom, without ever rising on the slopes).

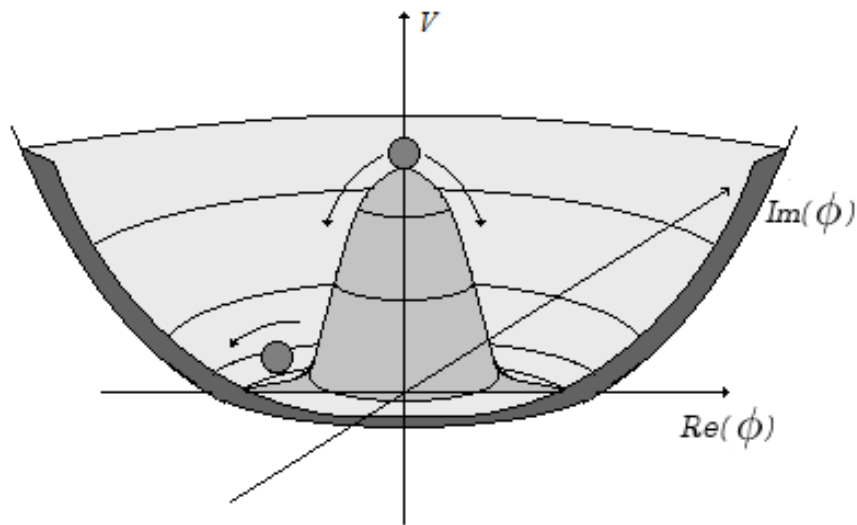


**Figure 3.3:** The Mexican hat potential and modes of stability.

This is illustrative of Goldstone's Theorem, which states that a massless particle (the Nambu-Goldstone particle) will be present for each continuous symmetry that is broken.

This form of spontaneous symmetry breaking was proposed as part of a mechanism for generating masses for the gauge bosons of electroweak theory and developed by various independent teams of scientists in the 1960s [69–71], the result of which was the prediction of the Higgs boson (named after British physicist Peter Higgs). This Higgs mechanism involves the introduction of a complex scalar field  $\phi$  under  $SU(2)$  with four degrees of freedom. After spontaneous symmetry breaking, a gauge transformation converts the massless Goldstone bosons (three of the degrees of freedom of the scalar doublet) into longitudinal components of the massive  $W^\pm$  and  $Z$  bosons. The fourth degree of freedom results in a scalar field that gains its mass through self-interaction (the Higgs boson).

The Lagrangian density of electroweak interactions is given by:

$$\mathcal{L} = -\frac{1}{4}F_{\mu\nu}F^{\mu\nu} - \frac{1}{4}f_{\mu\nu}^l f^{l\mu\nu} + |D_\mu\phi|^2 - V(\phi) + \mathcal{L}_{matter}, \quad (3.7)$$

where  $F_{\mu\nu} = \partial_\mu B_\nu - \partial_\nu B_\mu$  is the field strength tensor of  $A_\mu$  ( $B_\mu$  being the vector field of the  $U(1)_Y$  symmetry),  $f_{\mu\nu}^l = \partial_\nu W_\mu^l - \partial_\mu W_\nu^l + g\epsilon_{jkl}W_\mu^j W_\nu^k$  are the field strength tensors of the three  $SU(2)_W$  gauge symmetry vector fields  $W_\mu^l$  ( $l = 1, 2, 3$ ), and  $D_\mu$  is the covariant derivative,

$$D_\mu = \partial_\mu + \frac{ig'}{2}B_\mu Y + \frac{ig}{2}\sigma^l W_\mu^l, \quad (3.8)$$

with  $Y$  being the hypercharge,  $g$  and  $g'$  being the dimensionless gauge couplings and  $\sigma^l$  being the Pauli matrices:

$$\sigma^1 = \begin{pmatrix} 0 & 1 \\ 1 & 0 \end{pmatrix}, \quad \sigma^2 = \begin{pmatrix} 0 & -i \\ i & 0 \end{pmatrix}, \quad \sigma^3 = \begin{pmatrix} 1 & 0 \\ 0 & -1 \end{pmatrix}. \quad (3.9)$$

Finally,  $V(\phi)$  is a general scalar potential with  $\mu^2 < 0$ ,

$$V(\phi) = \mu^2 |\phi^2\phi| + |\mu| \left( |\phi^\dagger\phi| \right)^2. \quad (3.10)$$

As before, the minimum of this potential results in spontaneous symmetry breaking, with a minimisation condition given by  $|\phi^\dagger\phi| = \frac{v^2}{2}$  (where VEV  $v = \frac{\mu_-}{\sqrt{2\lambda}}$ ). Again as previously, there are an infinite number of solutions that satisfy this condition, but we can choose by convention to define  $\phi_0 = \frac{h+v}{\sqrt{2}}$ , which leads us to a rewritten Lagrangian:

$$\begin{aligned} \mathcal{L} = & \frac{1}{2}\partial^\mu h\partial_\mu h - \mu^2 h^2 + \frac{v^2}{8}Z^\mu + \frac{g^2 v^2}{8} \left( |W_\mu^+|^2 + |W_\mu^-|^2 \right) \\ & - \frac{1}{4} \left( F_{\mu\nu}F^{\mu\nu} + f_{\mu\nu}^l f^{l\mu\nu} \right) + \mathcal{L}_{matter}. \end{aligned} \quad (3.11)$$

Here,  $A_\mu$  is the vector field of the massless photon, given by

$$A_\mu = \frac{gB_\mu + g'W_{3\mu}}{\sqrt{g^2 + g'^2}}, \quad (3.12)$$

while  $Z_\mu$  and  $W_\mu^\pm$  are the fields of the physical gauge bosons,

$$Z_\mu = \frac{gW_\mu^3 - g'B_\mu}{\sqrt{g^2 + g'^2}}, \quad (3.13)$$

$$W_\mu^\pm = \frac{1}{\sqrt{2}}(W_{1\mu} \mp iW_{2\mu}). \quad (3.14)$$

What we can see is a new kinetic and mass term for the Higgs boson,  $\frac{1}{2}\partial^\mu h\partial_\mu h - \mu^2 h^2$ . The gauge bosons  $Z_\mu$  and  $W_\mu^\pm$  have also gained masses of their own. Another way of understanding this is that several of the scalar degrees of freedom have been ‘eaten’ to produce gauge boson masses. Although here we have only shown how the gauge bosons gain their mass, fermions (governed by  $\mathcal{L}_{matter}$ ) will also gain masses via the Higgs mechanism in a very similar way.

### 3.3 Outstanding problems of the standard model

The standard model is undoubtedly a beautiful model that successfully describes many natural phenomena. However, it is not without its flaws, some of which we have already touched upon. Some of the more pressing issues are expounded upon below - the existence of these problems gives us great incentive to look beyond the standard model and explore new physics.

- The Higgs Hierarchy Problem

This is a problem related to the introduction of the Higgs as a way of bestowing mass upon the gauge bosons and fermions. One would expect that the Higgs mass, given by its bare mass plus its self-energy, ought not to lie too far from the mass of the  $W^\pm$  and  $Z$  bosons. However, this picture is complicated by the fact that the self-energy also includes several virtual one-loop corrections from the gauge bosons, making it blow up considerably. In order to keep the Higgs mass  $\mathcal{O}(125 \text{ GeV})$ , the bare mass of the Higgs must be ‘fine tuned’ to such a high degree (13 decimal place precision) that feels rather unnatural in the absence of a physical explanation, since it has to cancel out these large corrections. This is a problem that may be fixed by expanding the SM to include supersymmetry or extra dimensions.

- The Strong CP Problem

CP-symmetry (charge-parity symmetry, which is invariance under interchange of a particle with its antiparticle followed by interchange of handed-ness) is observed to have been violated by weak interactions; however, experimentally this does not seem to be the case for quantum chromodynamic (QCD) interactions, even though there is a term in the QCD Lagrangian that is quite perfectly capable of breaking CP-symmetry,  $\frac{\theta_{QCD}}{32\pi^2} g_s^2 F_{\mu\nu} \tilde{F}^{\mu\nu}$  (where  $g_s$  is the QCD coupling constant and  $\theta_{QCD}$  is the QCD angle). The fact that  $\theta_{QCD}$  must consequently lie very close to zero is yet another fine-tuning problem of the SM.

- The inclusion of gravity

As mentioned, the SM currently only includes three of the four fundamental forces: the weak force, the strong force and the electromagnetic force. Following the ‘recipe book’ and including a massless, spin 2 gauge mediator boson for gravity (usually known as the graviton) does not produce the expected results without considerable modification, since general relativity is not a quantum theory, and is exceedingly difficult to renormalize.

The current best hope for unifying gravity with the rest of the SM appears to lie with string theory (and by extension supersymmetry).

- Unification of the gauge couplings

As it stands, the SM alone does not properly unify its gauge couplings at high energies (see Fig. 3.4). A GUT is a theory that unifies the three fundamental forces of the SM into a single force (if the fourth force, gravity, were also to be included, it would instead be a theory of everything, or TOE) with a universal gauge coupling. The simplest example of a GUT is the  $SU(5)$  group, which contains the three SM gauge groups  $SU(3) \times SU(2) \times U(1)$ . A more complex example is the  $SO(10)$  group, which can be broken down to  $SU(5)$  before breaking down to the three SM groups.

- Neutrino masses

The SM does not by itself provide an explanation for the very small observed masses of the three neutrinos, given that they are theoretically massless. As mentioned previously, one way of rectifying this problem is by employing a seesaw mechanism.

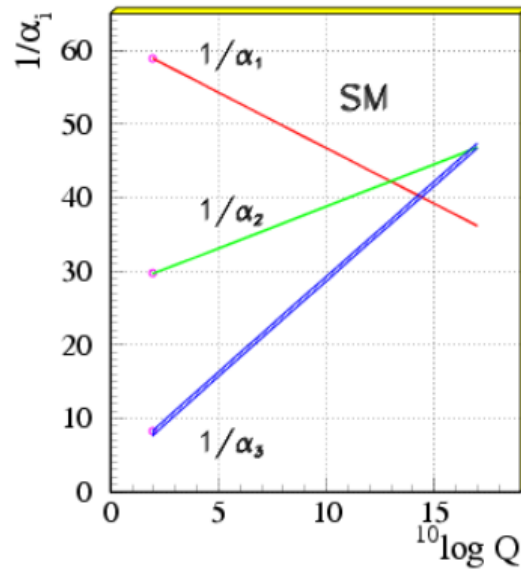


**Figure 3.4:** Running of the gauge couplings in the SM with energy [72]. It is hoped that a complete grand unified theory of physics will unify these forces at high energy.

- Matter-antimatter asymmetry

Matter and antimatter share the same mass, but opposite quantum numbers such as charge and spin. Collisions between them lead to mutual annihilation. However, the Big Bang evidently did not produce an equal amount of baryonic and anti-baryonic matter, as there is vastly more of the former than the latter in the universe. This is known as the baryon asymmetry problem, and there is no explanation for it in the SM.

- Dark matter and dark energy

Finally, as illustrated in the previous chapter, the universe is composed of a vast amount of unknown matter and energy that is entirely unaccounted for in the standard model (the SM can also not account for the accelerated expansion of the universe under the effects of dark energy).

It is this problem that this thesis is devoted to: how supersymmetry may provide the answer to the dark matter conundrum in the form of a light, weakly-interacting particle known as the neutralino.

---

# Supersymmetry

---

## 4.1 Poincaré algebra, No Go theorems and Supermultiplets

In the SM the space-time symmetries are described by the Poincaré group. The associated Poincaré algebra consists of six Lorentz transformations (three rotations and three boosts) and four translations in spacetime, the generators of which are  $M^{\mu\nu}$  and  $P^\mu$  respectively, that satisfy the following commutation relations,

$$[P^\mu, P^\nu] = 0, \quad (4.1)$$

$$[P^\rho, M^{\mu\nu}] = i(\eta^{\mu\rho}P^\nu - \eta^{\nu\rho}P^\mu), \quad (4.2)$$

$$[M^{\mu\nu}, M^{\rho\sigma}] = i(\eta^{\mu\rho}M^{\nu\sigma} - \eta^{\mu\sigma}M^{\nu\rho} + \eta^{\nu\sigma}M^{\mu\rho} - \eta^{\nu\rho}M^{\mu\sigma}), \quad (4.3)$$

where  $\eta^{\mu\nu}$  is the metric (-1,1,1,1) and  $\mu, \nu = 0, 1, 2, 3$ . An infinitesimal transformation (acting upon a 4-vector representing a position in spacetime,  $x^\mu = (ct, x^1, x^2, x^3)$ ) that combines the ten generators is represented by:

$$U(\delta + \omega, \epsilon) = 1 + i\epsilon^\mu P_\mu - \frac{i}{2}\omega^{\mu\nu}M_{\mu\nu}. \quad (4.4)$$

For a scalar field,  $P^\mu$  and  $M^{\mu\nu}$  take the form:

$$P^\mu = i\partial^\mu, \quad (4.5)$$

$$M^{\mu\nu} = i(x^\mu\partial^\nu - x^\nu\partial^\mu). \quad (4.6)$$

For a spinor they are very similar; the only difference is that  $M^{\mu\nu}$  has an additional  $\frac{i}{4}[\gamma^\mu, \gamma^\nu]$  term, making it  $M^{\mu\nu} = i(x^\mu\partial^\nu - x^\nu\partial^\mu) + \frac{i}{4}[\gamma^\mu, \gamma^\nu]$ .  $\gamma^\mu$  are the four gamma

matrices, defined by:

$$\begin{aligned}
 \gamma^0 &= \begin{pmatrix} 1 & 0 & 0 & 0 \\ 0 & 1 & 0 & 0 \\ 0 & 0 & -1 & 0 \\ 0 & 0 & 0 & -1 \end{pmatrix}, & \gamma^1 &= \begin{pmatrix} 0 & 0 & 0 & 1 \\ 0 & 0 & 1 & 0 \\ 0 & -1 & 0 & 0 \\ -1 & 0 & 0 & 0 \end{pmatrix}, \\
 \gamma^2 &= \begin{pmatrix} 0 & 0 & 0 & -i \\ 0 & 0 & i & 0 \\ 0 & i & 0 & 0 \\ -i & 0 & 0 & 0 \end{pmatrix}, & \gamma^3 &= \begin{pmatrix} 0 & 0 & 1 & 0 \\ 0 & 0 & 0 & -1 \\ -1 & 0 & 0 & 0 \\ 0 & 1 & 0 & 0 \end{pmatrix}.
 \end{aligned} \tag{4.7}$$

In the quest for physics beyond the standard model, a highly pertinent concern is which new symmetries may be successfully added to the SM by extending this algebra. As already established in an earlier chapter, a system has a symmetry if it retains a particular property after a transformation. These symmetries may be discrete or continuous - for instance, an equilateral triangle is symmetric (looks the same) under discrete rotations of  $60^\circ$  about its centre, whereas a circle is continuously symmetric under *any* rotation about its centre.

As it transpires, supersymmetry is the only non-trivial space-time extension of the existing Poincaré symmetry, as a result of the Coleman-Mandula No Go Theorem [73]. Formulated in 1967 and applying to Lie algebras, this theorem stipulates that it “is impossible to combine space-time and internal symmetries in any but a trivial way.” Suppose that we have some connected symmetry group  $\mathcal{H}$  that satisfies the following physical assumptions:

- Any two plane waves scatter at almost all energies
- The elastic-scattering amplitudes are analytic functions of the centre of mass energy and of the momentum transfer in some neighbourhood of the physical region
- There are only a finite number of particle types with mass less than  $M$  (for any  $M$ ).

The only generators of  $\mathcal{H}$  that are then possible are the generators of its Poincaré group  $H$  (ie. the generators satisfying the commutation relations in Eq. 4.1, Eq. 4.2 and Eq. 4.3), in addition to internal symmetry generators that commute with these. However, this was extended in a 1975 paper by Haag, Lopuszanski and Sohnius [74], who demonstrated that supersymmetry provides a ‘loophole’ of sorts and is the only non-trivial extension. The result of this extension is a beautiful and elegant symmetry between fermions and bosons [75–78] under the action of some anti-commuting spinor operator  $\mathcal{Q}$ :

$$Q|\text{Fermion}\rangle = |\text{Boson}\rangle, \quad Q|\text{Boson}\rangle = |\text{Fermion}\rangle. \quad (4.8)$$

For  $N = 1$  supersymmetry (where  $N$  is the number of supersymmetries<sup>1</sup>), the additional generators that may be added to the Poincaré algebra,  $\mathcal{Q}$  and  $\bar{\mathcal{Q}}$ , have the following commutation and anticommutation properties ( $\mu, \nu = 0, 1, 2, 3$ ,  $\alpha, \beta = 1, 2$ ):

$$[\mathcal{Q}_\alpha, P^\mu] = 0, \quad (4.9)$$

$$[\mathcal{Q}_\alpha, M^{\mu\nu}] = i(\sigma^{\mu\nu})_\alpha^\beta \mathcal{Q}_\beta, \quad (4.10)$$

$$\{\mathcal{Q}_\alpha, \bar{\mathcal{Q}}_{\dot{\beta}}\} = 2(\sigma^\mu)_{\alpha\dot{\beta}} P_\mu, \quad (4.11)$$

$$\{\mathcal{Q}_\alpha, \mathcal{Q}_\beta\} = \{\bar{\mathcal{Q}}_{\dot{\alpha}}, \bar{\mathcal{Q}}_{\dot{\beta}}\} = 0. \quad (4.12)$$

The irreducible representations of the SUSY algebra are known as supermultiplets, and contain both fermionic and bosonic components. The  $\mathcal{Q}$  operators act on these by decreasing spin by  $\frac{1}{2}$  ( $\mathcal{Q}_1$ ) or increasing spin by  $\frac{1}{2}$  ( $\mathcal{Q}_2$ ). Each supermultiplet state contains the same number of bosonic and fermionic degrees of freedom, as demonstrated:

$$\begin{aligned} \sum_n \langle n|(-1)^{2s} P^\mu |n\rangle &= \sum_n \langle n|(-1)^{2s} \mathcal{Q}\bar{\mathcal{Q}}|n\rangle + \sum_n \langle n|(-1)^{2s} \bar{\mathcal{Q}}\mathcal{Q}|n\rangle \\ &= \sum_n \langle n|(-1)^{2s} \mathcal{Q}\bar{\mathcal{Q}}|n\rangle + \sum_n \sum_m \langle n|(-1)^{2s} \bar{\mathcal{Q}}|m\rangle \langle m|\mathcal{Q}|n\rangle \\ &= \sum_n \langle n|(-1)^{2s} \mathcal{Q}\bar{\mathcal{Q}}|n\rangle + \sum_m \langle m|\mathcal{Q}(-1)^{2s} \bar{\mathcal{Q}}|m\rangle \\ &= \sum_n \langle n|(-1)^{2s} \mathcal{Q}\bar{\mathcal{Q}}|n\rangle - \sum_m \langle m|(-1)^{2s} \mathcal{Q}\bar{\mathcal{Q}}|m\rangle \\ &= 0. \end{aligned} \quad (4.13)$$

<sup>1</sup>When  $N > 1$  the algebra is called an extended supersymmetry.

Here, we have used the knowledge that, since the fermionic operator  $\mathcal{Q}$  turns a boson into a fermion or a fermion into a boson, the spin angular momentum operator  $(-1)^{2s}$  (which is  $+1$  when acting on a bosonic state and  $-1$  when acting on a fermionic state) must anticommute with both  $\mathcal{Q}$  and  $\bar{\mathcal{Q}}$ . Furthermore, the identity  $\sum_n |n\rangle\langle n| = 1$  may be inserted as in the second and third steps.

Since the LHS of Eq. (4.13) is directly proportional to the number of bosonic degrees of freedom minus the number of fermionic degrees of freedom, we thus have the result

$$n_B = n_F. \quad (4.14)$$

The consequences of this result are rather interesting. The fermion and boson states of a supermultiplet are known as superpartners, each different by spin  $\frac{1}{2}$ . By convention, these are typically referred to by adding an “s” prefix to the particle name (for example, the superpartners of leptons are called sleptons, the superpartners of quarks are known as squarks, and so on) or by appending “-ino” (for example, the fermionic partners of gauge bosons are known as gauginos).

Furthermore, superpartners in an unbroken supersymmetry must have the same masses as each other. This follows from the fact that  $[\mathcal{Q}, P^2] = 0$  - all particles in the same multiplet have the same  $P^2$  eigenvalue, and consequently the same mass. However, this is not what is observed in reality; if superpartners had the same masses as the matter that currently make up the standard model, we would have seen them by now in detection experiments. Clearly, supersymmetry must be broken at high energies if it is to be viable.

## 4.2 Superspace and superfields

Minkowski space-time, spanned ordinarily by the 4-vector  $x^\mu$ , is extended in supersymmetry to a superspace with coordinates  $x^\mu, \theta^\alpha, \bar{\theta}_{\dot{\alpha}}$ , where  $\theta^\alpha$  and  $\bar{\theta}_{\dot{\alpha}}$  ( $\alpha = 1, 2$ ) are fermionic two-component spinors and Grassmann variables with dimensions  $[\text{mass}]^{-\frac{1}{2}}$  satisfying the

following<sup>2</sup>:

$$\{\theta^\alpha, \theta^\beta\} = \{\bar{\theta}_{\dot{\alpha}}, \bar{\theta}_{\dot{\beta}}\} = \{\theta^\alpha, \bar{\theta}_{\dot{\alpha}}\} = 0, \quad (4.15)$$

$$[x^\mu, \theta^\alpha] = [x^\mu, \bar{\theta}_{\dot{\alpha}}] = 0, \quad (4.16)$$

$$\theta\theta = \theta^\alpha\theta_\alpha = \epsilon^{\alpha\beta}\theta_\beta\theta_\alpha = \theta^1\theta_1 + \theta^2\theta_2 = -\theta_1\theta^1 - \theta_2\theta^2, \quad (4.17)$$

$$(\theta^1)^2 = (\theta^2)^2 = (\bar{\theta}_1)^2 = (\bar{\theta}_2)^2 = 0, \quad (4.18)$$

$$\theta^\alpha\theta^\beta = -\frac{1}{2}\epsilon^{\alpha\beta}\theta\theta, \quad (4.19)$$

$$\bar{\theta}_{\dot{\alpha}}\bar{\theta}_{\dot{\beta}} = -\frac{1}{2}\epsilon_{\dot{\alpha}\dot{\beta}}\bar{\theta}\bar{\theta}. \quad (4.20)$$

Due to Eq. (4.18), any term can only contain at most two  $\theta$  and two  $\bar{\theta}$  fields - multiplying these by  $\theta$ ,  $\bar{\theta}$  or any higher orders of  $(\theta, \bar{\theta})$  will result in zero. Thus, the most general combination of  $\theta$  and  $\bar{\theta}$  follows the pattern:

$$s(\theta, \bar{\theta}) = a + b^\alpha\theta_\alpha + \bar{c}_{\dot{\alpha}}\bar{\theta}^{\dot{\alpha}} + d\theta\theta + e\bar{\theta}\bar{\theta} + (f^\alpha\theta_\alpha + \bar{g}_{\dot{\alpha}}\bar{\theta}^{\dot{\alpha}})(\theta\theta + \bar{\theta}\bar{\theta}) + h(\theta\theta)(\bar{\theta}\bar{\theta}). \quad (4.21)$$

A superfield is a field defined on this superspace, with the most generic possible form:

$$\begin{aligned} S(x, \theta, \bar{\theta}) &= \phi(x) + \theta\eta(x) + \bar{\theta}\bar{\chi}(x) + \theta^2m(x) + \bar{\theta}^2n(x) + \theta\sigma^\mu\bar{\theta}V_\mu(x) \\ &+ \theta^2\bar{\theta}\bar{\lambda}(x) + \bar{\theta}^2\theta\psi(x) + \theta^2\bar{\theta}^2D(x). \end{aligned} \quad (4.22)$$

Here,  $\phi(x), m(x), n(x)$  and  $D(x)$  are scalar fields,  $\eta(x), \bar{\chi}(x), \bar{\lambda}(x)$  and  $\psi(x)$  are spinors and  $V_\mu(x)$  is a vector field. However, chiral and vector superfields take different forms in accordance with differing constraints. For instance, in the case of chiral and anti-chiral superfields  $\Phi$  and  $\Phi^\dagger$  respectively, the constraints

$$\bar{D}_{\dot{\alpha}}\Phi = 0, \quad (4.23)$$

$$D_\alpha\Phi^\dagger = 0, \quad (4.24)$$

---

<sup>2</sup> $\epsilon^{\alpha\beta}$  is an antisymmetric symbol that raises or lowers indices:  $\epsilon^{12} = -\epsilon^{21} = \epsilon_{12} = -\epsilon_{21} = 1$  and  $\epsilon^{11} = \epsilon^{22} = \epsilon_{11} = \epsilon_{22} = 0$ .

are applied, where

$$D_\alpha = \frac{\partial}{\partial\theta^\alpha} - i(\sigma^\mu\theta^\dagger)_\alpha\partial_\mu, \quad (4.25)$$

$$\bar{D}_{\dot{\alpha}} = -\frac{\partial}{\partial\bar{\theta}^{\dot{\alpha}}} + i(\theta\sigma^\mu)_{\dot{\alpha}}\partial_\mu, \quad (4.26)$$

are chiral covariant derivatives. One solution is the following general form for a chiral superfield:

$$\begin{aligned} \Phi &= \phi(x) + i\bar{\theta}\bar{\sigma}^\mu\theta\partial_\mu\phi(x) + \frac{1}{4}\theta^2\bar{\theta}^2\partial_\mu\partial^\mu\phi(x) + \sqrt{2}\theta\psi(x) \\ &- \frac{i}{\sqrt{2}}\theta^2\bar{\theta}\bar{\sigma}^\mu\partial_\mu\psi(x) + \theta^2F(x). \end{aligned} \quad (4.27)$$

It may be more convenient to rewrite this by transforming the  $x^\mu$  coordinate such that the field takes a more simple form depending only on  $x'$  and one Grassman coordinate (this also results in a simplification for the supersymmetry charges for chiral and anti-chiral fields):

$$x^\mu \rightarrow x'^\mu = x^\mu + i\bar{\theta}\bar{\sigma}^\mu\theta, \quad (4.28)$$

$$\Phi \rightarrow \Phi = \phi(x') + \sqrt{2}\theta\phi(x') + \theta^2F(x'), \quad (4.29)$$

$$\Phi^\dagger \rightarrow \Phi^\dagger = \phi^\dagger(y^*) + \sqrt{2}\bar{\theta}\bar{\phi}(y^*) + \bar{\theta}\bar{\theta}F^\dagger(y^*). \quad (4.30)$$

The last  $\theta^2$  term is referred to as the  $F$ -term, which plays a role in supersymmetry breaking. On the other hand, a vector superfield is defined by the constraint  $V = V^\dagger$  (ie. real), such that all the components of  $V$  are components of a vector supermultiplet. This constraint results in the general form:

$$\begin{aligned} V(x, \theta, \bar{\theta}) &= \phi(x) + i\theta\chi(x) - i\bar{\theta}\bar{\chi}(x) + \frac{i}{2}\theta^2[A(x) + B(x)] - \frac{i}{2}\bar{\theta}^2[A(x) + B(x)] - \theta\sigma^\mu\bar{\theta}V_\mu(x) \\ &+ i\theta^2\bar{\theta}\left[\bar{\lambda}(x) + \frac{i}{2}\bar{\sigma}^\mu\partial_\mu\chi(x)\right] - i\bar{\theta}^2\theta\left[\lambda(x) + \frac{i}{2}\sigma^\mu\partial_\mu\bar{\chi}(x)\right] + \frac{1}{2}\theta^2\bar{\theta}^2[D(x) \\ &+ \frac{1}{2}\partial_\mu\partial^\mu\phi(x)]. \end{aligned} \quad (4.31)$$

We can simplify this by choosing a gauge such that the auxiliary fields  $\phi(x)$ ,  $\chi(x)$ ,  $A(x)$  and  $B(x)$  completely vanish. This is known as the Wess-Zumino gauge, and results in a

superfield with a gauge boson, a gaugino and an auxiliary field respectively:

$$V_{\text{WZ gauge}}(x, \theta, \bar{\theta}) = -\theta\sigma^\mu\bar{\theta}V_\mu(x) + i\theta^2\bar{\theta}\lambda(x) - i\bar{\theta}^2\theta\lambda(x) + \frac{1}{2}\theta^2\bar{\theta}^2D(x). \quad (4.32)$$

The last term is known as the  $D$ -term, and like the  $F$ -term of chiral superfields also has a role in supersymmetry breaking. Under the WZ gauge this vector field is no longer supersymmetric, as performing a supersymmetry transformation on it takes it out of WZ gauge; however, it can be restored back to a WZ gauge with an additional supergauge transformation [76].

Since the volume element of our superspace is  $d^4x d^2\theta d^2\bar{\theta}$ , a supersymmetric action (which must be invariant under any supersymmetry transformation) is the following integral of a superfield:

$$A = \int d^4x \int d^2\theta d^2\bar{\theta} S(x, \theta, \bar{\theta}). \quad (4.33)$$

An action over two  $\theta$  and two  $\bar{\theta}$  coordinates is known as a  $D$ -type action; an  $F$ -type action is an integral over a six-dimensional volume space  $d^4x d^2\theta$  or  $d^4x d^2\bar{\theta}$  on superfields in which  $\theta$  and  $\bar{\theta}$  only appear in terms containing spatial derivatives (ie. chiral superfields) [77].

A Lagrangian density (which is a function of  $x$ ) may be subsequently obtained by integrating over the Grassmann coordinates only. There are multiple ways to do this. If we integrate a vector superfield over both  $\theta$  and  $\bar{\theta}$ , the  $D$ -term contribution to the Lagrangian is as follows (only the last term in Eq. 4.31 is singled out, as it had both  $\theta^2$  and  $\bar{\theta}^2$  coordinates):

$$V(x, \theta, \bar{\theta}) \Big|_{\theta\theta\bar{\theta}\bar{\theta}} = \int d^\theta d^{\bar{\theta}} V(x, \theta, \bar{\theta}) = \frac{1}{2}D + \frac{1}{4}\partial_\mu\partial^\mu\phi. \quad (4.34)$$

The alternate  $F$ -type contribution (which must be paired with its complex conjugate in order to ensure that it is real and not complex) to the Lagrangian is obtained by integrating over  $\theta$  only:

$$\Phi \Big|_{\theta\theta} = \int d^2\theta \Phi \Big|_{\bar{\theta}=0} = F. \quad (4.35)$$

These three components (the  $D$ -term of a vector superfield, the  $F$ -term of a chiral superfield and its complex conjugate) can all be used to build a supersymmetrically invariant Lagrangian.

### 4.3 Supersymmetry breaking

Since we do not observe SUSY mirror particles at the same energies as SM particles, supersymmetry must be broken in order to introduce a mass asymmetry between particles and sparticles.

There are two main types of supersymmetry breaking:

- *Explicit SUSY breaking*: This occurs when terms are added to the Lagrangian that are not invariant under SUSY transformations.
- *Spontaneous SUSY breaking*: This occurs when the vacuum state is allowed to be non-invariant under SUSY, meaning that  $Q|0\rangle \neq 0$  (and  $\langle 0|H|0\rangle > 0$ ). Since  $V = |F|^2 + \frac{1}{4}D^2$ , the vacuum state has non-zero energy and SUSY is broken when either  $\langle D\rangle \neq 0$  ( $D$ -type breaking) or  $\langle F\rangle \neq 0$  ( $F$ -type breaking), or both.

The former has an additional complication, since we must ensure that the extra SUSY-breaking terms do not also spoil desirable predictive features of the supersymmetric model (such as cancelling power-law divergences). For this reason, explicit SUSY breaking takes the form of what is known as *soft supersymmetry breaking*.

However, we will first review the two mechanisms of spontaneous SUSY breaking. Spontaneous SUSY breaking can be illustrated by a simple scalar potential, as shown in the various examples in Fig. 4.1. The first potential, Fig. 4.1(a), is one in which neither supersymmetry nor any internal gauge symmetry is spontaneously broken. Fig. 4.1(b) introduces an offset that lifts the minimum away from zero and thus breaks SUSY; however, since the potential is still minimized for  $\langle \phi \rangle = 0$  no internal symmetries are broken (unlike the converse, in Fig. 4.1(c)). Fig. 4.1(d) breaks all symmetries.

#### 4.3.1 $D$ -type supersymmetry breaking

The  $D$ -type (or Fayet-Iliopoulos) mechanism occurs when  $\langle D \rangle \neq 0$ . This mechanism occurs when an additional linear term, gauge-invariant and supersymmetric, is added to the Lagrangian in order to gain the result  $\langle D \rangle \neq 0$ ,

$$\mathcal{L}_{\text{Fayet-Iliopoulos}} = \kappa^2 D, \quad (4.36)$$

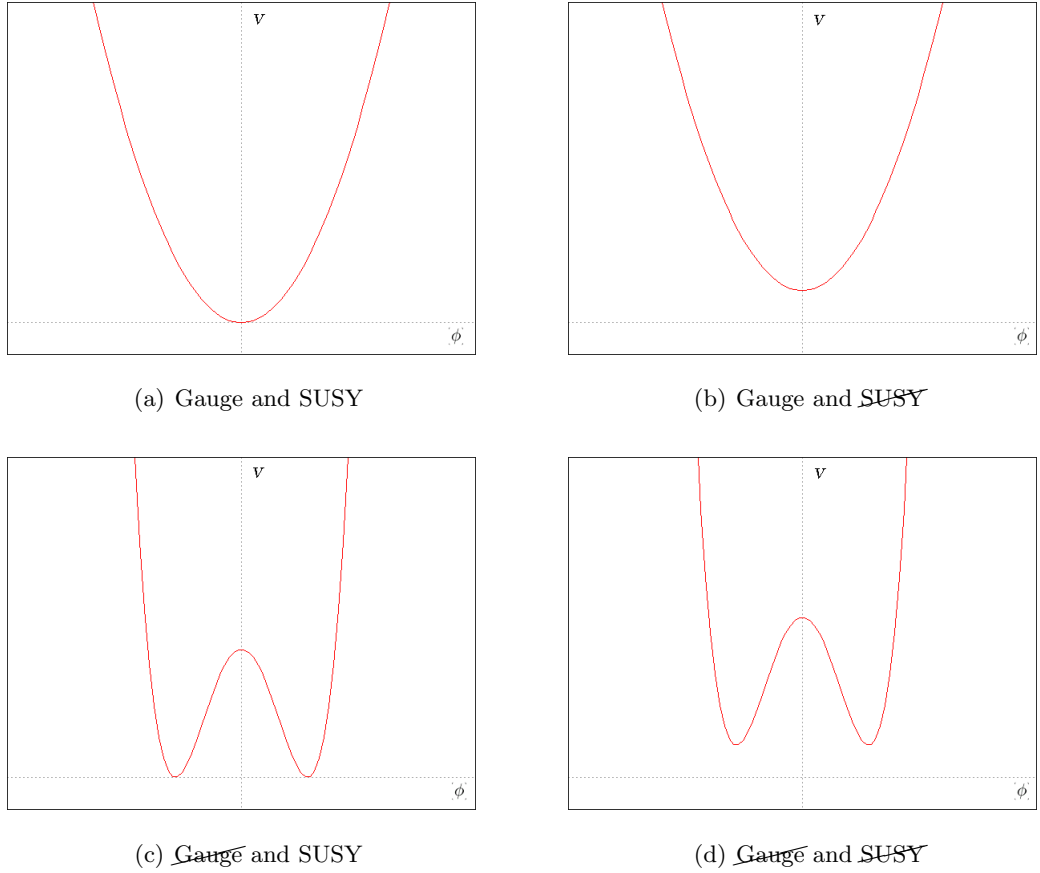


**Figure 4.1:** Various potentials demonstrating the breaking (or not) of internal symmetries and SUSY

where  $\kappa$  has dimensions of mass and is constant. The scalar potential, with  $q_i$  being the charges of scalar fields  $\phi_i$  under gauge group  $U(1)$ , is

$$V = -\kappa^2 D + \frac{1}{2} D^2 + gD \sum_i q_i |\phi_i|^2, \quad (4.37)$$

and  $D$  becomes

$$D = \kappa^2 - g \sum_i q_i |\phi_i|^2. \quad (4.38)$$

### 4.3.2 $F$ -type supersymmetry breaking

The  $F$ -type (or O’Raifeartaigh) mechanism occurs when  $\langle F \rangle = -\frac{\partial W}{\partial \phi} \neq 0$ . O’Raifeartaigh introduced a simple superpotential that satisfies this condition:

$$W = m\Phi_1\Phi_2 + g\Phi_3(\Phi_2^2 - M^2). \quad (4.39)$$

Differentiating with respect to each  $\Phi_i$  leads to three equations for  $F_i$ :

$$F_1 = -m\bar{\Phi}_2, \quad (4.40)$$

$$F_2 = -m\Phi_1 - 2g\Phi_2\bar{\Phi}_2, \quad (4.41)$$

$$F_3 = -g(\Phi_2^2 - M^2). \quad (4.42)$$

The supersymmetry has been spontaneously broken, since there is no solution for which  $F_1 = F_2 = F_3 = 0$ , and indeed it is possible to check this is the case by checking the potential  $V$  to confirm that the masses are degenerate - for instance, the masses of the fermions are

$$m_f = \sqrt{g^2 \langle \phi_3 \rangle^2 + m^2} \pm g \langle \phi_3 \rangle, \quad (4.43)$$

which for  $\langle \phi_3 \rangle = 0$  yields mass  $m$ .

### 4.3.3 Soft supersymmetry breaking

However,  $F$ - and  $D$ -type supersymmetry breaking schemes on the states we know unfortunately do not lead to a viable particle spectrum [76]. Introducing new supermultiplets with tree level couplings to the MSSM and attempting to achieve supersymmetry breaking this way leads to additional problems, such as squark and gluon masses that fall below experimental constraints and should thus have already been observed. This means that a separate and hidden soft explicit SUSY breaking sector is also necessary, which indirectly transmits the supersymmetry breaking to the rest of the MSSM (the visible sector). This hidden sector is at its own energy scale, consists of gauge singlet SM superfields, and couples only very weakly (and flavor-blindly) with the visible sector [75].

The details of this mechanism are not especially important for this discussion, but there are three main scenarios developed to describe this phenomenon. One is called Planck-scale (or gravity) mediated supersymmetry breaking (PMSB), in which the mediating interactions occur due to the gravity force near the Planck mass scale. Another is called gauge mediated supersymmetry breaking (GMSB), in which the hidden sector and visible sector communicate via messenger chiral supermultiplet interactions [79]. A third is anomaly mediated supersymmetry breaking (AMSB), which is a variation of PMSB in which the supersymmetry breaking is transmitted via the super-Weyl anomaly [80].

Explicit SUSY breaking involves the addition of new terms to the Lagrangian which must not reintroduce unwanted ultraviolet divergences (hence, ‘soft’ breaking). They must also comply with mass dimensional constraints. In practice, this means that each field operator in the added terms will have a mass dimension less than four.

In a general theory, the most general possible soft SUSY breaking terms are

$$\mathcal{L} = -(m^2)_j^i \phi^{*j} \phi_i - \left( \frac{1}{2} M_a \lambda^a \lambda^a + \frac{1}{3!} a^{ijk} \phi_i \phi_j \phi_k + \frac{1}{2} b^{ij} \phi_i \phi_j + h.c. \right). \quad (4.44)$$

These terms represent a scalar mass squared term, a trilinear scalar interaction, a bilinear scalar coupling, a tadpole scalar and a gaugino mass term for each gauge group respectively ( $\lambda^a$  is a two-component gaugino field,  $M$  is the gaugino mass,  $m$  is the scalar mass and  $\phi_i$  is the scalar part of the superfield  $\Phi_i$ ). It is worth noting that an additional soft term involving a trilinear coupling in  $\phi^{*i}$ ,  $\phi_j$  and  $\phi_k$  may also be added - however, this actually does introduce ultraviolet divergences under certain conditions.

## 4.4 The Minimal Supersymmetric Standard Model

The most basic possible extension of the standard model to include supersymmetry is known as the Minimal Supersymmetric Standard Model (MSSM), first proposed in 1981 [81]. The existing SM particles (or their left/right states, given their different gauge transformation properties) are embedded into supermultiplets also containing their superpartners; for instance, leptons have complex scalar partners known as sleptons (with each slepton corresponding to the left or right-handed state of its equivalent lepton). The gauge group of the MSSM is  $SU_c(3) \otimes SU_L(2) \otimes U_Y(1)$  (the same as that of the SM).

Table 4.4 gives an overview of the particle content of the MSSM, including the supersymmetric partners of the quarks, leptons, gauge bosons and Higgs bosons. Notably, there are now two Higgs doublets instead of the standard single  $SU_L(2)$  doublet field  $\phi$  of the SM. The Higgs sector of the MSSM is more complicated owing to the fact that the Higgs VEV gives rise to the masses of fermions. In a supersymmetric theory, since interaction terms cannot contain both the Higgs field  $\phi$  and its anti-chiral conjugate  $\phi^\dagger$ , up-type (or down-type) quarks may only derive their masses from a single Higgs doublet, so a second doublet is required to give masses to quarks of the opposite type. Furthermore, two

	Quarks, squarks	Leptons, sleptons	Higgs, Higgsinos	Gauge bosons, gauginos
Spin 0	$\tilde{Q} = (\tilde{u}_L, \tilde{d}_L)$ $\tilde{u}_R^*$ $\tilde{d}_R^*$	$\tilde{L} = (\tilde{\nu}, \tilde{l}_L)$ $\tilde{l}_R^*$	$H_u = (H_u^+, H_u^0)$ $H_d = (H_d^0, H_d^-)$	-
Spin $\frac{1}{2}$	$Q = (u_L, d_L)$ $u_R^\dagger$ $d_R^\dagger$	$L = (\nu, l_L)$ $l_R^\dagger$	$\tilde{H}_u = (\tilde{H}_u^+, \tilde{H}_u^0)$ $\tilde{H}_d = (\tilde{H}_d^0, \tilde{H}_d^-)$	$\tilde{B}$ $\tilde{W}^\pm, \tilde{W}^0$ $\tilde{g}$
Spin 1	-	-	-	$B$ $W^\pm, W^0$ $g$
$SU_c(3) \otimes SU_L(2) \otimes U_Y(1)$	$(3, 2, \frac{1}{3})$ $(\bar{3}, 1, -\frac{4}{3})$ $(\bar{3}, 1, \frac{2}{3})$	$(1, 2, -1)$ $(1, 1, 2)$	$(1, 2, 1)$ $(1, 2, -1)$	$(1, 1, 0)$ $(1, 3, 0)$ $(8, 1, 0)$

**Table 4.1:** Particles of the MSSM.

Higgs doublets are required for proper cancellation of gauge anomalies associated with the fermionic Higgsinos.

Compared to the SM, the MSSM has a greatly expanded quantity of parameters following the breaking of SUSY, making exploration of its features incredibly difficult. However, if the MSSM is constrained such that unification of various masses is achieved at the GUT scale, the number of parameters is greatly reduced. In one such scenario (the CMSSM),  $m_0$ ,  $M_{1/2}$  and  $A_0$  are the unified scalar mass, gaugino mass and scalar trilinear coupling respectively at MGUT:

$$\begin{aligned}
m_0^2 &= m_{H_u}^2 = m_{H_d}^2 = M_Q^2 = M_U^2 = M_D^2 = M_L^2 = M_R^2, \\
M_{1/2} &= M_1 = M_2 = M_3, \\
A_0 &= A_u = A_d = A_t.
\end{aligned} \tag{4.45}$$

Two final free parameters in the CMSSM are  $\tan\beta$  (the ratio between the up-type and down-type neutral Higgs vacuum expectation values  $v_u$  and  $v_d$ ), and the sign of  $\mu$ . One may further specify the bilinear coupling parameter  $B_0$  such that  $B_0 = A_0 - m_0$ , in which case  $\tan\beta$  is no longer freely varying - this is known as the minimal supergravity model (mSUGRA)<sup>3</sup> [82].

<sup>3</sup>However, some authors use the terms CMSSM and mSUGRA interchangeably.

## 4.5 MSSM Lagrangian

The Lagrangian of the MSSM is built from several separate components:

- Kinetic terms for matter, Higgs fields, gauge bosons and gauginos
- Superpotential with Yukawa interactions and self-interactions
- Supersymmetry breaking terms

The kinetic terms are gained from the Kähler potential  $K$ , a real supergauge invariant function of chiral and anti-chiral superfields that is typically written at tree-level as:

$$K = \Phi_i \Phi^{i\dagger}. \quad (4.46)$$

The superpotential of the MSSM is:

$$\begin{aligned} W_{\text{MSSM}} &= y_U^{ij} Q_i u_j^c H_u + y_d^{ij} Q_i d_j^c H_d + y_l^{ij} L_i l_j^c H_d + \mu H_u H_d \\ &= \frac{1}{2} \lambda^{ijk} L_i L_j \bar{e}_k + \lambda'^{ijk} L_i Q_j \bar{d}_k + \mu^i L_i H_u + \frac{1}{2} \lambda''^{ijk} \bar{u}_i \bar{d}_j \bar{d}_k. \end{aligned} \quad (4.47)$$

Here, the Yukawa coupling parameters  $y_u$ ,  $y_d$  and  $y_l$  are dimensionless  $3 \times 3$  matrices that determine the current masses of the quarks and leptons. These are frequently approximated so that only the three heaviest fermions (top quark, bottom quark and tau lepton) are represented. In this approximation, the MSSM superpotential is reduced to contain only the Higgs and third family contributions:

$$y_u \approx \begin{pmatrix} 0 & 0 & 0 \\ 0 & 0 & 0 \\ 0 & 0 & y_t \end{pmatrix}, \quad y_d \approx \begin{pmatrix} 0 & 0 & 0 \\ 0 & 0 & 0 \\ 0 & 0 & y_b \end{pmatrix}, \quad y_l \approx \begin{pmatrix} 0 & 0 & 0 \\ 0 & 0 & 0 \\ 0 & 0 & y_\tau \end{pmatrix}. \quad (4.48)$$

The soft SUSY breaking Lagrangian is:

$$\begin{aligned}
\mathcal{L}_{soft}^{MSSM} &= -\frac{1}{2} \left( M_3 \tilde{g} \tilde{g} + M_2 \tilde{W} \tilde{W} + M_1 \tilde{B} \tilde{B} \right) + \text{c.c.} \\
&- \left( \tilde{u} \mathbf{a}_u \tilde{Q} H_u - \tilde{d} \mathbf{a}_d \tilde{Q} H_d - \tilde{e} \mathbf{a}_e \tilde{L} H_d \right) + \text{c.c.} \\
&- \tilde{Q}^\dagger \mathbf{m}_Q^2 \tilde{Q} - \tilde{L}^\dagger \mathbf{m}_L^2 \tilde{L} - \tilde{u} \mathbf{m}_u^2 \tilde{u}^\dagger - \tilde{d} \mathbf{m}_d^2 \tilde{d}^\dagger - \tilde{e} \mathbf{m}_e^2 \tilde{e}^\dagger \\
&- m_{H_u}^2 H_u^* H_u - m_{H_d}^2 H_d^* H_d - (b H_u H_d + \text{c.c.}). \tag{4.49}
\end{aligned}$$

## 4.6 Neutralinos and charginos

Due to electroweak symmetry breaking the mass eigenstates of binos, winos and Higgsinos can be linearly combined to form composite particles known as charginos (comprised of charged winos and Higgsinos) and neutralinos (comprised of neutral gauginos and Higgsinos).

The chargino states,  $\psi^+ = (\tilde{W}^+, \tilde{H}_u^+)$  and  $\psi^- = (\tilde{W}^-, \tilde{H}_d^-)$ , have a mass mixing matrix given by

$$M_{\tilde{C}} = \begin{pmatrix} 0 & 0 & M_2 & \frac{1}{\sqrt{2}} g v_d \\ 0 & 0 & \frac{1}{\sqrt{2}} g v_u & \mu \\ M_2 & \frac{1}{\sqrt{2}} g v_u & 0 & 0 \\ \frac{1}{\sqrt{2}} g v_d & \mu & 0 & 0 \end{pmatrix}. \tag{4.50}$$

This may also be written as  $M_{\tilde{C}} = \begin{pmatrix} \mathbf{0} & \mathbf{X}^T \\ \mathbf{X} & \mathbf{0} \end{pmatrix}$ , where  $\mathbf{X} = \begin{pmatrix} M_2 & \frac{1}{2} \sqrt{2} g v_u \\ \frac{1}{2} \sqrt{2} g v_d & \mu \end{pmatrix}$ . The La-

grangian for the chargino mass terms is:

$$\mathcal{L} = -\frac{1}{2} (\psi^\pm)^T M_{\tilde{C}} \psi^\pm + \text{c.c.} \tag{4.51}$$

The four neutralino states,  $\tilde{\chi}_1^0, \tilde{\chi}_2^0, \tilde{\chi}_3^0$  and  $\tilde{\chi}_4^0$ , have an interaction basis consisting of  $\tilde{N}_{\text{int}} = (\tilde{B}, \tilde{W}, \tilde{H}_d, \tilde{H}_u)^T$  and a mass mixing matrix given by

$$M^N = \begin{pmatrix} M_1 & 0 & -\frac{1}{2}g'v_d & \frac{1}{2}g'v_u \\ 0 & M_2 & \frac{1}{2}gv_d & -\frac{1}{2}gv_u \\ -\frac{1}{2}g'v_d & \frac{1}{2}gv_d & 0 & -\mu \\ \frac{1}{2}g'v_u & -\frac{1}{2}gv_u & -\mu & 0 \end{pmatrix}. \quad (4.52)$$

## 4.7 R-parity

As it stands thus far some of the renormalizable couplings of the MSSM may violate both baryon number and lepton number: the last term of Eq. (4.47) is baryon violating, while the three terms preceding it are lepton violating. Problematically, this leads to the proton decaying within a very short time frame, which is a scenario that obviously contradicts reality as we know it. In order to correct this undesirable scenario, a quantity known as R-parity may be defined as

$$P = (-1)^{3(B-L)+2s}, \quad (4.53)$$

where  $B$ ,  $L$  and  $s$  are baryon number, lepton number and spin respectively. The conservation of R-parity not only ensures the stability of the proton, but also baryon and lepton conservation. R-parity even (+1) particles are those that belong to the existing standard model, whereas their supersymmetric partners (sparticles) are R-parity odd (-1). This type of symmetry is known as a discrete  $Z_2$  symmetry. In the absence of R-parity violating terms, the new MSSM superpotential is:

$$W_{\text{MSSM}} = y_U^{ij} Q_i u_j^c H_u + y_D^{ij} Q_i d_j^c H_d + y_l^{ij} L_i l_j^c H_d + \mu H_u H_d. \quad (4.54)$$

As a consequence of R-parity conservation, every interaction vertex in the theory *must* contain an even number of sparticles. This means that sparticles are produced in pairs from SM particles, resulting in a distinct signature that may be detected at colliders. Notably, the R-parity constraint prevents the lightest supersymmetric particle (LSP) from

decaying into SM particles, as such a decay would have only one sparticle contribution to the interaction vertex, which is forbidden. This long-term stability is a highly desirable feature in a dark matter candidate, which is why LSPs have been the focus of many dark matter hypotheses using supersymmetric models with R-parity conservation applied. Furthermore, if a sparticle heavier than the LSP decays, it must produce an odd number of sparticles.

Imposing R-parity conservation on the MSSM and other supersymmetric models seems somewhat *ad hoc*, but it can be rationalised by formulating B-L as a continuous gauge symmetry, with R-parity conservation coming about as a result of the spontaneous breaking of this symmetry at very high energies by scalar VEVs with integer values of  $(B - L) + 2s$ .

---

# The NMSSM

---

*Note: This chapter describes work undertaken in 2011-early 2012, which was published in Physics Review D [83]. It may no longer be representative of the current status of the NMSSM.*

The previous chapter was devoted to discussing how supersymmetric models have become popular within the past few decades, particularly the MSSM. In these scenarios, dark matter takes the form of the LSP (usually a neutralino), which is favoured as a dark matter candidate for its stable and weakly-interacting nature [1].

As also discussed, various authors in the past decades have used the MSSM and its variants to make predictions about the interaction of dark matter as a neutralino with baryonic matter via the calculation of spin independent scattering cross sections. However, in the light of recent results from the LHC, the MSSM is becoming increasingly hard-pressed to serve as a complete description of physics beyond the standard model, because of the need to fine-tune its parameter space. The next-to-minimal supersymmetric standard model (NMSSM), on the other hand, is under less threat [84], and is currently a model of considerable interest.

In this chapter, original work involving a calculation the spin-independent cross section for neutralino-nucleon scattering within the constrained NMSSM will be presented, taking into account the constraints from the initial running of the LHC, as well as lattice QCD determinations of the light quark sigma commutators. The spin-independent cross section will be shown to possibly take a wide range of values depending on the composition of the lightest neutralino, being particularly small in the singlino-like case. However, applying the latest relic density constraints from WMAP results in a drastic reduction of regions in the NMSSM parameter space for which neutralino dark matter is viable.

## 5.1 The NMSSM

For a comprehensive review of the NMSSM, the review [85] is recommended.

As already discussed in the previous chapter, the MSSM introduces two neutral Higgs doublets  $H_u$  and  $H_d$  to the standard model. The Higgs superfields contribute a Higgs mass term to the superpotential of the MSSM,

$$W_{MSSM} = W_Y + \mu H_u H_d, \quad (5.1)$$

where  $W_Y$  represents the superpotential terms giving rise to the Yukawa couplings for the SM fermions and  $H_u, H_d$  are the Higgs chiral superfields. In order to avoid extreme fine-tuning, it is necessary that the  $\mu$  term and the scale of SUSY breaking both lie at the electroweak scale, 246 GeV, for various phenomenological reasons.

Firstly,  $\mu = 0$  is ruled out by experimental constraints, since no charginos have yet been detected and thus chargino masses are constrained to be greater than  $\approx 103$  GeV, which in turns constraints  $|\mu| > 100$  GeV (as determined by the chargino mass matrix). Furthermore, an undesirable massless axion would be created by  $\mu = 0$ .

On the flipside,  $\mu$  also appears in the Higgs squared mass terms in the Lagrangian:

$$\mathcal{L}_{\text{SUSY Higgs mass}} = |\mu|^2 (|H_u^0|^2 + |H_d^0|^2 + |H_u^+|^2 + |H_d^+|^2). \quad (5.2)$$

Since this equation is unstable at  $H_u^0 = H_d^0 = 0$  and is non-negative, this means that there must also be a negative soft SUSY breaking term included. In order to get the correct Higgs VEV, the squared Higgs mass terms cannot have greater magnitudes than and dominate over the negative squared mass terms of the introduced soft SUSY breaking. The consequence of this is that  $|\mu|$  is constrained to be  $\approx M_{\text{SUSY}}$ , which when  $M_{\text{SUSY}} \ll M_{\text{Planck}}$  prevents  $|\mu|$  itself from being too large. However, it is unknown why  $\mu \approx M_{\text{SUSY}}$  when  $\mu$  itself has little to do with SUSY breaking; this is generally considered to be a problem of naturalness. Historically, the NMSSM was formulated as a convenient way of dealing with this “ $\mu$  problem.” In the NMSSM,  $\mu$  is replaced by a gauge singlet chiral superfield  $S$ . An effective  $\mu$  can thus be dynamically generated upon SUSY breaking, explaining the coincidence of scales.

We also include an additional trilinear singlet field term. This is because the superpotential now has a  $U(1)'$  symmetry known as the Peccei-Quinn symmetry. Upon being broken by EWSB, a massless goldstone boson (pseudoscalar Higgs) known as an axion is produced, which is undesirable. In order to explicitly break this PQ symmetry beforehand, the term  $\frac{1}{3}\kappa S^3$  is introduced, which generates additional mass terms and results in an expanded superpotential in the NMSSM,

$$W_{NMSSM} = W_Y + \lambda S H_u H_d + \frac{\kappa}{3} S^3. \quad (5.3)$$

Here,  $\lambda$  and  $\kappa$  are dimensionless parameters. In some scenarios (covered in studies of the NMSSM under gauge mediated supersymmetry breaking, GMSB), an additional  $\xi_F S + \frac{1}{2}\mu' S^2$  is included alongside the usual cubic, where  $\mu'$  is another supersymmetric mass term and  $\xi_F$  parametrises a tadpole term. However, these  $Z_3$  symmetry-violating terms<sup>1</sup> are more frequently set to zero to preserve  $Z_3$  symmetry. The promotion of  $\mu$  to a singlet field does have some consequences for the neutralino-hadron cross section, since it results in a greater number of ways in which these particles can interact. Two extra Higgs fields are generated, such that the Higgs sector of the NMSSM consists of three neutral CP-even Higgs, two CP-odd Higgs and two charged Higgs. However, only the three CP-even Higgs are of relevance when formulating neutralino-hadron spin-independent cross sections. The two additional Higgs states stem from the scalar degrees of freedom given by the complex scalar field  $S$ , which also yields an additional fermion state: the neutral singlino  $\tilde{S}$  (superpartner of the singlet). The lightest neutralino is thus a mixing of five neutral fields rather than the four of the MSSM,

$$\tilde{\chi} = Z(N)_{11}\tilde{B} + Z(N)_{12}\tilde{W} + Z(N)_{13}\tilde{H}_d + Z(N)_{14}\tilde{H}_u + Z(N)_{15}\tilde{S}, \quad (5.4)$$

---

<sup>1</sup>Under the  $Z_3$  symmetry, superfields are invariant under the phase transformation  $\phi_i \rightarrow e^{i\frac{2\pi}{3}}\phi_i$ , where  $i$  denotes all the superfields in the model's superpotential.

with a mass mixing matrix given by

$$\mathcal{M} = \begin{pmatrix} M_1 & 0 & -m_Z c_\beta s_W & m_Z s_\beta s_W & 0 \\ 0 & M_2 & m_Z c_\beta c_W & -m_Z s_\beta c_W & 0 \\ -m_Z c_\beta s_W & m_Z c_\beta c_W & 0 & -\mu & -\mu_\lambda s_\beta \\ m_Z c_\beta s_W & -m_Z s_\beta c_W & -\mu & 0 & -\mu_\lambda c_\beta \\ 0 & 0 & -\mu_\lambda s_\beta & -\mu_\lambda c_\beta & \mu_\kappa \end{pmatrix}. \quad (5.5)$$

As before,  $\tilde{B}$  is the bino (superpartner of the  $U(1)$  gauge field),  $\tilde{W}$  is the wino (superpartner of the  $W$  gauge field), and  $\tilde{H}_d$  and  $\tilde{H}_u$  are Higgsinos (superpartners of the Higgs fields). In the mass mixing matrix,  $\tan\beta$  is the ratio of the VEVs of the original two neutral Higgs doublet fields ( $v_u/v_d$ ),  $s_\beta = \sin\beta$ ,  $c_\beta = \cos\beta$  and  $s_W$ ,  $c_W$  and  $t_W$  are the sine, cosine and tangent of  $\theta_W$  (the electroweak mixing angle).

The behaviour of the neutralino as it interacts with hadronic matter is strongly dependent on its exact composition. A predominantly bino-like neutralino (99% bino), for instance, will be shown to yield a high spin-independent cross section, relative to a singlino-like neutralino.

## 5.2 Spin-independent neutralino-hadron cross section

The calculation of the elastic scattering cross section between neutralinos and hadrons is of vital importance, since it determines the rate at which the particle may be detected in detection experiments (both directly and indirectly, since a higher cross section also leads to greater rates of neutralino annihilation in the galactic halo, thus increasing the resultant signal for indirect detection experiments). However, the details of this calculation are heavily model dependent.

Most basically, the scattering cross section between particles 1 and 2 is the effective area of collision, and defined by the total number of scattering events divided by the number densities ( $\rho_1$  and  $\rho_2$ ) and lengths ( $l_1$  and  $l_2$ ) of the bunches of particles as well as

the cross sectional area of scattering  $A$ :

$$\sigma = \frac{\text{Number of scattering events}}{\rho_1 \rho_2 l_1 l_2 A} \text{cm}^2. \quad (5.6)$$

The calculation of this cross section is in practice quite complicated, but can be simplified with a number of tricks. Before proceeding to the results for this section, it will be helpful to outline the method behind obtaining an expression for the spin-independent cross section  $\sigma_{SI}$  in the NMSSM.

The non-relativistic Lagrangian for the four-fermion interaction is

$$\mathcal{L} = \alpha_{2q} (\tilde{\chi} \gamma^\mu \gamma_5 \tilde{\chi}) (\bar{q} \gamma_\mu \gamma_5 q) + \alpha_{3q} (\tilde{\chi} \tilde{\chi}) (\bar{q} q), \quad (5.7)$$

where the first term is the spin-dependent component (consisting of t-channel  $Z$  exchange and s-channel squark exchange) and the second term is the SI component (consisting of t-channel Higgs exchange and s-channel squark exchange). It is this second half that we shall be focusing on, since the SI-component overwhelmingly dominates over the SD-component in most direct-detection experiments. The alpha coefficients,  $\alpha_{2q}$  and  $\alpha_{3q}$ , each encapsulate the relevant physics in terms of the amplitudes of each contributing neutralino-quark interaction (the top half of Fig. 5.1).

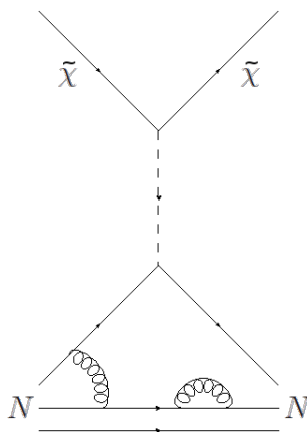


**Figure 5.1:** A neutralino-nucleon collision via Higgs exchange.

Fig. 5.1 shows one example of an interaction between a neutralino (denoted by  $\tilde{\chi}$ ) and a nucleon (neutralinos and nucleons may also interact via squark exchange). The cross section for this kind of interaction involves matrix elements of the form  $\langle N | \bar{q} q | N \rangle$ , where

$\langle N|$  represents the nucleon. The following gives a succinct expression for the contribution to  $\sigma_{SI}$  of each quark [86, 87],

$$\begin{aligned}\langle N\tilde{\chi}|\alpha_{3q}\tilde{\chi}\tilde{\chi}\bar{q}q|\tilde{\chi}N\rangle &= \alpha_{3q}\langle N|\bar{q}q|N\rangle \\ &= \alpha_{3q}m_N\frac{f_{Tq}}{m_q},\end{aligned}\quad (5.8)$$

where  $m_N$  is the nucleon mass ( $N = p$  or  $n$ ) and  $f_{Tq}$  is defined by the relation  $m_N f_{Tq} \equiv \langle N|m_q\bar{q}q|N\rangle$ . Summing over light and heavy quarks results in a generic expression for the cross section:

$$\sigma_{SI} = \frac{4m_r^2}{\pi} (Zf_p + (A - Z)f_n)^2, \quad (5.9)$$

where  $m_r$  is the neutralino-nucleon reduced mass and the  $f$  terms are found by summing over light and heavy quark contributions ( $m_q$  and  $m_Q$  being the masses of the light and heavy quarks respectively):

$$\frac{f}{m_N} = \sum_{q=u,d,s} \frac{\alpha_{3q}f_{Tq}}{m_q} + \sum_{Q=c,b,t} \frac{\alpha_{3Q}f_{TQ}}{m_Q}. \quad (5.10)$$

This may be simplified further by noting that  $m_N = \langle N|\theta_\mu^\mu|N\rangle$  for a system at rest, where the trace of the energy-momentum tensor is given by

$$\theta_\mu^\mu = \sum_q m_q\bar{q}q + \sum_Q m_Q\bar{Q}Q - \frac{7\alpha_s}{8\pi}G_{\mu\nu}^\alpha G^{\alpha\mu\nu}. \quad (5.11)$$

Taking the system to be at zero-momentum, such that  $\theta_\mu^\mu = \theta_0^0$ , this equation becomes

$$\begin{aligned}m_N &= \langle N|\sum_q m_q\bar{q}q|N\rangle + \langle N|\sum_Q m_Q\bar{Q}Q|N\rangle \\ &\quad - \langle N|\frac{7\alpha_s}{8\pi}G_{\mu\nu}^\alpha G^{\alpha\mu\nu}|N\rangle.\end{aligned}\quad (5.12)$$

The extra term involving the quark-gluon coupling constant  $\alpha_s$  and the gluon field strength tensor  $G_{\mu\nu}^\alpha$  ( $\alpha = 1, \dots, 8$ ) can be conveniently eliminated by appealing to the Novikov-Shifman-Vainshtein [88] relation, which tells us that  $-(7\alpha_s/8\pi)\langle N|G_{\mu\nu}^\alpha G^{\alpha\mu\nu}|N\rangle$  may be

written as  $(7/2) \sum_Q m_Q \langle N | \bar{Q}Q | N \rangle$ ,

$$\begin{aligned} m_N &= \sum_q \langle N | \bar{q}q | N \rangle + \frac{9}{2} \sum_Q m_Q \langle N | \bar{Q}Q | N \rangle \\ &= \sum_q m_N f_{Tq} + \frac{27}{2} m_Q \langle N | \bar{Q}Q | N \rangle, \end{aligned} \quad (5.13)$$

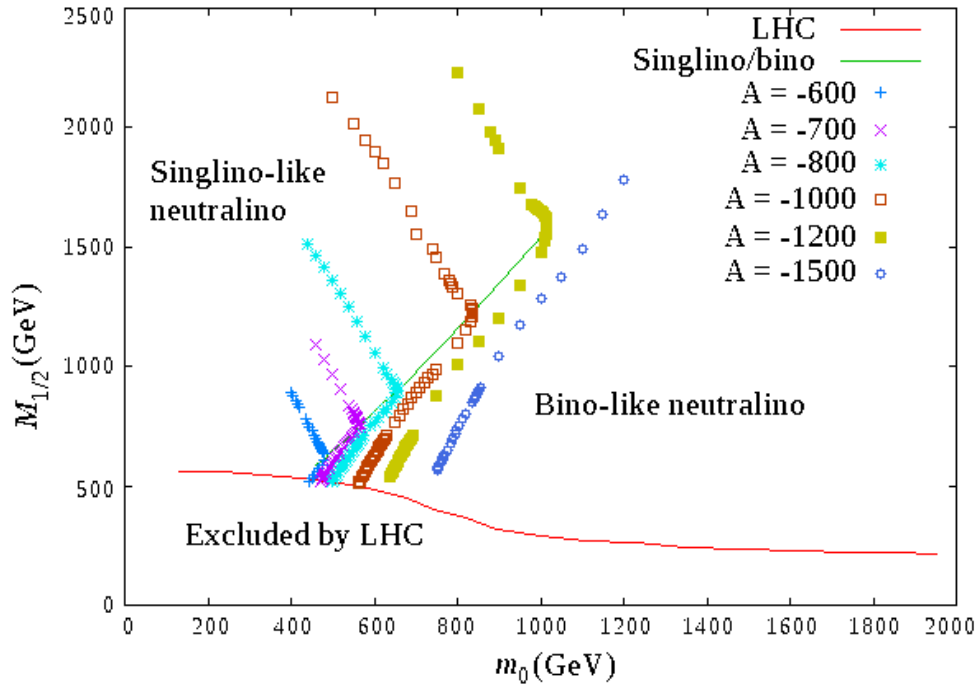
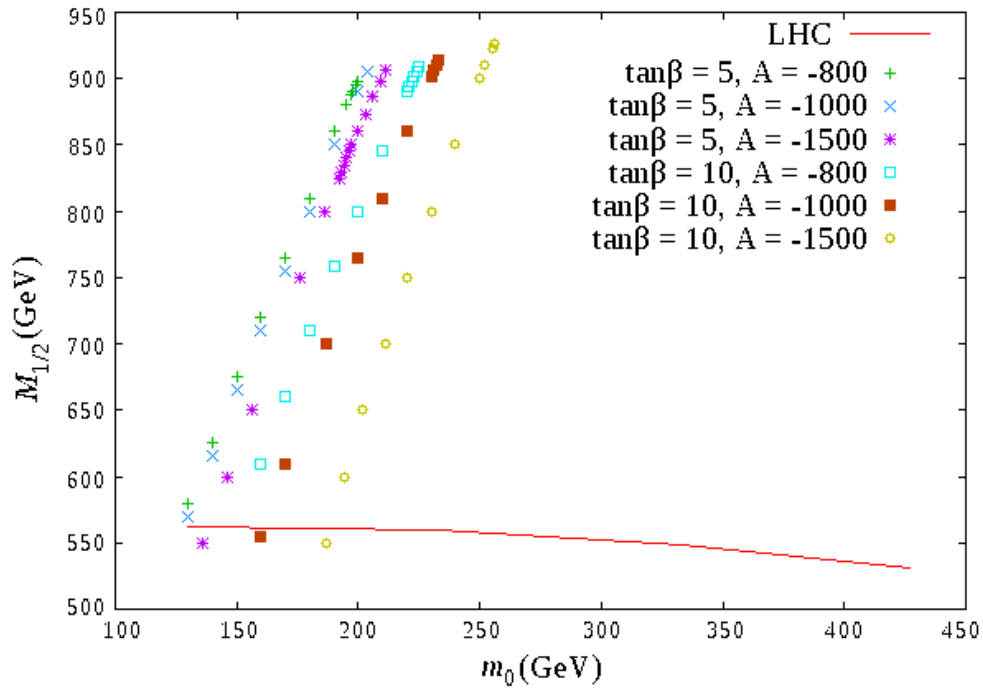
and thus  $m_Q \langle N | \bar{Q}Q | N \rangle = \frac{2}{27} m_N \left( 1 - \sum_q f_{Tq} \right)$ . Hence, the final expression for  $f$  is

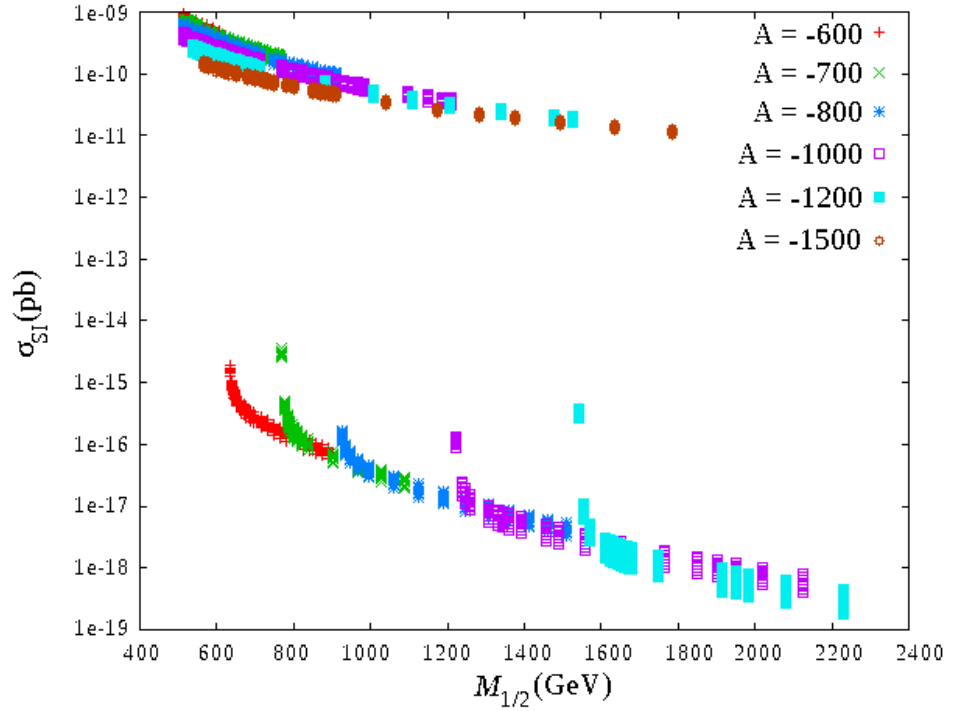
$$\begin{aligned} \frac{f}{m_N} &= \sum_{q=u,d,s} \frac{\alpha_{3q} f_{Tq}}{m_q} + \frac{2}{27} f_{TQ} \sum_{Q=c,b,t} \frac{\alpha_{3Q}}{m_Q}, \\ f_{TQ} &= \left( 1 - \sum_{q=u,d,s} f_{Tq} \right). \end{aligned} \quad (5.14)$$

The  $\alpha_{3q}$  terms for the NMSSM are derived by computing the amplitudes of the contributing Feynman diagrams. This is done so at zero-momentum scale, because the usual scenarios involve dark matter-hadron collisions at low speeds. In addition, the  $f_{Tq}$  terms have been derived from numerous studies in lattice QCD [89–91], which are updates of early estimates [92, 93].

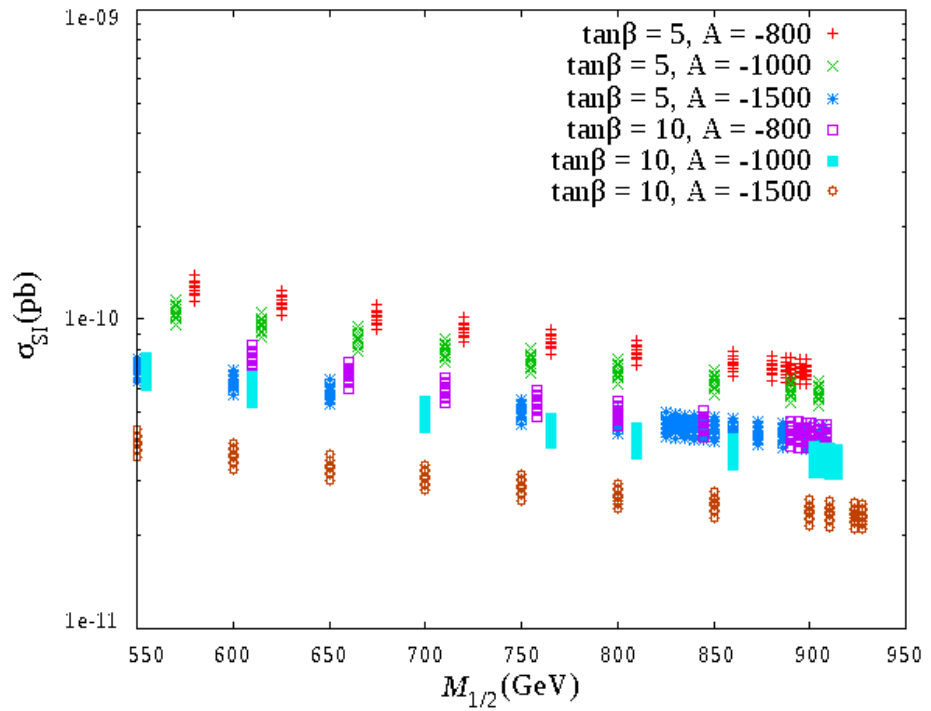
### 5.3 Results and Discussion

In order to compute the  $\alpha_{3q}$  terms and  $\sigma_{SI}$  using the latest results for the sigma terms from lattice QCD, we utilised micrOMEGAs, a code for calculating general dark matter properties under supersymmetric physics, by Belanger *et al.* [94]. In order to reduce the parameter space, we chose a constrained version of the NMSSM in which the scalar and gaugino masses were taken to be universal at the GUT scale. Thus, the free parameters were the universal scalar mass  $m_0$ , universal gaugino mass  $M_{1/2}$ , singlino trilinear coupling  $A_\kappa$ , Higgs-singlino trilinear coupling  $A_0$  (later referred to simply as  $A$  in this chapter),  $\tan\beta$  (the ratio of vacuum expectation values of the neutral Higgses) and  $\lambda$ . In addition, the effective Higgs mass  $\mu$  was taken to be positive. One of the constraints imposed by micrOMEGAs (namely, the computation of the muon anomalous moment [95]) was relaxed. Initially, the light-quark sigma term  $\sigma_l$  was taken to be 47 MeV, to correspond with a lattice determination of  $\sigma_l = 47 \pm 9$  MeV, and the strangeness sigma term  $\sigma_s$  was taken to be 50 MeV, in accordance with  $\sigma_s = 50 \pm 8$  MeV from [89], which was obtained

(a)  $\tan\beta = 50$ ,  $\lambda = 0.01$ ,  $A_\kappa = -40$ (b)  $\tan\beta = 5$  or  $10$ ,  $\lambda = 0.1$ ,  $A_\kappa = -40$ **Figure 5.2:** Regions in the space of universal spin-1/2 and spin-0 masses allowed by relic density constraints.



(a)  $\tan\beta = 50$ ,  $\sigma_s = 22 \pm 6$ ,  $\sigma_l = 47 \pm 9$



(b)  $\tan\beta = 5$  or  $10$ ,  $\sigma_s = 22 \pm 6$ ,  $\sigma_l = 47 \pm 9$

**Figure 5.3:** Cross sections for the spin-independent neutralino-neutron cross section for the parameter sets illustrated in Fig. 5.2(a) and Fig. 5.2(b).

by averaging two different lattice results. However, recent findings tend to favour an even lower value [96]. Thus, these scans were repeated with  $\sigma_s = 22 \pm 6$  and  $\sigma_l = 47 \pm 9$ , and the plots provided used these values. In addition, findings from WMAP and other observations have placed constraints on the relic density  $\Omega$  to lie between 0.1053 and 0.1193 at 95% confidence level [97, 98]. This constraint places tight restrictions on the allowed parameter space, where for a fixed  $A$ , the allowed regions are reduced to thin strips or lines in the  $(m_0, M_{1/2})$  plane. Finally, recent data from the CMS collaboration [99] was used to place a lower bound on  $(m_0, M_{1/2})$ ; although this bound was originally formulated within the context of the MSSM, the spectrum of superpartners is quite similar in the NMSSM within this region of parameter space, so the bound still represents a very good approximation in the present case.

Sweeps of  $m_0$  and  $M_{1/2}$  were carried out for various values of  $A$  at high  $\tan\beta$  (50), with  $\lambda$  and  $A_\kappa$  fixed at 0.01 and -40 respectively. Points that are allowed by both LHC and relic density constraints are plotted in Figure 5.2(a). Noticeably, as  $M_{1/2}$  is increased the character of the neutralino changes quite significantly. For lower  $M_{1/2}$  along each strip, the content is predominantly bino, and cross sections are of the order of  $10^{-9}$  pb. However, as the points cross the bino-singlino line, as illustrated in Figure 5.2(a), the neutralino is almost entirely singlino and the cross section drops by many orders of magnitude. For this reason, the region immediately to the right of the bino-singlino line is most favourable as an area of interest, since neutralinos in the singlino-like region have interaction cross sections that are far too small to allow for detection in current searches (see Figure 5.3(a)).

In addition, lower values of  $\tan\beta$  (5 and 10) also yield allowed regions, although the highest cross sections are found for  $\tan\beta = 50$  (see Figure 5.3(b)). However, in this region of scanned  $A$  values we do not observe any singlino-like behaviour (as evidenced in Figure 5.2(b)), since a limit is quickly reached beyond which the LSP is no longer a neutralino. Very low values of  $\tan\beta$  proved to be unfavourable, because of the presence of a Landau pole.

Table 5.1 shows that in the NMSSM at high  $\tan\beta$ , the cross section is dominated by the down-type quarks (particularly the bottom and strange quarks). This is similar to the finding in the CMSSM, although in the present case the bottom quark dominates by an even greater percentage. This is shown also for Table 5.1 with an updated  $\sigma_s$  value.

It is interesting to compare these results to those obtained for the constrained minimal supersymmetric standard model (CMSSM) in [89]; it seems that cross sections are on average lower (typically by an approximate factor of 2) in the constrained NMSSM than in the CMSSM.

**Table 5.1:** Example breakdown of quark flavour contributions at a high cross section with  $\sigma_s = 22$ ,  $\sigma_l = 47$ .

Model	$q$	$\alpha_{3q}/m_q$	$f_q^p/f_p$
$\tan\beta = 50, A = -575$	$u$	$-1.179 \times 10^{-9}$	0.0196
$m_0 = 436, M_{1/2} = 510$	$d$	$-1.090 \times 10^{-8}$	0.1820
$\lambda = 0.01, A_\kappa = -40$	$c$	$-1.179 \times 10^{-9}$	0.0538
$\sigma_{SI} = 8.678 \times 10^{-10}$ pb	$s$	$-1.090 \times 10^{-8}$	0.1700
$\sigma_l = 47$	$t$	$-1.174 \times 10^{-9}$	0.0536
$\sigma_s = 22$	$b$	$-1.142 \times 10^{-8}$	0.5213

From these results, it seems that the constrained NMSSM may still plausibly produce a viable candidate for dark matter in the form of its lightest neutralino. However, the parameter space must be quite finely tuned in order to produce regions in which this may occur because of the precision of the WMAP results. As expected,  $\sigma_{SI}$  for the neutralino-hadron collision in this scheme is very strongly dependent on the composition of the neutralino itself, being negligibly small for singlino-like neutralinos. Furthermore, given the sharp drop in the  $\sigma_{SI}$  for a singlino-like neutralino, these results give a clear indication of a possible scenario where a discovery at the LHC is compatible with a null result in direct detection dark matter searches.

More scans will be necessary for other variations of supersymmetric models as new data from the LHC is produced. The following chapters will move on to a more extended model of supersymmetry, the E6SSM, and present more original work and its implications for the detection of neutralino dark matter in direct detection experiments.



---

# The $E_6$ SSM

---

As already outlined in previous chapters, the outstanding problem of dark matter has motivated many proposed modifications to the standard model. Supersymmetric extensions in particular, although suggested for many other reasons, are also often favoured for providing viable, weakly interacting massive particle (WIMP) candidates for dark matter. For instance, the application of R-parity, a  $Z_2$  symmetry meant to preserve baryon and lepton number, to the MSSM ensures the stability of the lightest supersymmetric particle, a neutralino. However, these supersymmetric models are not without potential shortcomings of their own. To a certain extent,  $E_6$ -inspired supersymmetric models of physics have their roots in a desire to find a solution to the persistent  $\mu$  problem of the MSSM, whilst further eliminating the potential drawbacks that may be found in the solutions postulated by other models. The  $\mu$  problem, where  $\mu$  is a parameter with dimensions of mass that appears as a coupling between Higgs fields in the term  $\mu H_d H_u$  in the superpotential of the MSSM, is fundamentally one of naturalness, since in order for the Higgs doublets to gain non-zero VEVs,  $\mu$  must be of the same order of magnitude as the electroweak scale. Unfortunately, a physical connection between  $\mu$  and the EW scale is not apparent in the MSSM, meaning that adjusting  $\mu$  to match the latter is decidedly *ad hoc*.

As already explained, the NMSSM attempts to rectify the unnaturalness of this situation via the addition of a singlet field  $S$  to the superpotential which couples to the Higgs doublets:

$$W_{\text{NMSSM}} = W_{\text{MSSM}} + W_{\text{Yukawa}} + \lambda S H_d H_u + \frac{\kappa}{3} S^3. \quad (6.1)$$

The trilinear term  $\frac{\kappa}{3} S^3$  is necessary to prevent an additional Peccei-Quinn symmetry that would otherwise introduce an unwanted axion.  $\mu$  is subsequently generated dynamically by the vacuum expectation value of a singlet field,  $\mu_{\text{eff}} = \frac{s\lambda}{\sqrt{2}}$ , ensuring that it is of the same

order as the SUSY breaking scale in a “natural” way. However, a potentially unpleasant feature of the NMSSM is that it can also give rise to cosmological domain walls. These domain walls, formed in the early universe as the result of the breaking of  $Z_3$  symmetry, have a high surface energy density and fundamentally alter the evolution of the cosmos in a manner that contradicts our observations of its degree of homogeneity and isotropy [100]. The presence of this problem has prompted the refinement of the NMSSM in numerous ways [101], and also partly motivates the  $E_6$ SSM [102].

The  $E_6$ SSM features an extended particle content to include three fundamental  $27_i$  representations (where  $i$  runs from 1 to 3), which ensures generation-by-generation anomaly cancellation [103]. This model and its variants have been comprehensively studied in recent years [104–109] for its neutralino content and additional exotic coloured states. In our own study, we explore a constrained version of the  $E_6$ SSM with additional symmetries (EZSSM). Ultimately, our aim is to explore the parameter space in greater detail and in particular to find regions that not only yield high spin-independent cross sections between dark matter neutralinos and nucleons, but are still viable in the light of the 2012 discovery of the Higgs Boson and relic density constraints from WMAP. In this chapter the features of the  $E_6$ SSM are further detailed, including the spectra of its associated neutralinos and charginos. This begins with a discussion of the key parameters and benchmarks to be explored in a region scan, as well as the computational tools necessary (discussed in the following chapter). This will finally lead to a presentation and discussion of original work, detailing the largest parameter exploration of the  $E_6$ SSM to date.

## 6.1 The $E_6$ SSM

The  $E_6$ SSM can be derived from a symmetry breaking chain of the  $E_6$  GUT group:

$$\begin{aligned}
 E_6 &\rightarrow SO(10) \otimes U(1)_\phi, \\
 SO(10) &\rightarrow SU(5) \otimes U(1)_X, \\
 SU(5) &\rightarrow SU(3) \otimes SU(2) \otimes U(1)_Y, \\
 \therefore E_6 &\rightarrow SU(3) \otimes SU(2) \otimes U(1)_Y \otimes U(1)_N,
 \end{aligned} \tag{6.2}$$

where  $U(1)_N$  is a linear combination of  $U(1)_\chi$  and  $U(1)_\phi$ :

$$U(1)_N = U(1)_\chi \cos\theta + U(1)_\phi \sin\theta. \quad (6.3)$$

In Eq. (6.3),  $\tan\theta$  may be set to equal  $\sqrt{15}$  ( $\cos\theta = \frac{1}{4}$ , and  $\sin\theta = \frac{\sqrt{15}}{4}$ ) in order to ensure that sterile (right-handed) neutrinos carry zero charges and don't participate in the gauge interactions [110] (these gain masses after the breaking of  $E_6$  at an intermediate scale [105]).

The three  $27_i$  families mentioned in the introduction to this chapter decompose under the  $SU(5) \otimes U(1)_N$  subgroup in the  $E_6$  as:

$$27_i \rightarrow (10, 1)_i + (5^*, 2)_i + (5^*, -3)_i + (5, -2)_i + (1, 5)_i + (1, 0)_i, \quad (6.4)$$

with  $i = 1, 2, 3$ . The first quantity in each bracket in Eq. 6.4 is the  $SU(5)$  representation and the second quantity is the extra  $U(1)_N$  charge (the decomposition occurs under a  $SU(5) \times U(1)_N$  subgroup of  $E_6$ ). The first two terms contains quarks and leptons, the third and fourth terms contain up- and down-type Higgs doublets  $H_{ui}$  and  $H_{di}$  as well as additional exotic coloured states  $D_i$  and  $\bar{D}_i$ , the fifth contains the SM-singlet fields  $S_i$  and the last contains the sterile neutrinos. Furthermore, an additional  $27'$  and  $\bar{27}'$  provide  $SU(2)_W$  doublet  $H'$  and anti-doublet  $\bar{H}'$  states, respectively. The latter are included in order to ensure that gauge coupling unification is preserved.

Ultimately, the superpotential of  $E_6$ SSM leads to a term analogous to that of the NMSSM, where each  $i, j, k$  runs from 1 to 3 to represent the three generations:

$$\sum_{ijk} \lambda_{ijk} S_i H_{dj} H_{uk} \in W_{E_6SSM}. \quad (6.5)$$

In this scenario, the effective  $\mu$  parameter is provided by  $\mu_{eff} = \frac{s\lambda_{333}}{\sqrt{2}}$ . This is an example of a  $U(1)$  extension of the NMSSM - no trilinear  $S^3$  is required (indeed, such a term is forbidden by the  $U(1)$  gauge symmetries that emerge in the breaking of the  $E_6$  group), as the Peccei-Quinn axion is absorbed by the new gauge boson that breaks each  $U(1)$ .

### 6.1.1 $Z_2$ symmetries and the EZSSM

The full superpotential of the  $E_6$ SSM is given by:

$$W_{E_6SSM} = W_0 + W_1 + W_2, \quad (6.6)$$

where

$$\begin{aligned} W_0 = & \lambda_{ijk} S_i H_{dj} H_{uk} + \kappa_{ijk} S_i D_j \hat{D}_k + h_{ijk}^N \hat{N}_i^c H_{uj} L_k \\ & + h_{ijk}^U \hat{u}_i^c H_{uj} Q_k + h_{ijk}^D \hat{d}_i^c H_{dj} Q_k + h_{ijk}^E \hat{e}_i^c H_{dj} L_k, \end{aligned} \quad (6.7)$$

$$W_1 = g_{ijk}^Q D_i Q_j Q_k + g_{ijk}^q \hat{D}_i \hat{d}_j^c \hat{u}_k^c, \quad (6.8)$$

$$W_2 = g_{ijk}^N \hat{N}_i^c D_j \hat{d}_k^c + g_{ijk}^E \hat{e}_i^c D_j \hat{u}_k^c + g_{ijk}^D Q_i L_j \hat{D}_k. \quad (6.9)$$

Only the third generation singlets and Higgses will acquire vacuum expectation values, and by convention these are referred to as  $S_3 \equiv S$ ,  $H_{d3} \equiv H_d$  and  $H_{u3} \equiv H_u$  with VEVs  $s$ ,  $v_d$  and  $v_u$  respectively. The first and second generations are known as ‘‘inert’’ fields.

However, this picture is not complete without the application of  $Z_2$  symmetries, since at this point there are non-diagonal flavor transitions and lepton and baryon number violating operators that lead to rapid proton decay (an obviously undesirable feature of any model) are not forbidden.

One possibility, which is explored in detail in [108], is to impose an approximate  $Z_2^H$  symmetry, under which  $S_3$ ,  $H_{d3}$  and  $H_{u3}$  are even while every other field is odd. If any term in the superpotential that violates  $Z_2^H$  (by containing superfields adding up to a net odd value) is forbidden, the result is that couplings containing  $\lambda_{333}$ ,  $\lambda_{\alpha 33}$ ,  $\lambda_{3\alpha 3}$ ,  $\lambda_{33\alpha}$  or  $\lambda_{\alpha\beta\gamma}$  ( $\alpha, \beta, \gamma \in 1, 2$ ) are suppressed. However, the  $Z_2^H$  symmetry cannot be exact, since it forbids all terms that would otherwise allow for the decay of exotic quarks. An additional  $Z_2$  symmetry must thus be applied to act the part of R-parity and ensure baryon and lepton number conservation, such as  $Z_2^L$  (in which the exotic quarks are diquarks) or  $Z_2^B$  (in which the exotic quarks are leptoquarks).

There are numerous other  $Z_2$  symmetries that may be applied. The choice of which symmetry-violating terms to include has an impact on the particle spectra generated from parameter space, which may under certain circumstances be in tension with observed

experimental constraints. One can stipulate that only the two inert singlets  $S_\alpha$  are odd. This is known as the  $Z_2^S$  symmetry (and it is exact). When this is imposed, the  $E_6$ SSM model is known as the EZSSM and the couplings containing  $\lambda_{\alpha jk}$  alone are suppressed. This is beneficial for neutralino dark matter detection, since the decoupled inert singlinos contribute to the effective number of neutrinos rather than dark matter relic density (light dark matter with inert singlinos are ruled out by direct detection limits).

### 6.1.2 Squarks, sleptons, gluinos and Higgsinos

As before, in the NMSSM chapter, each quark and lepton state of the SM has a superpartner. The squared masses of first and second generation squarks and sleptons are determined by the approximate diagonal entries of their  $6 \times 6$  mass matrices, given that their partner quarks and leptons have extremely small Yukawa couplings (leading to negligibly small mixing angles for first and generation squarks and sleptons). The expressions for the squark masses below are provided by [105]:

$$m_{dLi}^2 \approx m_{Q_i}^2 + \left(-\frac{1}{2} + \frac{1}{3}\sin^2\theta_W\right) M_Z^2 \cos 2\beta + \Delta_Q, \quad (6.10)$$

$$m_{uLi}^2 \approx m_{Q_i}^2 + \left(\frac{1}{2} - \frac{2}{3}\sin^2\theta_W\right) M_Z^2 \cos 2\beta + \Delta_Q, \quad (6.11)$$

$$m_{uRi}^2 \approx m_{u_i^c}^2 + \frac{2}{3}M_Z^2 \sin^2\theta_W \cos 2\beta + \Delta_{u^c}, \quad (6.12)$$

$$m_{dRi}^2 \approx m_{d_i^c}^2 - \frac{1}{3}M_Z^2 \sin^2\theta_W \cos 2\beta + \Delta_{d^c}, \quad (6.13)$$

$$m_{eLi}^2 \approx m_{L_i}^2 + \left(-\frac{1}{2} + \sin^2\theta_W\right) M_Z^2 \cos 2\beta + \Delta_L, \quad (6.14)$$

$$m_{eRi}^2 \approx m_{e_i^c}^2 - M_Z^2 \sin^2\theta_W \cos 2\beta + \Delta_{e^c}, \quad (6.15)$$

$$m_{\nu_i}^2 \approx m_{L_i}^2 + \frac{1}{2}M_Z^2 \cos 2\beta + \Delta_L, \quad (6.16)$$

where the  $\Delta$  terms (contributions from the  $U(1)_N$  D-term) are given by:

$$\Delta_\phi = \frac{g_1'^2}{2} (Q_d v_d^2 + Q_u v_u^2 + Q_s s^2) Q_\phi. \quad (6.17)$$

### 6.1.3 Neutralino and chargino mass mixing matrices

The presence of additional fields lends a certain richness to the content of the neutralino and chargino mass mixing matrices. In the full unconstrained  $E_6$ SSM, the lightest neutralino may have as many as twelve contributing fields in its interacting basis; if all  $Z_2^H$  violating couplings are neglected, however, this is reduced to six, since all interactions between third and first/second generation Higgsinos are suppressed:

$$\tilde{N}_{int} = \left( \begin{array}{cccc|cc} \tilde{B} & \tilde{W} & \tilde{H}_d^0 & \tilde{H}_u^0 & \tilde{S} & \tilde{B}' \end{array} \right)^T. \quad (6.18)$$

For the upcoming exploration of the EZSSM parameter space, these  $Z_2^H$  violating couplings were allowed and the exact  $Z_2^S$  symmetry was adhered to, resulting in a basis composed of ten fields ( $\tilde{S}_u$  and  $\tilde{S}_d$  are decoupled):

$$\tilde{N}_{int} = \left( \begin{array}{cccccc|cccc} \tilde{B} & \tilde{W}^3 & \tilde{H}_d^0 & \tilde{H}_u^0 & \tilde{S}_3 & \tilde{B}' & \tilde{H}_{d1}^0 & \tilde{H}_{d2}^0 & \tilde{H}_{u1}^0 & \tilde{H}_{u2}^0 \end{array} \right)^T. \quad (6.19)$$

This leads to the following neutralino mass mixing matrix:

$$M^N = \left( \begin{array}{cccccc|cccc} M_1 & 0 & -\frac{1}{2}g'v_d & \frac{1}{2}g'v_u & 0 & 0 & 0 & 0 & 0 & 0 \\ 0 & M_2 & \frac{1}{2}g'v_d & -\frac{1}{2}g'v_u & 0 & 0 & 0 & 0 & 0 & 0 \\ -\frac{1}{2}g'v_d & \frac{1}{2}g'v_d & 0 & -\mu & -\frac{\lambda v_u}{\sqrt{2}} & Q_d g'_1 v_d & 0 & 0 & -\frac{\lambda_{331}s}{\sqrt{2}} & -\frac{\lambda_{332}s}{\sqrt{2}} \\ \frac{1}{2}g'v_u & -\frac{1}{2}g'v_u & -\mu & 0 & \frac{\lambda v_d}{\sqrt{2}} & Q_u g'_1 v_u & -\frac{\lambda_{313}s}{\sqrt{2}} & -\frac{\lambda_{323}s}{\sqrt{2}} & 0 & 0 \\ 0 & 0 & -\frac{\lambda v_u}{\sqrt{2}} & -\frac{\lambda v_d}{\sqrt{2}} & 0 & Q_s g'_1 s & -\frac{\lambda_{313}v_u}{\sqrt{2}} & -\frac{\lambda_{323}v_u}{\sqrt{2}} & -\frac{\lambda_{331}v_d}{\sqrt{2}} & -\frac{\lambda_{332}v_d}{\sqrt{2}} \\ 0 & 0 & Q_d g'_1 v_d & Q_u g'_1 v_u & Q_s g'_1 s & M'_1 & 0 & 0 & 0 & 0 \\ \hline 0 & 0 & 0 & -\frac{\lambda_{313}s}{\sqrt{2}} & -\frac{\lambda_{313}v_u}{\sqrt{2}} & 0 & 0 & 0 & -\frac{\lambda_{311}s}{\sqrt{2}} & -\frac{\lambda_{312}s}{\sqrt{2}} \\ 0 & 0 & 0 & -\frac{\lambda_{323}s}{\sqrt{2}} & -\frac{\lambda_{323}v_u}{\sqrt{2}} & 0 & 0 & 0 & -\frac{\lambda_{321}s}{\sqrt{2}} & -\frac{\lambda_{322}s}{\sqrt{2}} \\ 0 & 0 & -\frac{\lambda_{331}s}{\sqrt{2}} & 0 & -\frac{\lambda_{331}v_d}{\sqrt{2}} & 0 & -\frac{\lambda_{311}s}{\sqrt{2}} & -\frac{\lambda_{312}s}{\sqrt{2}} & 0 & 0 \\ 0 & 0 & -\frac{\lambda_{332}s}{\sqrt{2}} & 0 & -\frac{\lambda_{332}v_d}{\sqrt{2}} & 0 & -\frac{\lambda_{321}s}{\sqrt{2}} & -\frac{\lambda_{322}s}{\sqrt{2}} & 0 & 0 \end{array} \right), \quad (6.20)$$

where  $Q_d = -\frac{3}{\sqrt{40}}$ ,  $Q_u = -\frac{2}{\sqrt{40}}$  and  $Q_s = -\frac{5}{\sqrt{40}}$  are the  $U(1)_N$  charges of the down-type Higgs doublets, the up-type Higgs doublets and the SM-singlets respectively. Furthermore,  $M_1$ ,  $M_2$  and  $M'_1$  are soft gaugino masses, while  $g'_1$  is the GUT normalised  $U(1)_N$  gauge coupling. The top-left block of this matrix is the usual NMSSM neutralino mass mixing matrix with an additional row and column for the  $U(1)$  bino, known as the USSM sector. The rest are contributions from couplings with the inert Higgsinos. Note that if the  $Z_2^H$

symmetry were exact (by limiting  $\lambda_{3\alpha 3}$  and  $\lambda_{33\alpha}$  from above by imposing flavour changing neutral current (FCNC) constraints), the bottom right corner becomes an approximately decoupled mass matrix in a basis consisting of the inert Higgsinos.

For completion, the interaction basis of the chargino is:

$$\tilde{C}_{int} = \left( \begin{array}{cc|cc|cc|cc} \tilde{W}^+ & \tilde{H}_{u3}^+ & \tilde{H}_{u2}^+ & \tilde{H}_{u1}^+ & \tilde{W}^- & \tilde{H}_{d3}^- & \tilde{H}_{d2}^- & \tilde{H}_{d1}^- \end{array} \right)^T. \quad (6.21)$$

The chargino mass mixing matrix is:

$$M^C = \begin{pmatrix} 0 & P^T \\ P & 0 \end{pmatrix}, \quad (6.22)$$

where

$$P = \begin{pmatrix} M_2 & \sqrt{2}m_W s_\beta & 0 & 0 \\ \sqrt{2}m_W c_\beta & \mu & \frac{1}{\sqrt{2}}\lambda_{332}s & \frac{1}{\sqrt{2}}\lambda_{331}s \\ 0 & \frac{1}{\sqrt{2}}\lambda_{323}s & \frac{1}{2}\lambda_{322}s & \frac{1}{\sqrt{2}}\lambda_{321}s \\ 0 & \frac{1}{\sqrt{2}}\lambda_{313}s & \frac{1}{\sqrt{2}}\lambda_{312}s & \frac{1}{\sqrt{2}}\lambda_{311}s \end{pmatrix}. \quad (6.23)$$

#### 6.1.4 Neutralino dark matter and previous benchmarks

As before, the dark matter candidate under consideration is the lightest neutralino,  $\tilde{\chi}_1^0$ , which interacts with nucleons via spin-1  $Z$  exchange (spin-dependent), Higgs exchange (spin-independent) and squark exchange (both spin-dependent and spin-independent). It is not the lightest  $R$ -parity odd state, since there also exist massless inert singlinos  $\tilde{\sigma}$ . Despite this, it is still stable and thus viable as a dark matter candidate, since it cannot decay to  $\tilde{\sigma}$ : the potential  $\tilde{\chi}_1^0 \rightarrow \tilde{\sigma}\sigma$  decay has no kinematically viable final states with the same quantum numbers as the lightest neutralino [108].

The viability of the lightest neutralino as a dark matter candidate has been explored by numerous previous studies [111, 112]. These various studies have taken numerous different assumptions about the neutralino according to the  $E_6$ SSM model - for example, Athron

*et al.* [111] explore the neutralino in the context of the constrained  $E_6$ SSM (c $E_6$ SSM), in which case the inert Higgsinos and singlinos are decoupled from the neutralino mixing matrix, rendering it as a  $6 \times 6$  matrix with a basis of  $(\tilde{B}, \tilde{W}, \tilde{H}_d, \tilde{H}_u, \tilde{S}, \tilde{B}')$ .

The impact of the extended particle spectrum of the  $E_6$ SSM on cosmological evolution is an important area of consideration. Hall & King [108] worked with a  $10 \times 10$  neutralino mass matrix and unified soft parameters at the GUT scale (just as this thesis), demonstrating that bino-like neutralinos successfully fit the constraints on the properties of dark matter from WMAP. In this scenario, the presence of the two extra decoupled inert singlino states ( $\tilde{S}_1$  and  $\tilde{S}_2$ ) was considered in terms of how they potentially affect big bang nucleosynthesis. The primordial abundance of  ${}^4\text{He}$  depends on the baryon-to-photon ratio,  $\eta$ , and the effective number,  $N_{\text{eff}}$ , of neutrinos (and neutrino-like particles) contributing to the expansion of the early universe, being particularly sensitive to  $N_{\text{eff}}$ . Given the justifiable assumption that the inert singlino decoupling occurs within a temperature range defined between the decoupling of the strange quark mass and decoupling of the charm quark mass, the eventual derived result for  $N_{\text{eff}}$  in the  $E_6$ SSM was:

$$N_{\text{eff}} = 3 + 2 \left( \frac{43}{247} \right)^{4/3} \approx 3.194, \quad (6.24)$$

which is valid for a  $Z'$  mass between approximately 1.3 TeV and 4.7 TeV. This is in good agreement with Planck 2015 data,  $N_{\text{eff}} = 3.15 \pm 0.23$  [113], and lies slightly closer to its central value than the value predicted by the standard model,  $N_{\text{eff}} = 3.046$ . [114]. The  $N_{\text{eff}}$  values obtained by [108] for lower  $Z'$  masses are above 4, and thus lie well beyond the 95% confidence level of this Planck data. However, this is of little consequence, given that the latest LHC results have set new lower mass limits on  $Z'$ . CMS has set lower bounds of 3.15 TeV and 2.60 TeV for sequential standard model  $Z'$  and superstring-inspired  $U(1)_\psi$   $Z'$  bosons respectively [115], while ATLAS has set lower dilepton channel bounds of 3.40 TeV, 2.85 TeV and 2.79 TeV on  $Z'_{SSM}$ ,  $Z'_N$  (the  $Z'$  that is relevant to our  $E_6$ SSM model) and  $Z'_\psi$ , respectively, [116]. Thus,  $Z'$  masses lower than 1.3 TeV have themselves been ruled out.

The three benchmark points chosen in reference [108] illustrate the diversity of outcomes with a light neutralino dark matter candidate in this model, as they span a wide

range of parameter choices. Since publication, however, two of these points have been ruled out by the 2012 bounds on the Higgs mass. The third benchmark point (featuring a medium-sized LSP at 94.07 GeV) is also an unlikely scenario on the basis of an accompanying light  $M_{Z'} = 1850.4$  GeV, below the most recent LHC constraints on  $Z'$  bosons.

A more recent survey [109] conducted in 2015 singled out a number of benchmark points for an even more constrained version of the  $E_6$ SSM (no inert Higgsinos or inert singlinos), focusing on scenarios satisfying  $s = 650$  TeV,  $\tan\beta = 10$  and small values of  $\mu_{\text{eff}}$ , noting that the SI cross section increases when the lightest neutralino is a combination of bino and Higgsino. This survey demonstrated that this version of the  $E_6$ SSM is still viable in the light of the most recent LHC data. The greatest cross section,  $\sigma_{\text{SI}}^{\text{p}} = 6.16 \times 10^{-45}$  cm<sup>2</sup>, was obtained with a neutralino mass  $m_{\chi_1^0} = 409$  GeV, bino content 60.87%, wino content 0.75% and Higgsino content 38.38%.

However, what will follow in the last part of my thesis is a presentation of original work exploring the present viability of the  $E_6$ SSM with a 10-component neutralino LSP as a dark matter WIMP candidate instead, like [108]. Additional benchmark points must be suggested to augment the known regions of interest of this supersymmetric model. The next chapter will first present an explanation of the computational tools used; this will be followed by the results of the parameter survey.



---

# Programs and Interfaces: micrOMEGAs, FlexibleSUSY and MultiNest

---

This chapter will detail the technical work undertaken in order to prepare our programs to give us the requisite SI WIMP-nucleon cross sections with the level of accuracy that we desire for extended scanning of the  $E_6$ SSM. As with the NMSSM, micrOMEGAs was used (this time in conjunction with an  $E_6$ SSM spectrum generator) to produce the full spectrum of masses, decay rates, relic densities and cross sections. However, we also required it to use renormalization group equations (RGEs) to appropriately evolve certain parameters, which we achieved by interfacing it with an additional program, FlexibleSUSY [117]. Finally, since we also desired a more sophisticated plotting and sampling method than grid scanning, we used a nested sampling program named MultiNest [118–120] to call the micrOMEGAs routine. By using a “likelihood” based on constraints on cross section (from LUX), relic density (from WMAP) and the Higgs mass, MultiNEST preferentially selected the most interesting regions of the parameter space.

## 7.1 micrOMEGAs

micrOMEGAs was already used extensively in the original work presented on the NMSSM, but as this chapter covers the technical aspects of the  $E_6$ SSM project, it is prudent to explain the package in further detail, particularly the manner of its relic density calculation.

Fig. 7.2 is a flow chart depicting the order of operations of micrOMEGAs. By default the micrOMEGAs package does not come with the  $E_6$ SSM model, but such a model

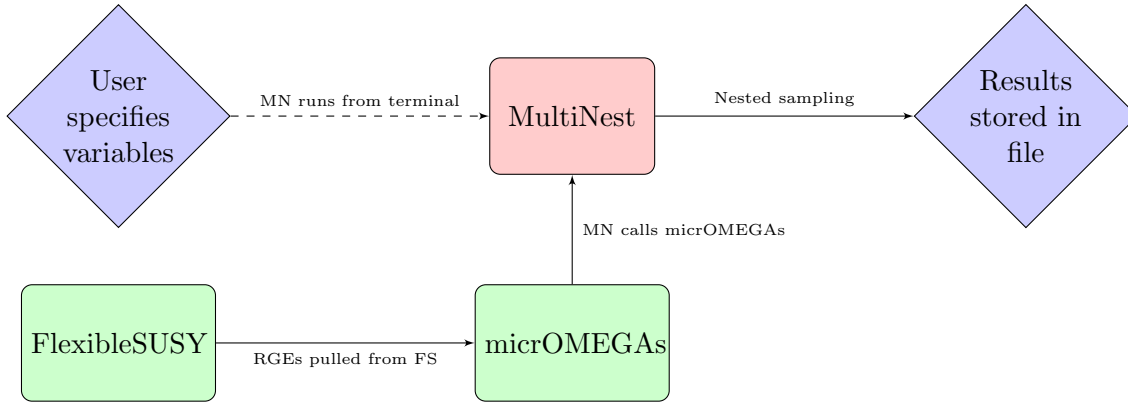


**Figure 7.1:** *micrOMEGAs*, *FlexibleSUSY* and *MultiNest* working together.

may be added to it by using CalcHEP model files, as demonstrated by [108]. Our `.mdl` model files for the  $E_6$ SSM were authored by Jonathan Hall using LanHEP (these were subsequently converted to CalcHEP format). These files, which specify the particles, vertices, parameters (both free and constrained) and Feynman rules, were linked with a private spectrum generator (first used for [105,106]) to calculate the masses and couplings in the  $cE_6$ SSM. *micrOMEGAs* uses these and matrix elements from CalcHEP (in addition to a variety of auxilliary routines containing the effective couplings, collider constraints, etc) to calculate all tree-level cross sections. The final output contains the full spectrum of particle masses in addition to the dark matter relic density, indirect and direct WIMP-nucleon detection rates (as well as rates for the indirect detection of  $e^+$ ,  $\bar{p}$ ,  $\gamma$ ,  $\nu$ ), and expected cross sections and branching ratios for particles in colliders.

The relic density,  $\Omega h^2$ , is calculated by the `darkOmega` function in *micrOMEGAs*:

---

```
omega = darkOmega(&Xf, fast, Beps);
```

---

`fast` and `Beps` are input parameters, the first controlling whether or not the user wishes for faster, more optimized calculations and the second defining the number of channel contributions. `Xf` is an output evaluated by `darkOmega`, related to the freeze-out temperature  $T_f$ :

$$X_f = \frac{M_{cdm}}{T_f}. \quad (7.1)$$

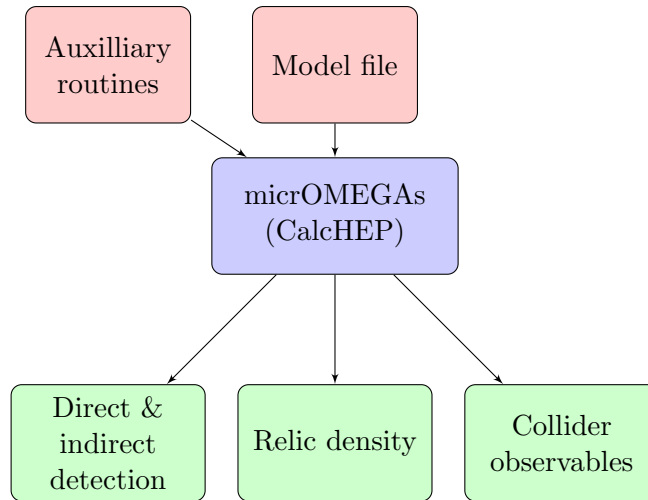


**Figure 7.2:** Flow chart of micrOMEGAs.

The input parameters are contained within a `.oc` file; for instance, the following `benchmark.oc` is an example for a single point in parameter space, where  $x_{u2}$  and  $x_{u1}$  are  $SH_{dj}H_{u3}$  couplings with  $j = 1, 2$ ,  $x_{d2}$  and  $x_{d1}$  are  $SH_{d3}H_{uk}$  couplings with  $k = 1, 2$ , and finally  $\lambda_{mn}$  are  $SH_{dm}H_{un}$  couplings with  $m, n = 1, 2$ :

---

```

600 //TMSSM;
3000 //TESSM;

0.0403 //l22;
0.0001 //l21;
0.0001 //l12;
0.1 //l11;

0.012 //xd2;
0.005 //xd1;
0.012 //xu2;
0.005 //xu1;

0. //Msig2;
0. //Msig1;

0 //Indicates fixed variable
  
```

---

```

-0.37 //lambda;

0
0.18 //kappa;

0
4400 //s;

0
10 //tan beta;

```

---

This may be easily modified if the user wishes the routine to act on a range of parameters. *micrOMEGAs* is executed by `omegaCon.cpp`, which reads the input parameters from `benchmark.oc` and other hardwired parameters from `vars`:

---

```
./omegaCon vars benchmark.oc
```

---

The output is a full spectrum including particle masses, the relic density (including contributing channels) and SI WIMP-nucleon cross section. Some of the relevant details from the output for this particular example are summarised below - for our benchmark the relic density  $\Omega h^2$  is 0.1036 and the SI WIMP-nucleon cross section is  $2.534 \times 10^{-48}$   $\text{cm}^{-2}$ :

---

Masses of odd sector Particles:

```

~o1  : MNE1  =   114.5 || ~1+  : MC1   =   126.4 || ~o2  : MNE2  =
      126.4
~o3  : MNE3  =   126.5 || ~2+  : MC2   =   203.2 || ~o4  : MNE4  =
      203.2
~o5  : MNE5  =   311.3 || ~3+  : MC3   =   311.3 || ~o6  : MNE6  =
      311.3
~e4  : MSe2  =   519.2 || ~e5  : MSmu2 =   519.2 || ~n1  : MSne  =
      609.3

```

---

```

~n2 : MSnu = 609.3 || ~e1 : MSe1 = 614.4 || ~e2 : MSmu1 =
614.4
~t1 : MStop1= 625.3 || ~g : MSG = 626.9 || ~e3 : MStau1=
718.8
~n3 : MSntau= 945.6 || ~e6 : MStau2= 949.2 || ~b1 : MSbot1=
1009.1
~u2 : MSu2 = 1055.5 || ~c2 : MSc2 = 1055.5 || ~d2 : MSd2 =
1056.4
~s2 : MSs2 = 1056.4 || ~t2 : MStop2= 1068.8 || ~u1 : MSu1 =
1110.1
~c1 : MSc1 = 1110.1 || ~d1 : MSd1 = 1112.9 || ~s1 : MSs1 =
1112.9
~o7 : MNE7 = 1194.5 || ~o8 : MNE8 = 1194.8 || ~4+ : MC4 =
1196.1
~b2 : MSbot2= 1265.1 || ~o9 : MNE9 = 1572.3 || ~oA : MNEA =
1688.7

```

```

Dark Matter candidate is ~o1
Xf=26.63068182 Omega=0.1035736566

```

```

Omega h^2
-----
0.1035736566

```

```

SI N1-p cross-section from (h1, h2, h3, all)
-----

```

```

5.626096815e-08
2.411230352e-08
5.357462255e-14
2.534261104e-48

```

---

## 7.2 FlexibleSUSY

An unfortunate shortcoming of the  $E_6$ SSM model extension that we used in *micrOMEGAs* is its inability, by itself, to evolve couplings such as the trilinear scalar couplings. We needed to vary parameters that violate  $Z_2^H$  symmetry and allow for the possibility that they can become large. We thus required an additional method of obtaining the RGEs, so we turned to a new program called *FlexibleSUSY*.

*FlexibleSUSY* is a ‘spectrum generator generator.’ Written in C++, it uses the Mathematica package *SARAH* [121] and components from *SOFTSUSY* [122] to create a custom spectrum generator for a user-specified physical model, numerically solving tree-level expressions for its mass matrices, EWSB conditions, two-loop RGEs and one-loop self energies. The advantage of this is that it is extremely flexible, and can be adapted for a number of different extensions of supersymmetry (unlike generators that contain hard-coded information about particular models, such as *NMSSMTools* and *SOFTSUSY*).

Firstly, the user provides *FlexibleSUSY* with *SARAH* model files. Within the `/sarah` subdirectory in *FlexibleSUSY* are three files (`E6SSM.m`, `parameters.m` and `particles.m`) containing the model information. The following example code is taken from `E6SSM.m`, demonstrating how it specifies global symmetries, vector superfields, chiral superfields and the superpotential:

---

```
Off[General::spell]

Model`Name = "E6SSM";
Model`NameLaTeX = "E6SSM";
Model`Authors = "Sophie Underwood";
Model`Date = "2013-11-10";

(*-----*)
(* Particle Content*)
(*-----*)

(* Global symmetries *)
```

---

```

Global[[1]] = {Z[2],RParity};
RpM = {-1,-1,1};
RpP = {1,1,-1};

(* Vector Superfields *)

Gauge[[1]]={B, U[1], hypercharge, g1,False,RpM};
Gauge[[2]]={WB, SU[2], left, g2,True, RpM};
Gauge[[3]]={G, SU[3], color, g3,False,RpM};
Gauge[[4]]={Bp, U[1], Ncharge, g1p,False,RpM};

(* Chiral Superfields *)

SuperFields[[1]] = {q, 3, {uL, dL}, 1/6, 2, 3, 1, RpM};
SuperFields[[2]] = {l, 3, {vL, eL}, -1/2, 2, 1, 2, RpM};
SuperFields[[3]] = {Hd,1, {Hd0, HdM}, -1/2, 2, 1, -3, RpP};
SuperFields[[4]] = {Hu,1, {Hup, Hu0}, 1/2, 2, 1, -2, RpP};

SuperFields[[5]] = {d, 3, conj[dR], 1/3, 1, -3, 2, RpM};
SuperFields[[6]] = {u, 3, conj[uR], -2/3, 1, -3, 1, RpM};
SuperFields[[7]] = {e, 3, conj[eR], 1, 1, 1, 1, RpM};
SuperFields[[8]] = {s, 1, sR, 0, 1, 1, 5, RpP};

SuperFields[[9]] = {H11I, 1, {H11I0, H11Im}, -1/2, 2, 1, -3, RpP
};

SuperFields[[10]] = {H21I, 1, {H21Ip, H21I0}, 1/2, 2, 1, -2, RpP
};

SuperFields[[11]] = {H12I, 1, {H12I0, H12Im}, -1/2, 2, 1, -3, RpP
};

SuperFields[[12]] = {H22I, 1, {H22Ip, H22I0}, 1/2, 2, 1, -2, RpP
};

SuperFields[[13]] = {sI, 2, sIR, 0, 1, 1, 5, RpP};
SuperFields[[14]] = {Dx, 3, DxL, -1/3, 1, 3, -2, RpP};

```

---

```

SuperFields[[15]] = {Dxbar, 3, conj[DxbarR], 1/3, 1, -3, -3, RpP};

SuperFields[[16]] = {Hp, 1, {Hp0, Hpdm}, -1/2, 2, 1, 2, RpP};
SuperFields[[17]] = {Hpbar, 1, {Hpup, Hpu0}, 1/2, 2, 1, -2, RpP};
NoU1Mixing=True;
AddMixedSofts = False;

(*-----*)
(*Z2H exact Superpotential *)
(*-----*)

SuperPotential = Yu u.q.Hu - Yd d.q.Hd - Ye e.l.Hd + \[Lambda] s.Hu
.Hd + \[Lambda]1 s.H21I.H11I + \[Lambda]2 s.H22I.H12I + \[
Kappa] s.Dx.Dxbar + \[Mu]Pr Hpbar.Hp + Xu1 s.Hu.H11I + Xu2 s.Hu
.H12I + Xd1 s.H21I.Hd + Xd2 s.H22I.Hd ;

```

---

A simple set of commands in the terminal builds this user-specified model:

---

```

$ ./createmodel --models=E6SSM
$ ./configure --with-models=E6SSM
$ make

```

---

Once the model of E<sub>6</sub>SSM has been created, its SUSY parameter, soft-breaking parameter and  $\beta$ -function files are stored within the FlexibleSUSY/Models/E6SSM/ directory. A class hierarchy is implemented in which E6SSM\_susy\_parameters inherits from Beta\_functions while E6SSM\_soft\_parameters inherits from E6SSM\_susy\_parameters. These two classes are derived from the parameters of the SARAH model file, and allow renormalization group running of the model parameters. The two-loop RGEs of  $T_{Y_U}$ ,  $T_{Y_d}$ ,  $T_{Y_3}$ ,  $T_{X_u}$ ,  $T_{X_d}$ ,  $T_\lambda$ ,  $T_\kappa$ ,  $T_{\lambda_{ij}}$  and  $T_{B'_\mu}$  were included to be solved by FlexibleSUSY. As an

example, the two-loop RGEs of the trilinear  $\lambda$  and  $\kappa$  in particular are:

$$\begin{aligned} \frac{dA_{\lambda_i}}{dt} &= \frac{1}{(4\pi)^2} \left[ 4\lambda_i^2 A_{\lambda_i} + 4 \sum_{A_\lambda} + 6 \sum_{A_\kappa} + (6h_t^2 A_t + 6h_b^2 A_b + 2h_\tau^2 A_\tau) \delta_{i3} \right. \\ &\quad \left. - 6g_2^2 M_2 - \frac{6}{5} g_1^2 M_1 - \frac{19}{5} g_1'^2 M_1' + \frac{\beta_{A_{\lambda_i}}^{(2)}}{(4\pi)^2} \right], \end{aligned} \quad (7.2)$$

$$\begin{aligned} \frac{dA_{\kappa_i}}{dt} &= \frac{1}{(4\pi)^2} \left[ 4\kappa_i^2 A_{\kappa_i} + 4 \sum_{A_\lambda} + 6 \sum_{A_\kappa} - \frac{32}{3} g_3^2 M_3 - \frac{8}{15} g_1^2 M_1 \right. \\ &\quad \left. - \frac{19}{5} g_1'^2 M_1' + \frac{\beta_{A_{\kappa_i}}^{(2)}}{(4\pi)^2} \right], \end{aligned} \quad (7.3)$$

where the  $\beta$ -functions are given by:

$$\begin{aligned} \beta_{A_{\lambda_i}}^{(2)} &= -4\lambda_i^2 \left( \lambda_i^2 + 2 \sum_{\lambda} + 3 \sum_{\kappa} \right) A_{\lambda_i} - 4\lambda_i^2 \left( \lambda_i^2 A_{\lambda_i} + 2 \sum_{A_\lambda} + 3 \sum_{A_\kappa} \right) - 16\Pi_{A_\lambda} \\ &\quad - 24\Pi_{A_\kappa} - 2\lambda^2 (3h_t^2 + 3h_b^2 + h_\tau^2) (2 + \delta_{i3}) A_\lambda \\ &\quad - 2\lambda^2 (3h_t^2 A_t + 3h_b^2 A_b + h_\tau^2 A_\tau) (2 + \delta_{i3}) \\ &\quad - 12 [3h_t^4 A_t + 3h_b^4 A_b + h_t^2 h_b^2 (A_t + A_b) + h_\tau^4 A_\tau] \delta_{i3} \\ &\quad + 32g_3^2 \left( \sum_{\kappa} M_3 + \sum_{A_\kappa} \right) + 12g_2^2 \left( \sum_{\lambda} M_2 + \sum_{A_\lambda} \right) \\ &\quad + 2g_i^2 \left[ \left( \frac{4}{5} \sum_{\kappa} + \frac{6}{5} \sum_{\lambda} \right) M_1 + \frac{4}{5} \sum_{A_\kappa} + \frac{6}{5} \sum_{A_\lambda} \right] \\ &\quad + 2g_2'^2 \left[ \left( \frac{5}{2} \lambda_i^2 - \frac{9}{5} \sum_{\kappa} - \frac{6}{5} \sum_{\lambda} \right) M_1' + \frac{5}{2} \lambda_i^2 A_{\lambda_i} - \frac{9}{5} \sum_{A_\kappa} - \frac{6}{5} \sum_{A_\lambda} \right] \\ &\quad + 32g_3^2 [(h_t^2 + h_b^2) M_3 + h_t^2 A_t + h_b^2 A_b] \delta_{i3} \\ &\quad + 2g_1^2 \left[ \left( \frac{4}{5} h_t^2 - \frac{2}{5} h_b^2 + \frac{6}{5} h_\tau^2 \right) M_1 + \frac{4}{5} h_t^2 A_t - \frac{2}{5} h_b^2 A_b + \frac{6}{5} h_\tau^2 A_\tau \right] \delta_{i3} \\ &\quad + g_1'^2 \left[ \left( -\frac{3}{5} h_t^2 - \frac{2}{5} h_b^2 - \frac{2}{5} h_\tau^2 \right) M_1' - \frac{3}{5} h_t^2 A_t - \frac{2}{5} h_b^2 A_b - \frac{2}{5} h_\tau^2 A_\tau \right] \delta_{i3} \\ &\quad + 12g_2^4 \left( 3N_g - \frac{7}{2} \right) M_2 + \frac{12}{5} g_1^4 \left( 3N_g + \frac{9}{10} \right) M_1 + \frac{39}{5} g_1'^4 \left( 3N_g + \frac{27}{20} \right) M_1' \\ &\quad + \frac{18}{5} g_2^2 g_1^2 (M_2 + M_1) + \frac{39}{10} g_2^2 g_1'^2 (M_2 + M_1') + \frac{39}{50} g_1^2 g_1'^2 (M_1 + M_1'), \end{aligned} \quad (7.4)$$

$$\begin{aligned}
\beta_{A_{\kappa_i}}^{(2)} = & -4\kappa_i^2 \left( \kappa_i^2 + 2 \sum_{\lambda} + 3 \sum_{\kappa} \right) A_{\kappa_i} - 4\kappa_i^2 \left( \kappa_i^2 A_{\kappa_i} + 2 \sum_{A_{\lambda}} + 3 \sum_{A_{\kappa}} \right) - 16\Pi_{A_{\lambda}} \\
& - 24\Pi_{A_{\kappa}} - 4\lambda^2 (3h_t^2 + 3h_b^2 + h_{\tau}^2) A_{\lambda} - 4\lambda^2 (3h_t^2 A_t + 3h_b^2 A_b + h_{\tau}^2 A_{\tau}) \\
& + 32g_3^2 \left( \sum_{\kappa} M_3 + \sum_{A_{\kappa}} \right) + 12g_2^2 \left( \sum_{\lambda} M_2 + \sum_{A_{\lambda}} \right) \\
& + 2g_i^2 \left[ \left( \frac{4}{5} \sum_{\kappa} + \frac{6}{5} \sum_{\lambda} \right) M_1 + \frac{4}{5} \sum_{A_{\kappa}} + \frac{6}{5} \sum_{A_{\lambda}} \right] \\
& + 2g_2'^2 \left[ \left( \frac{5}{2} \kappa_i^2 - \frac{9}{5} \sum_{\kappa} - \frac{6}{5} \sum_{\lambda} \right) M_1' + \frac{5}{2} \kappa_i^2 A_{\kappa_i} - \frac{9}{5} \sum_{A_{\kappa}} - \frac{6}{5} \sum_{A_{\lambda}} \right] \\
& + \frac{64}{3} g_3^4 \left( 3N_g - \frac{19}{3} \right) M_3 + \frac{16}{15} g_1^4 \left( 3N_g + \frac{11}{15} \right) M_1 + \frac{38}{5} g_1'^4 \left( 3N_g + \frac{27}{20} \right) M_1' \\
& + \frac{128}{45} g_3^2 g_1^2 (M_3 + M_1) + \frac{104}{15} g_3^2 g_1'^2 (M_3 + M_1') + \frac{26}{75} g_1^2 g_1'^2 (M_1 + M_1'), \quad (7.5)
\end{aligned}$$

where

$$\sum_{A_{\lambda}} = \lambda_1^2 A_{\lambda_1} + \lambda_2^2 A_{\lambda_2} + \lambda_3^2 A_{\lambda_3}, \quad (7.6)$$

$$\sum_{A_{\kappa}} = \kappa_1^2 A_{\kappa_1} + \kappa_2^2 A_{\kappa_2} + \kappa_3^2 A_{\kappa_3}, \quad (7.7)$$

$$\Pi_{\lambda} = \lambda_1^4 A_{\lambda_1} + \lambda_2^4 A_{\lambda_2} + \lambda_3^4 A_{\lambda_3}, \quad (7.8)$$

$$\Pi_{\kappa} = \kappa_1^4 A_{\kappa_1} + \kappa_2^4 A_{\kappa_2} + \kappa_3^4 A_{\kappa_3}. \quad (7.9)$$

The solution to the trilinear scalar couplings takes the form:

$$A_i(t) = e_i(t) A_0 + f_i(t) M_{1/2}, \quad (7.10)$$

where  $t = \ln \frac{Q}{M_X}$ , in which  $Q$  is a renormalization scale. This in turn leads to the solution for the RGEs for the soft scalar masses. However, exact analytic solutions of each of the RGEs are unknown, which also means that an analytic expression for the function  $e_i(t)$  cannot be written.

FlexibleSUSY handles the RGEs by integrating them between the GUT scale (at which point the scalar masses and gauge masses are unified at  $m_0$  and  $M_{1/2}$  respectively) and the low energy SUSY scale using an adaptive Runge-Kutta algorithm. This is an itera-

tive process that necessitates calculating the  $\beta$ -functions approximately 50 times, which FlexibleSUSY handles by employing a fast linear algebra package (Eigen [123]).

### 7.3 Interfacing FlexibleSUSY and MicrOMEGAs

Each parameter must be passed between FlexibleSUSY and MicrOMEGAs. In order to achieve this, a direct interface was set up inside the file `essmsoftpars.cpp` within the `micromegas_2.4.5/E6SSM/con` directory.

The interface begins with:

---

```
flexiblesusy::SophieE6SSM_susy_parameters FlexiSusyPars;
```

---

This creates a new constructor called `FlexiSusyPars`. Beneath this line, each parameter in FlexibleSUSY can be pointed to according to the naming convention within micrOMEGAs. For example, the following lines deal with the  $\lambda$  and  $\kappa$  parameters, which are called `Lambdax`, `Lambda3` and `Kappa(double matrix)` in FlexibleSUSY and `displaylambda`, `displaylambda3` and `Kappa(double vector)` in micrOMEGAs:

---

```

//Lambdas
FlexiSusyPars.set_Lambdax(0,0,-displaylambda(1,1));
FlexiSusyPars.set_Lambdax(0,1,-displaylambda(1,2));
FlexiSusyPars.set_Lambdax(1,0,-displaylambda(2,1));
FlexiSusyPars.set_Lambdax(1,1,-displaylambda(2,2));
FlexiSusyPars.set_Lambda3(-displaylambda3());

//Kappas
DoubleVector kappa = displaykappa();
FlexiSusyPars.set_Kappa(0,0,-kappa(1));
FlexiSusyPars.set_Kappa(1,1,-kappa(2));
FlexiSusyPars.set_Kappa(2,2,-kappa(3));
FlexiSusyPars.set_Kappa(0,1,0.);
FlexiSusyPars.set_Kappa(0,2,0.);
FlexiSusyPars.set_Kappa(1,0,0.);
FlexiSusyPars.set_Kappa(1,2,0.);

```

---

```

FlexiSusyPars.set_Kappa(2,0,0.);
FlexiSusyPars.set_Kappa(2,1,0.);

```

---

This is done for each and every variable in the E6SSM model. Directly beneath these blocks lies another constructor that deals with the reverse: mapping each parameter in *micrOMEGAs* to their equivalents in *FlexibleSUSY*.

---

```

flexiblesusy::SophieE6SSM_soft_parameters FlexiBetas =
    FlexiSoftPars.calc_beta();
static SoftParsEssm dsoft;

//Lambda
dsoft.setlambda(1,1,-FlexiBetas.get_Lambdax(0,0));
dsoft.setlambda(1,2,-FlexiBetas.get_Lambdax(0,1));
dsoft.setlambda(2,1,-FlexiBetas.get_Lambdax(1,0));
dsoft.setlambda(2,2,-FlexiBetas.get_Lambdax(1,1));
dsoft.setlambda3(-FlexiBetas.get_Lambda3());

//Kappas
DoubleVector kap(3);
kap(1) = FlexiBetas.get_Kappa(0,0);
kap(2) = FlexiBetas.get_Kappa(1,1);
kap(3) = FlexiBetas.get_Kappa(2,2);
dsoft.setkappa(-1.0 * kap);

```

---

The final result is a version of *micrOMEGAs* that successfully incorporates the missing two-loop RGEs for our E<sub>6</sub>SSM model. The only task left is to change the sampling method to one based on likelihood.

## 7.4 MultiNest

MultiNest is a Bayesian inference tool that uses the nested sampling method to calculate the Bayesian evidence for a model and assign relative probabilities to model outcomes.

Bayesian inference utilises Bayes' Theorem to update the probability of a particular hypothesis according to observed data. This theorem states that:

$$\Pr(\Theta | \mathbf{D}, H) = \frac{\Pr(\mathbf{D} | \Theta, H)\Pr(\Theta | H)}{\Pr(\mathbf{D} | H)}, \quad (7.11)$$

or in more condensed form:

$$\mathcal{P}(\Theta) = \frac{\mathcal{L}(\Theta)\pi(\Theta)}{\mathcal{Z}}, \quad (7.12)$$

where  $H$  is the hypothesis or model,  $\Theta$  are its parameters,  $\mathbf{D}$  is the data,  $\Pr(\Theta | \mathbf{D}, H) \equiv \mathcal{P}(\Theta)$  is the posterior probability distribution of the parameters (“the probability of observing parameters  $\Theta$  given data  $\mathbf{D}$  that has already been observed”),  $\Pr(\Theta | H) \equiv \pi(\Theta)$  is the prior (“the probability of observing parameters  $\Theta$  before new data  $\mathbf{D}$  is observed”),  $\Pr(\mathbf{D} | \Theta, H) \equiv \mathcal{L}(\Theta)$  is the likelihood (“the probability of observing data  $\mathbf{D}$  given parameters  $\Theta$ ”) and finally,  $\Pr(\mathbf{D} | H) \equiv \mathcal{Z}$  is the Bayesian evidence (“the probability of data  $\mathbf{D}$  without regard to parameters  $\Theta$ ”).  $\mathcal{Z}$  effectively serves as a normalization constant, given by:

$$\mathcal{Z} = \int \mathcal{L}(\Theta)\pi(\Theta)d^D\Theta, \quad (7.13)$$

where  $D$  is the number of dimensions of the parameter space. Unfortunately, the posterior cannot be evaluated analytically, since we are working with a model with ten free parameters, resulting in a complex, multi-dimensional posterior function. This necessitates the use of sampling algorithms.

MultiNest employs an approach known as nested sampling, in which the multi-dimensional evidence integral is converted into a much simpler one-dimensional integral (which is calculated using Monte Carlo integration), with the posterior being calculated as a by-product. This is an improvement on older Markov Chain Monte Carlo (MCMC) techniques.

The prior volume is given by:

$$X(\lambda) = \int_{\mathcal{L}(\Theta) > \lambda} \pi(\Theta)d^D\Theta, \quad (7.14)$$

$$dX = \pi(\Theta)d^D(\Theta). \quad (7.15)$$

This integral is carried out over the regions of parameter space inside the iso-likelihood

contour  $\mathcal{L}(\Theta) = \lambda$ . It follows that the evidence integral can be written as:

$$\mathcal{Z} = \int_0^1 \mathcal{L}(X) dX. \quad (7.16)$$

$\mathcal{L}$  decreases monotonically with  $X$ . This may be illustrated with a simple two dimensional example, given in Fig. 7.3. The nested sampling algorithm computes the evidence  $\mathcal{Z} = \sum_{i=1}^M \mathcal{L}w_i$  by first setting a number of live points  $M_{\text{live}}$  from the prior, and setting the initial prior volume to unity. The process is iterative: the algorithm sweeps through nested shells (narrowing the prior volume down to regions of higher and higher likelihood) and works by elimination. The point with the lowest likelihood ( $\mathcal{L}_i$ ) is removed from the  $i^{\text{th}}$  set of live points and replaced with another point from the prior chosen under the condition that its associated likelihood is greater than the minimum likelihood that was just removed.

This nested sampling process in MultiNest was used to efficiently scan the parameter range based on the data fed into it from FlexibleSUSY and micrOMEGAs, homing in on regions of high “likelihood”. Instead of calling micrOMEGAs, the user now begins by calling MultiNest (see Fig. 7.1), which we modified to include relevant code from `omegaCon.cpp` in micrOMEGAs.

Each parameter is placed in an `enum` string in the `.cc` file used to create the MultiNest routine, with the first ten (out of 69 total) being the free parameters (number of dimensions):

$$x_{d2} \ x_{u2} \ x_{d1} \ x_{u1} \ \lambda_{11} \ \lambda_{22} \ \lambda \ \tan\beta \ s \ \kappa, \quad (7.17)$$

where:

$$x_{d2} = \lambda_{332}, \quad (7.18)$$

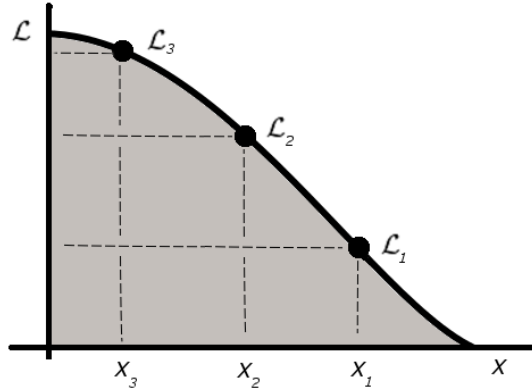
$$x_{d1} = \lambda_{331}, \quad (7.19)$$

$$x_{u2} = \lambda_{323}, \quad (7.20)$$

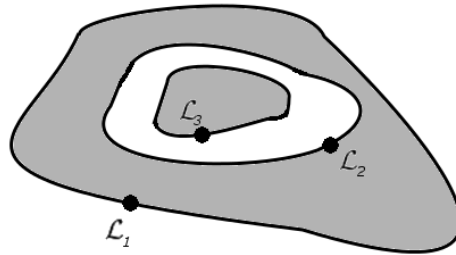
$$x_{u1} = \lambda_{313}, \quad (7.21)$$

$$\lambda_{11} = \lambda_{311}, \quad (7.22)$$

$$\lambda_{22} = \lambda_{322}. \quad (7.23)$$



(a)  $\mathcal{L}(X)$  function, decreasing monotonically with  $X$ . The grey area beneath this function is the evidence  $\mathcal{Z} = \sum_{i=1}^M \mathcal{L}_i w_i = \frac{1}{2} \sum_{i=1}^M \mathcal{L}_i (X_{i-1} - X_{i+1})$  (using the trapezium rule).



(b) The posterior of a simple two-dimensional problem.

**Figure 7.3:** Graphical illustration of the calculation of  $\mathcal{Z}$ .

with  $\lambda_{ijk}$  being the trilinear coupling of  $S_i H_{dj} H_{uk}$  (see Eq. (6.5)).  $\lambda_{21} = \lambda_{321}$  and  $\lambda_{12} = \lambda_{312}$  were both kept fixed at 0.0001.

These ten parameters are placed in an array called `Cube` to represent the parameter space. MultiNest performs all sampling within this unit hypercube, and it is up to the user to convert the sampled parameters to the ranges of interest. We do this by scaling each `Cube[i]` to fit the prior range.

---

```
enum{Xu2 ,Xd2 ,Xu1 ,Xd1 ,L ,T ,S ,K ,L22 ,L11 ,
      L21 ,L12 ,tmssm ,tessm ,MSIG1 ,MSIG2 ,Sigmapar ,Omegapar ,hMass1 ,
      nMass1 ,
      Mass1 ,
      nMixing11 ,nMixing12 ,nMixing13 ,nMixing14 ,nMixing15 ,
```

```

nMixing16,nMixing17,nMixing18,nMixing19,nMixing110,
nMixing21,nMixing22,nMixing23,nMixing24,nMixing25,
nMixing26,nMixing27,nMixing28,nMixing29,nMixing210,
nMixing31,nMixing32,nMixing33,nMixing34,nMixing35,
nMixing36,nMixing37,nMixing38,nMixing39,nMixing310,
M1stop,M2stop,M1sbot,M2sbot,Msd1,Msul,Msur,Msdr,Siglim,
gMass,m12,M0,a0,alambda,Lambda,m2,m1primed,
nSol};

cout << "after enum" << endl;
double l22, l21, l12, l11;
double xd2, xd1, xu2, xu1;
double Msig1, Msig2;
double TMSSM, TESSM;
double l;
double k;
double s;
double t;
//Set prior range on parameters
double min[10];
double max[10];
min[Xd2]=0.001;max[Xd2]=0.5;
min[Xu2]=0.001;max[Xu2]=0.5;
min[Xd1]=0.001;max[Xd1]=0.5;
min[Xu1]=0.001;max[Xu1]=0.5;
min[T]=1;max[T]=40;
min[L]=-1.0;max[L]=1.0;
min[S]=0;max[S]=100000;
min[L11]=0.0001;max[L11]=1.0;
min[L22]=0.0001;max[L22]=1.0;
min[K]=0.01;max[K]=1.0;

```

---

```

xd1=Cube[Xd1];
xu1=Cube[Xu1];
xd2=Cube[Xd2];
xu2=Cube[Xu2];

```

---

```

l22=Cube [L22];
l11=Cube [L11];

t=Cube [T];
k=Cube [K];
l=Cube [L];
s=Cube [S];

```

---

These `Cube[i]` points are passed to the `micrOMEGAs` code, which outputs the relic density and SI cross section. These are subsequently fed into a likelihood function inside `E6SSM.cc`, `lnew`, which also contains relevant constraints on the Higgs mass (from the LHC), the relic density (from the Planck experiment), and the SI WIMP-nucleon cross section (from LUX):

---

```

gsl_interp_accel *acc = gsl_interp_accel_alloc ();
gsl_spline *spline = gsl_spline_alloc (gsl_interp_cspline,83);
luxinterp(acc,spline);
double siglim = 0.0;
int overspillLow=0;
int overspillHigh=0;
if (nMass[1] > 5100){
    siglim = 1.0e-3;
    overspillHigh++;
}
else if (nMass[1] < 5.5256){
    siglim = 1.0e-3;
    overspillLow++;
}
else{
    siglim = gsl_spline_eval(spline,nMass[1],acc)*pow(10,-36); \\a
    routine feeding LUX data into the limit on cross section
    Sigma
}
logLikeSigma = -pow((Sigma - siglim)/(0.5*siglim),2);

```

```
lnew = -pow((hMass[1] - 125.3)/sqrt(0.41),2) - pow((Omega -  
0.1196)/0.0031,2) + logLikeSigma;
```

---

As MultiNest continues the nested sampling process, each point from the likelihood shells is stored in a `.txt` file, which eventually contains between 30,000 and 40,000 lines for each set of parameters. These may be plotted as heat maps using a simple Gnuplot routine.

The next chapter will present the original results of the most extensive parameter exploration of the  $E_6$ SSM to date.

---

# Results of the E<sub>6</sub>SSM Parameter Scan

---

This chapter presents a sophisticated exploration of the viability of the E<sub>6</sub>SSM model in providing a suitable neutralino dark matter candidate. This work was conducted with sweeping multi-dimensional parameter scans using the programs mentioned in the previous chapter: micrOMEGAs, FlexibleSUSY and MultiNest. The ranges allowed for each parameter are given in Table 8.1.

Parameter	Range	Parameter	Range
$x_{u1}$	0 – 0.5	$x_{u2}$	0 – 0.5
$x_{d1}$	0 – 0.5	$x_{d2}$	0 – 0.5
$\lambda_{11}$	0.0001 – 1.0	$\lambda_{22}$	0.0001 – 1.0
$\tan\beta$	1 - 40	$s$	0 – 100000
$\lambda$	-0.5 – 0.5	$\kappa$	0 – 5

**Table 8.1:** Parameters and their ranges. As already defined in Chapter 7,  $x_{u2}$  and  $x_{u1}$  are  $SH_{dj}H_{u3}$  couplings with  $j = 1, 2$ ,  $x_{d2}$  and  $x_{d1}$  are  $SH_{d3}H_{uk}$  couplings with  $k = 1, 2$ , and finally  $\lambda_{mn}$  are  $SH_{dm}H_{un}$  couplings with  $m, n = 1, 2$ .

The main focus is not only to discover regions of the E<sub>6</sub>SSM parameter space with rich and interesting features for future detection efforts but also to explore the mixing content of the lightest neutralino. A previous study on the EZSSM (with two decoupled inert singlinos, which we have followed in this study) considered scenarios in which the neutralino dark matter is composed heavily of binos [108]. As mentioned in Chapter 6, the three benchmark scenarios in that study have since been ruled out by recent LHC constraints on the lightest Higgs mass (denoted here as  $m_{h_1}$ ) and the  $Z'$  mass  $M_{Z'}$ . In

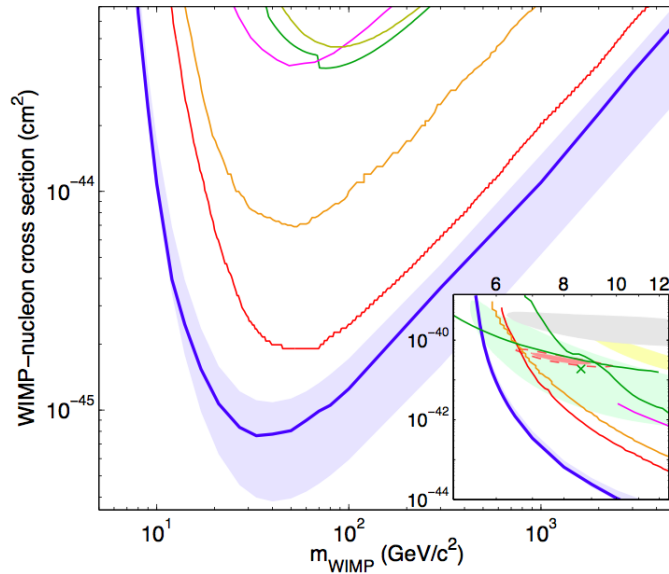


**Figure 8.1:** The LUX exclusion limit on neutralino-hadron scattering cross section used in this scan. This has since been superseded by an updated limit, but it does not impact the viability of the benchmark points obtained in this chapter.

this most recent scan, we found that we could not detect these three benchmark scenarios due to new constraints.

However, what we have found instead is an abundance of scenarios in which the light neutralinos contain greater mixtures of Higgsino and inert Higgsino. These points satisfy the latest constraints from the LHC on gluinos, squarks and the lightest Higgs mass, and offer interesting new solutions to the dark matter problem. Instead of a bino-like WIMP, future detectors may discover a Higgsino-like or inert Higgsino-like WIMP.

## 8.1 The MultiNest Likelihood

As mentioned, the MultiNest likelihood assigned to each of the following points in the multi-dimensional parameter space consists of terms that model measurements of the lightest Higgs mass, the dark matter relic density and also limits on the SI WIMP-nucleon cross section.

$$\log L = - \left( \frac{m_{h_1} - 125.3}{\sqrt{0.41}} \right)^2 - \left( \frac{\Omega h^2 - 0.1196}{0.0031} \right)^2 - \left( \frac{\sigma - \sigma_{\text{lim}}}{0.5\sigma_{\text{lim}}} \right)^2. \quad (8.1)$$

The first term is the constraint from the Higgs mass, assuming a central value of 125.3 GeV. This is using the 2012 CMS result [63] (the Higgs mass measurement has since been slightly improved to  $125.09 \pm 0.21 \pm 0.11$  GeV by combined CMS and ATLAS measurements [124]). The second term is the constraint from the relic density, assuming a central value of  $\Omega h^2 = 0.1196$ . This is using the 2013 value from the Planck collaboration [33]. The third and final term is the constraint on the WIMP-nucleon SI cross section from the 2013 LUX results [56]. Here, the function  $\sigma_{\text{lim}}$  was extrapolated from the 95% confidence level LUX limit in Fig. 8.1 (points were favoured if they were close to the LUX limit, on either side of it). The inclusion of this LUX limit means that this quantity isn't a true likelihood in a statistical sense, but rather a means to ensure that the MultiNest routine will quickly home in on the regions of current observational reach. Note that the LUX limit in Fig. 8.1 has been updated and slightly improved since these scans were conducted [55] - however, the sigma of the Gaussian function selected to represent the old LUX limit in our fake likelihood is still large enough to include a swath of favourable points below the new LUX limit.

It is easy to check that when the Higgs mass and relic density are plotted against each other with the log of this "likelihood" as a heat map, the result is a Gaussian profile centred on  $m_{h_1} = 125.3$  GeV and  $\Omega h^2 = 0.1196$ , as expected from LHC and Planck data respectively (see Fig. 8.2: like other plots in this section, these are binned distributions that have been projected out from the overall sample space).

However, when the neutralino mass is plotted against SI cross section, the points eventually favour a neutralino mass of approximately 1 TeV, extending well below the LUX constraint (see Fig. 8.3), demonstrating that the contributions from relic density and Higgs mass constraints overwhelmingly dominate the likelihood. However, this has still given us a good range of points in near proximity to the LUX dark matter WIMP curve. The majority of benchmark scenarios in this chapter have a neutralino mass close to 1 TeV.

## 8.2 Experimental constraints

Further exclusions on squark and gluino masses based on LHC data can also be applied. Gluino mass limitations are heavily dependent on the neutralino mass. Furthermore, first

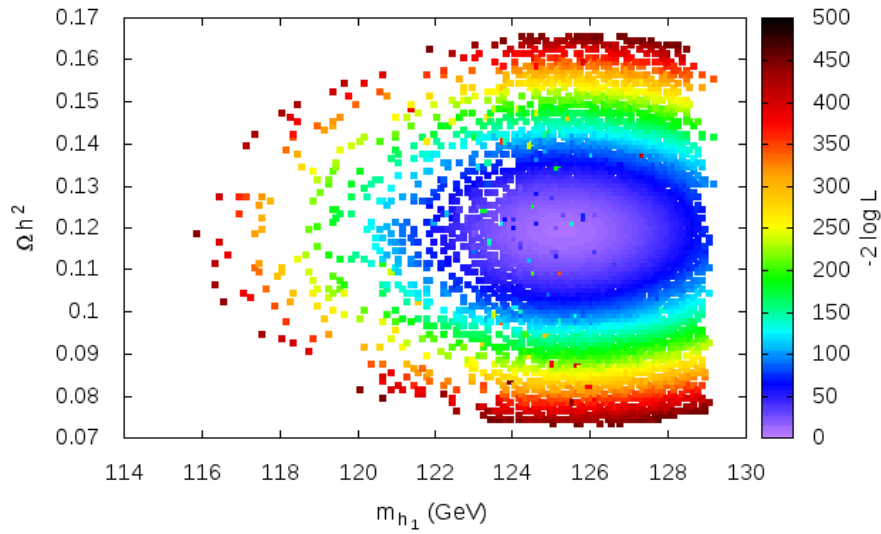


**Figure 8.2:** Gaussian probability centred on  $m_{h_1} = 125.3$  GeV and  $\Omega h^2 = 0.1196$ . Low heat map values represent high likelihood.

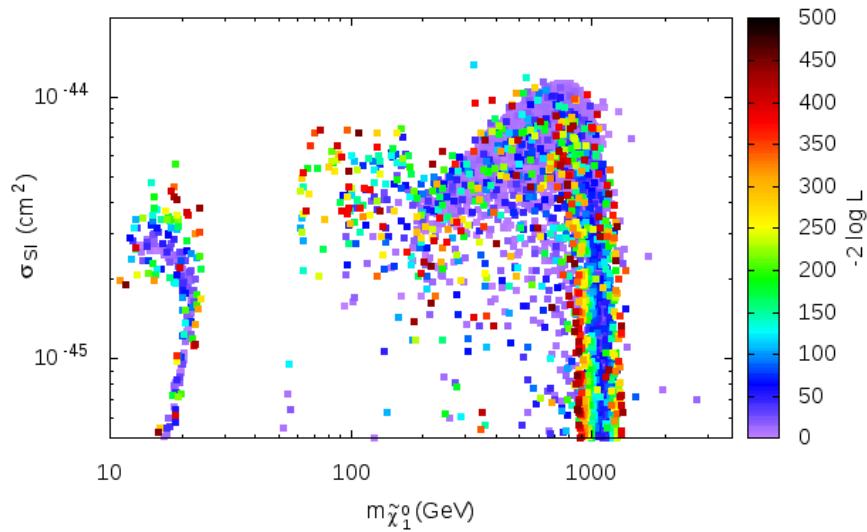


**Figure 8.3:** The SI cross section plotted against the neutralino mass as a function of the fake likelihood. The curve follows the LUX constraint for neutralino masses between 300 GeV and 1 TeV, but at this point curves sharply downwards to favour neutralino masses at 1 TeV.

and second generation squark mass limits vary according to model and experiment. For the Tevatron experiments, and assuming the constrained MSSM, the lower limit on first and second generation squarks is 380 or 390 GeV [125] (the former for all gluino masses, the latter in the case where  $m_{\bar{q}} = m_{\bar{g}}$ ). For the ATLAS collaboration (using 20 fb<sup>-1</sup> of data at 8 TeV), squarks are excluded below 1600 GeV and 1700 GeV ( $m_{\bar{q}} \neq m_{\bar{g}}$  and  $m_{\bar{q}} = m_{\bar{g}}$  respectively). The top and bottom squarks are typically excluded below approximately 600 GeV. For neutralino masses above approximately 300 GeV, no limits can be applied on direct squark production scenarios by LHC experiments.

Of course, the spectrum of the E<sub>6</sub>SSM is radically different from that of the constrained MSSM; comparing exclusion plots based on  $m_0$  and  $M_{1/2}$  is quite difficult, given that these two parameters will result in very different squark and gluino masses in each model after the running of the RGEs is performed. Comparing squark and gluino mass exclusions between the MSSM and E<sub>6</sub>SSM works to a certain extent, but there is some uncertainty introduced by the fact that squarks and gluinos themselves decay to lighter supersymmetric particles, which naturally vary between models; consequently, the decay widths and branching ratios are not identical. For this reason, the squark and gluino limits from dedicated experimental analyses using the MSSM as a model can be used only as a conservative and rough guide for estimates of the constraints on the E<sub>6</sub>SSM.

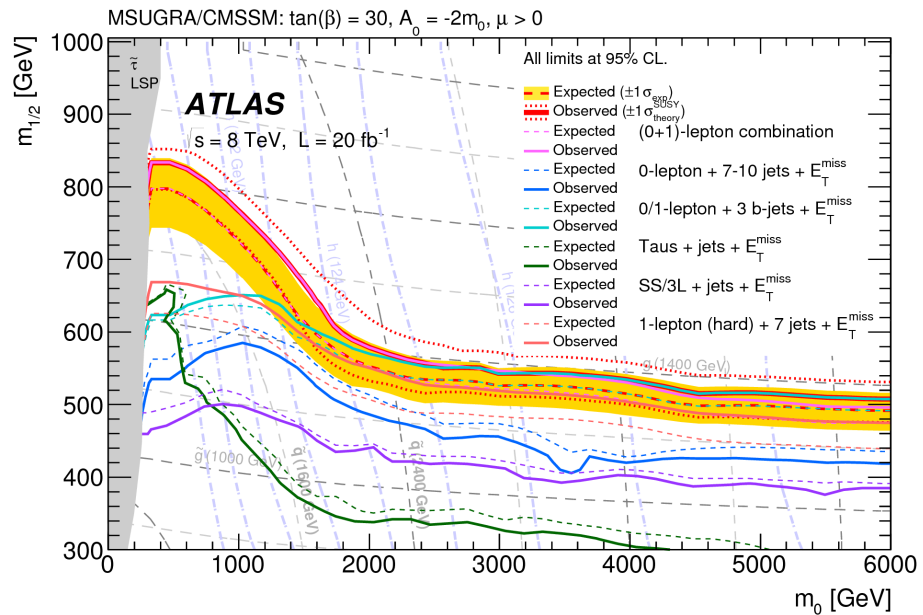


**Figure 8.4:** ATLAS figure (from [126]) displaying the lower bound on the gluino mass in the cMSSM/mSUGRA model.

A previous study on the cE<sub>6</sub>SSM [107] found that the low energy gaugino masses are related to the universal gaugino mass  $M_{1/2}$  by the following approximate rules of thumb:  $M_1 \approx 0.15M_{1/2}$ ,  $M_2 \approx 0.25M_{1/2}$  and  $M_3 \approx 0.7M_{1/2}$ . Likewise in this study of the extended E<sub>6</sub>SSM, as expected from the RG running,  $M_1$  is approximately given by  $0.16M_{1/2}$  while  $M_2 \approx 0.28M_{1/2}$  and  $M_3 \approx 0.74M_{1/2}$ . By comparison, the corresponding gaugino values in the constrained MSSM are given by  $M_1 \approx 0.4M_{1/2}$ ,  $M_2 \approx 0.8M_{1/2}$  and  $M_3 \approx 2.7M_{1/2}$ . Compared to the cMSSM, the E<sub>6</sub>SSM predicts much lighter gluinos (but also heavier squarks). This must be taken into account when comparing  $(m_0, M_{1/2})$  charts between the cMSSM and the E<sub>6</sub>SSM - a given gluino mass corresponds to an E<sub>6</sub>SSM  $M_{1/2}$  value that is roughly 3.5 times smaller than its equivalent  $M_{1/2}$  in the cMSSM, and an  $m_0$  value that is about 1.5 bigger [107]. The latest  $m_0$ - $M_{1/2}$  mSUGRA/cMSSM plot from ATLAS at 8 TeV sets a lower bound on gluino masses of 1400 GeV for  $m_0 > 2000$  GeV [126]. Translated to the cE<sub>6</sub>SSM, this bound holds for  $m_0$  greater than roughly 3.5 TeV. This will be applied as an approximate lower bound to potential benchmark points from these scans. The spectrum of gluino masses  $m_{\tilde{g}}$  plotted against  $m_0$  and  $M_{1/2}$  is shown in Fig. 8.5. The lower purple section is the only part ruled out by experimental constraints. The fake likelihood imposed on the MultiNest sampling algorithm ensures that it is also extremely easy to find a variety of scenarios above  $m_0 = 3.5$  TeV satisfying the Higgs mass and relic density constraints (see Fig. 8.6).

The first and second generation squark masses  $m_{\tilde{d}L}$ ,  $m_{\tilde{u}L}$ ,  $m_{\tilde{d}R}$  and  $m_{\tilde{u}R}$  are given by:

$$m_{\tilde{d}L} = m_{Q_2} + \left( -\frac{1}{2} + \frac{1}{2}\sin^2\theta_W \right) m_Z^2 \cos^2\beta + \frac{1}{10}M_{Z'}^2, \quad (8.2)$$

$$m_{\tilde{u}L} = m_{Q_2} + \left( \frac{1}{2} - \frac{2}{3}\sin^2\theta_W \right) m_Z^2 + \frac{1}{10}M_{Z'}^2, \quad (8.3)$$

$$m_{\tilde{d}R} = m_{U_2} + \frac{2}{3}m_Z^2 \sin^2\theta_W \cos^2\beta + \frac{1}{2}M_{Z'}^2, \quad (8.4)$$

$$m_{\tilde{u}R} = m_{D_2} - \frac{1}{3}m_Z^2 \sin^2\theta_W \cos^2\beta + \frac{2}{10}M_{Z'}^2. \quad (8.5)$$

These masses tend to be extremely heavy. Fig 8.7 demonstrates this for  $m_{\tilde{u}L}$ . The masses of the top and bottom squarks are significantly lower, but still mostly beyond 13 TeV (see Fig. 8.8, which plots  $m_{\tilde{t}_1}$ ).

Fig. 8.9 and Fig. 8.10 plot  $s$  and  $\lambda$  against maximum binned values of the first generation squark mass  $m_{\tilde{u}L}$  and the third generation squarks  $m_{\tilde{b}_1}$ , respectively. For  $s > 20$  TeV,

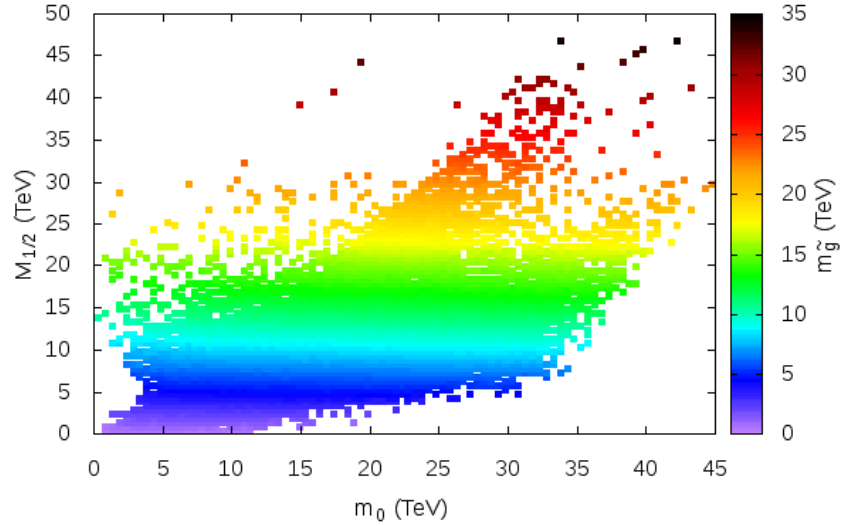


**Figure 8.5:** Maximum gluino masses plotted against  $m_0$  and  $M_{1/2}$ .  $m_{\tilde{g}}$  has a linear dependence on  $M_{1/2}$ .

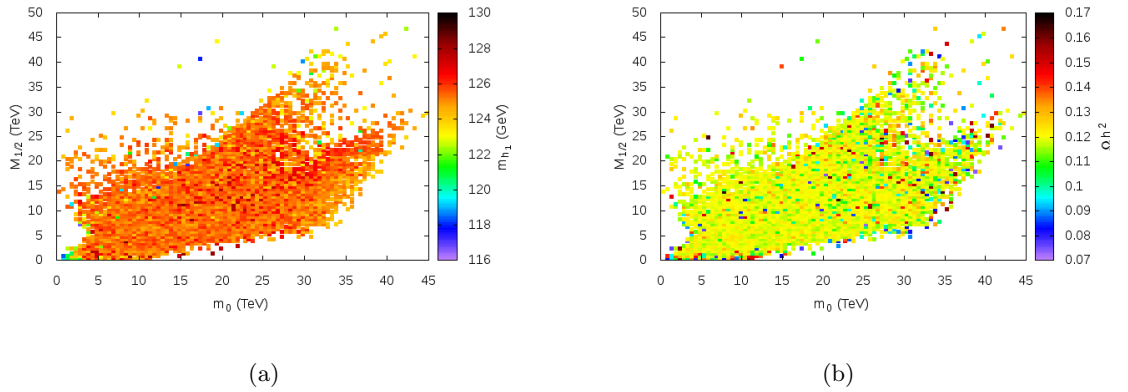


**Figure 8.6:** Binned values of the Higgs mass and relic density closest to 125.3 GeV and 0.1196 respectively, plotted against  $m_0$  and  $M_{1/2}$ .

the vast majority of squark masses are so heavy that they are well beyond detectability in the current run of the LHC. For instance, the greatest stop and sbottom masses reach an upper limit of roughly 80 TeV for higher values of  $s$ . The first and second generation squarks tend to reach slightly higher masses than equivalent values of the stop and sbottom squarks for each point in parameter space.

This is a rather different scenario from quarks in the standard model, in which the

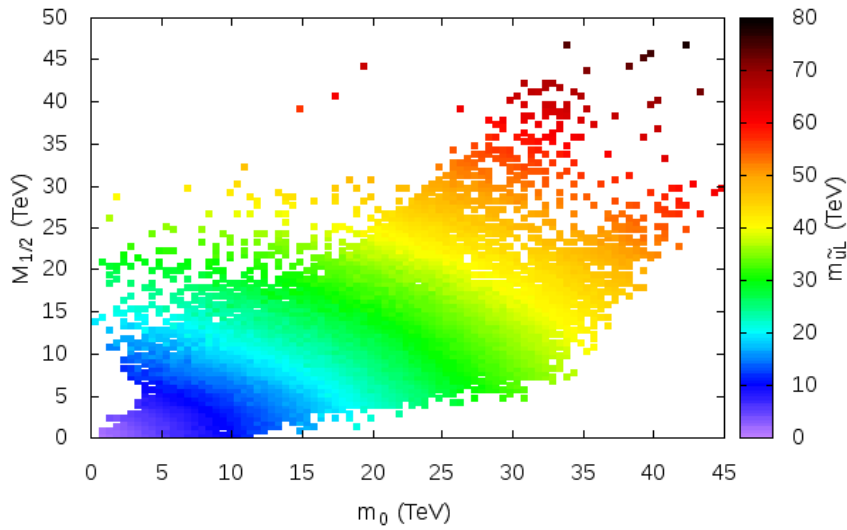


**Figure 8.7:** Binned maximum values of  $m_{\tilde{u}_L}$  plotted against  $m_0$  and  $M_{1/2}$ . These are mostly well beyond the scope of the LHC.

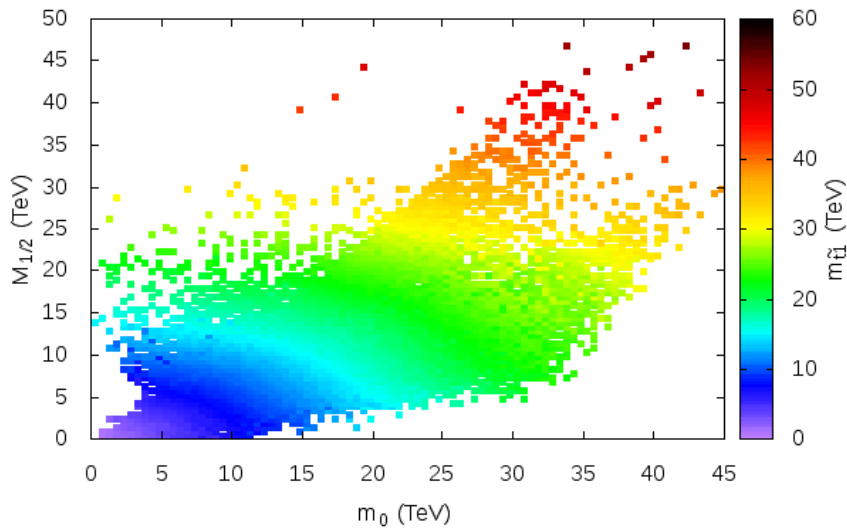


**Figure 8.8:** Binned maximum values of  $m_{\tilde{u}_1}$  plotted against  $m_0$  and  $M_{1/2}$ . These are smaller than the first and second generation squark masses, but are still mostly beyond the scope of the LHC.

third generation of quarks exists at a much higher mass scale than the first and second generations. In the constrained  $E_6$ SSM, similarly to the CMSSM, the discrepancy in

masses between squark generations arises during the RG evolution of each parameter, with the large third generation Yukawa coupling (particularly that of the top quark) resulting in a reduction of the stop and sbottom masses.

However, Athron et al. [132] noted that there may be substantial variation in squark masses even for given values of  $s$ , since even though the upper limits of  $M_{1/2}$  and  $m_0$  are dependent on  $s$ , low values of  $M_{1/2}$  are possible even for high values of  $s$ . It is possible to pick points out in our scan that demonstrate this fact - a heat map with the minimum  $m_{\tilde{b}_1}$  masses binned on the  $z$ -axis is shown in Fig. 8.11.

Although the minimum value of the squark masses also generally increases with  $s$ , squark mass values of 10-15 TeV or lower are still common for  $s$  up to 60 TeV (some points on the maximum binning plot reached up to 50 TeV for the equivalent  $s$  value).

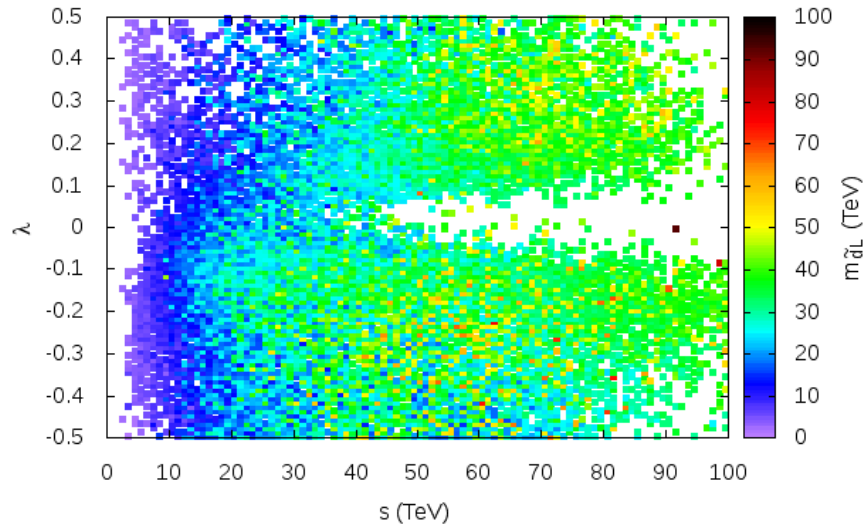


**Figure 8.9:** Maximum binned values of the left-hand first generation squark masses plotted against  $\lambda$  and  $s$ . Plots of the other first and second generation squarks,  $m_{\tilde{d}_r}$ ,  $m_{\tilde{u}_l}$  and  $m_{\tilde{u}_r}$ , look extremely similar, so for the sake of brevity only one plot has been printed. The majority of points sampled are not only well above established lower bounds on the squark masses, but also beyond being detected in current runs of the LHC, particularly for  $s > 20$  TeV.

An additional constraint is the mass of the  $Z'$  gauge boson. How well each point fits the  $Z'$  mass constraint is determined by the value of the singlet vacuum expectation value

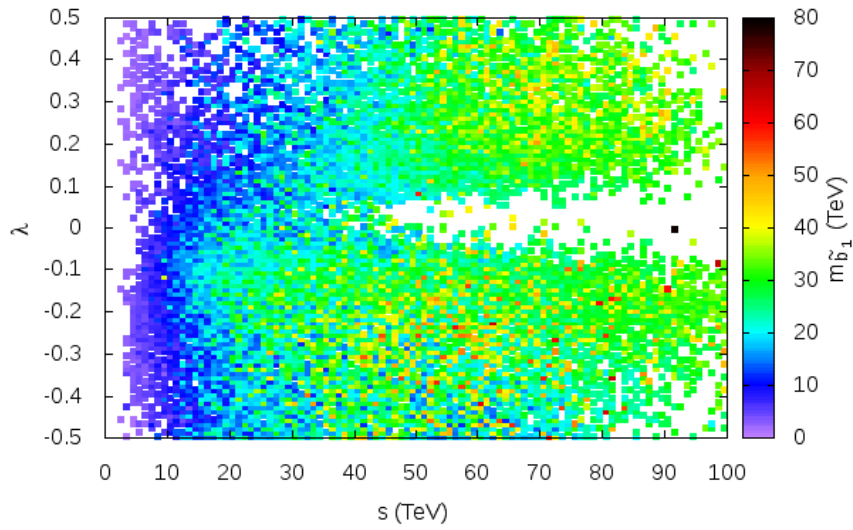


**Figure 8.10:** Maximum binned samples of the third generation squark mass  $m_{\tilde{b}_1}$  plotted against  $\lambda$  and  $s$ . As in the case of the first and second generation squarks, the majority of points sampled are well above LHC limits and detectability.

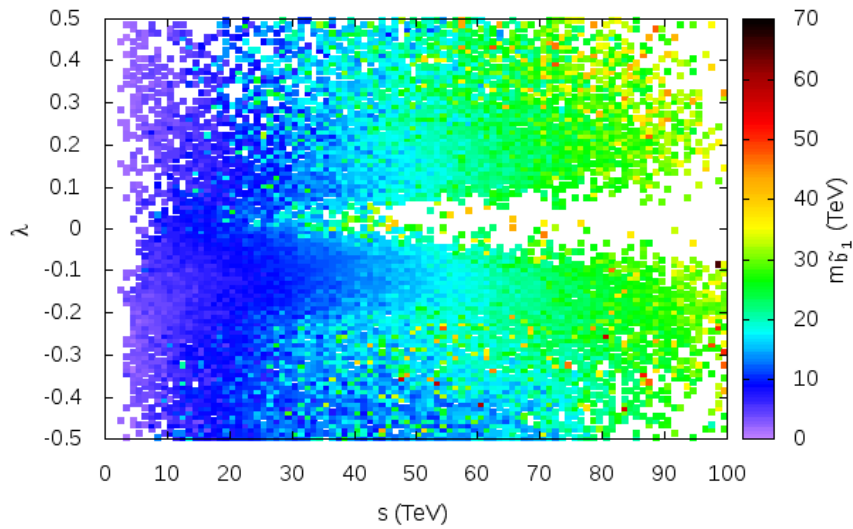


**Figure 8.11:** Plotting minimum binned values of  $m_{\tilde{b}_1}$ , demonstrating the range of squark masses that may be obtained for a given value of  $s$ .

$s$ , since for  $s \gg v$ :

$$M_{Z'} \approx g'_1 \bar{Q}_s s, \quad (8.6)$$

where  $\bar{Q}_s$  (the  $U(1)_N$  charge of  $S$ ) equals  $\frac{5}{\sqrt{40}}$  and  $g'_1$  (the low energy  $U(1)_N$  gauge coupling) is approximately 0.47. Hence,  $M_{Z'} \approx 0.37s$ . Since we can place a lower bound on  $M_{Z'}$  of approximately 2.85 TeV (with 95% confidence) [116], this means that  $s$  must take values greater than roughly 7.7 TeV (with the same level of confidence) for each point to be considered a benchmark. The majority of  $s$  values obtained in this scan exceed this by a clear margin. The full spread of  $m_{Z'}$  values obtained is shown in Fig. 8.12; the majority exceed limits on  $M_{Z'}$  by a wide margin, demonstrating that just as in the case of gluinos, values of  $m_0$  and  $M_{1/2}$  exceeding around 3.5 TeV yield mass parameters beyond experimental constraints.

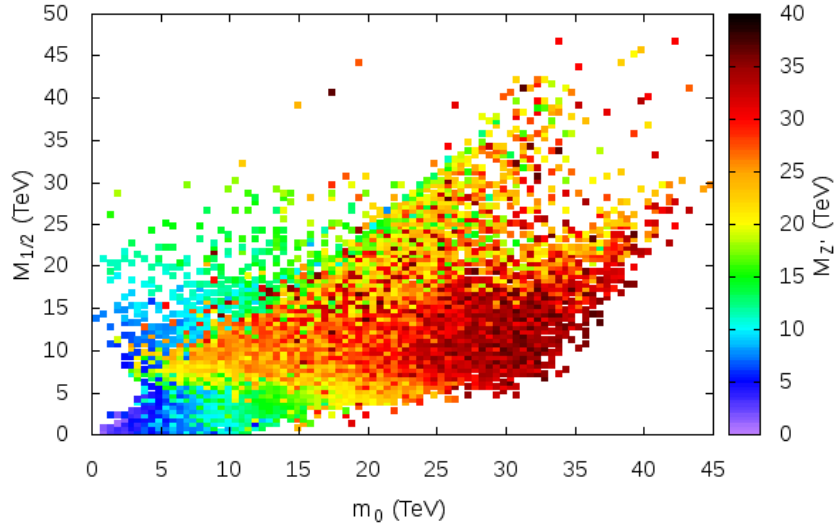


**Figure 8.12:** Binned maximum values of  $M_{Z'}$  plotted against  $m_0$  and  $M_{1/2}$ .

Numerous lower bounds on neutralinos and charginos have been estimated from collider experiments. LEP II set a lower bound on charginos of 100 GeV with a 95% confidence limit [127]. Although neutralino masses lower than 50 GeV are of great phenomenological interest [131], the masses of the lightest neutralinos of our model are of the same order of magnitude as that of the lightest chargino, so the LEP limit effectively rules out low mass

neutralinos as well.

### 8.3 Neutralino content mixing and masses

In the EZSSM with two decoupled inert singlinos, there are ten contributing fields to the lightest neutralino mass: bino ( $\tilde{B}$ ), wino ( $\tilde{W}$ ), two Higgsinos ( $\tilde{H}_u, \tilde{H}_d$ ), singlino ( $\tilde{S}$ ),  $U'(1)$  field ( $\tilde{B}'$ ) and four exotic inert Higgsinos ( $\tilde{H}_{u1}, \tilde{H}_{u2}, \tilde{H}_{d1}, \tilde{H}_{d2}$ ). The degree to which each field contributes to the neutralino content is denoted by  $|Z(N)_{1i}|^2$  ( $i = 1, \dots, 10$ ), and is dependent upon the variables in each column of the neutralino mixing angle matrix.

This study was motivated in part to consider scenarios such as those in [108] but with more Higgsino and exotic inert Higgsino content contributing to the lightest neutralino. The bino-like benchmarks of [108] have been ruled out by experimental constraints, but in this scan we have uncovered not only a number of potential WIMP candidates with bino-like properties, but also candidates with dominant Higgsino and inert Higgsino contributions.

Fig. 8.13 and Fig. 8.14 display heat maps of  $m_0$  and  $M_{1/2}$ , with the maximum binned neutralino mixing content displayed as colour heat maps. The subplots of Fig. 8.13 show the contributions of  $\tilde{B}$ ,  $\tilde{W}$ ,  $\tilde{H}_d$ ,  $\tilde{H}_u$ ,  $\tilde{S}$  and  $\tilde{B}'$  content respectively, while the subplots of Fig. 8.14 show the contributions of  $\tilde{H}_{d1}$ ,  $\tilde{H}_{d2}$ ,  $\tilde{H}_{u1}$  and  $\tilde{H}_{u2}$  content respectively. For small values of  $M_{1/2}$ , there are regions in which the neutralino is near-entirely bino-like. For  $M_{1/2}$  above 5 TeV, the content becomes less heavily dominated by binos and more by Higgsinos and inert Higgsinos. Winos, singlinos and the  $\tilde{B}'$  field contribute very little to the neutralino content.

The masses and mixing angles of the neutralinos are determined by only a few variables:  $M_{1/2}$ ,  $\tan\beta$ ,  $s$  and the  $x_{u/d/1/2}$  and  $\lambda_{11/22}$  terms. Thus, we find that bino-like and wino-like contributions are heavily dependent on the value of  $M_{1/2}$  (the lower  $M_{1/2}$ , the greater the bino and wino content).

For greater values of  $M_{1/2}$ , Higgsino-like and inert Higgsino-like neutralinos become dominant (see Fig. 8.13); for  $M_{1/2} > 6 \times 10^3$  GeV, the WIMP dark matter has almost no bino content. This is due to the fact that  $M_{1/2}$  determines the mass of both the bino and the wino, with winos tending to be heavier. If  $M_{1/2}$  is increased, so do the bino and wino masses, and thus the LSP will be more likely to be Higgsino and inert Higgsino dominated

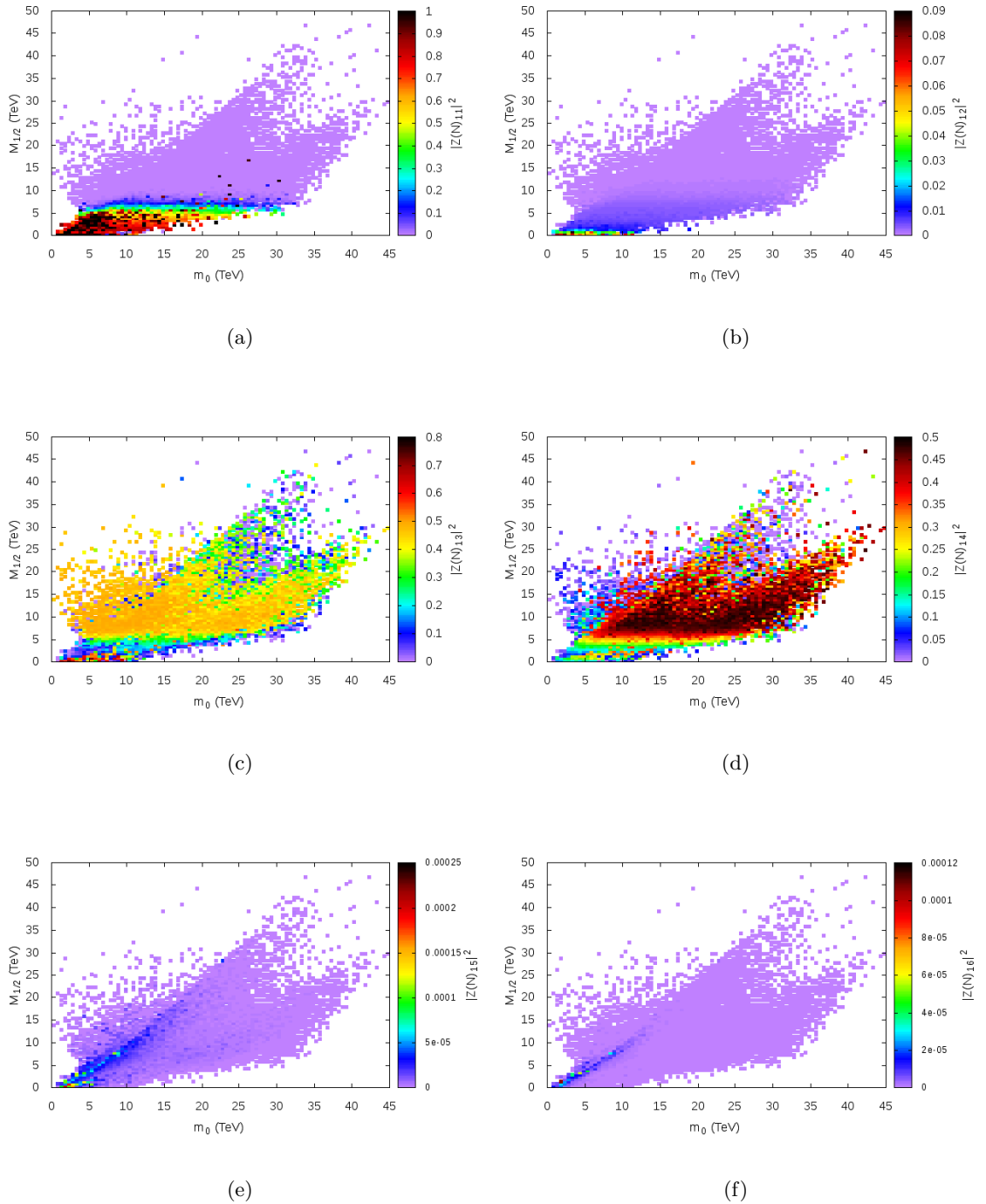


**Figure 8.13:** Maximum binned plots of the neutralino mixing content: (a) shows bino content; (b) shows wino content; (c) and (d) show Higgsino content; (e) shows singlino content; (f) shows  $\tilde{B}'(1)$  content.

(with the heavier neutralinos being made up mostly of winos and binos). As subfigures Fig. 8.13(e) and Fig. 8.13(f) demonstrate, there is very little singlino and  $U'(1)$  content. This is the consequence of singlino masses being set by the  $Z'$  mass and consequently being

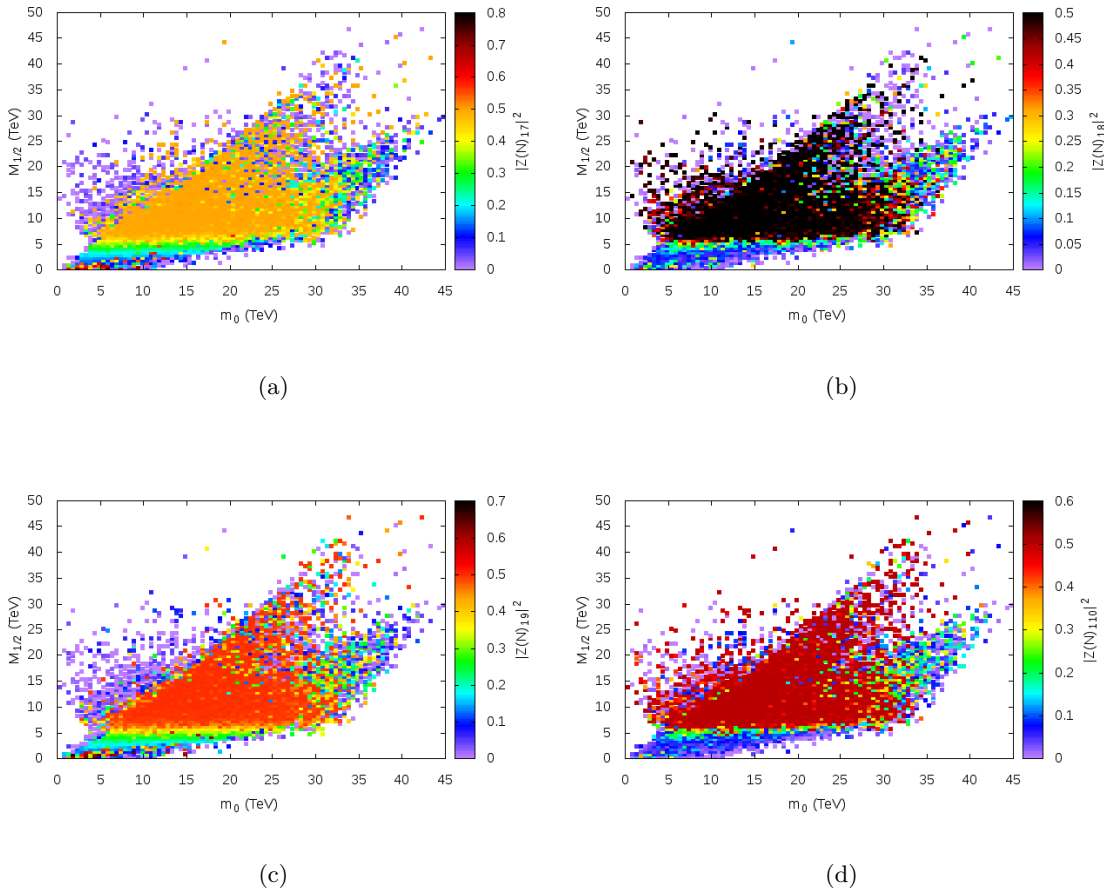


**Figure 8.14:** Maximum binned plots of the inert Higgsino content.

too heavy for representation in the content of the LSP. Thus, the greatest contributions for the lightest neutralino content will stem from binos, Higgsinos and inert Higgsinos, with the exact proportion of each depending on  $M_{1/2}$ .

Whether Higgsinos contribute more than the inert Higgsinos depends upon the values of their respective columns in the neutralino mixing matrix (such as the  $l_{11}$  and  $l_{22}$  terms in the  $4 \times 4$  submatrix in the bottom-right corner, which heavily determine the proportion of inert Higgsino). For both  $\lambda_{11}$  and  $\lambda_{22}$ , Fig. 8.15(a) and Fig. 8.15(b) demonstrate that there are two distinct regions in which the neutralino content is heavily dominated by inert Higgsinos,  $\lambda_{11/22} \approx 0.1$  and  $\lambda_{11/22} \approx 0.8$  (separately, as Fig. 8.16 shows). Higher gluino masses are also correlated with increased inert Higgsino content (with  $l_{11}$  and  $l_{22}$  clustered at  $< 0.1$  and  $0.8$ ).

Fig. 8.18(a), Fig. 8.18(b) and Fig. 8.18(c) show the spread of SI cross sections for bino,

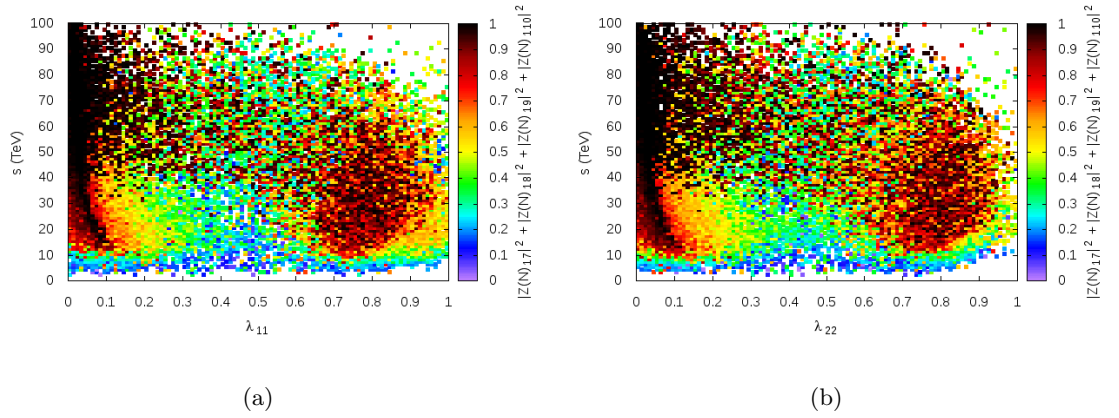


**Figure 8.15:** Maximum binned plots of the inert Higgsino content, showing its correlation with  $\lambda_{11}$ ,  $\lambda_{22}$  and  $s$ .

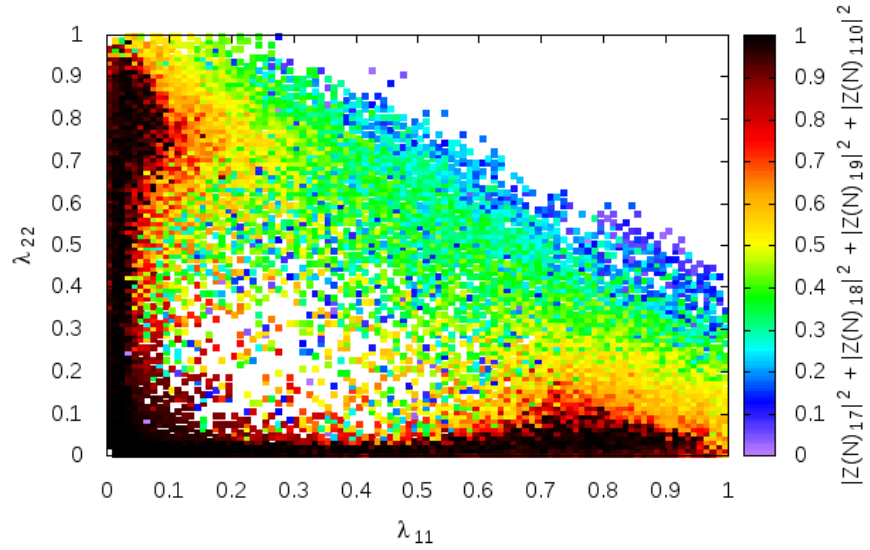


**Figure 8.16:** Maximum binned plots of the inert Higgsino content, showing its correlation with  $\lambda_{11}$  and  $\lambda_{22}$  together.

Higgsino and inert Higgsino neutralino content respectively. The very highest, most easily detected cross sections (potentially ruled out by LUX exclusions) are skewed in favour of higher bino and Higgsino content, although there is a sharp spike in frequency for points containing almost entirely inert Higgsino content (Fig. 8.17(a) and Fig. 8.17(b)).

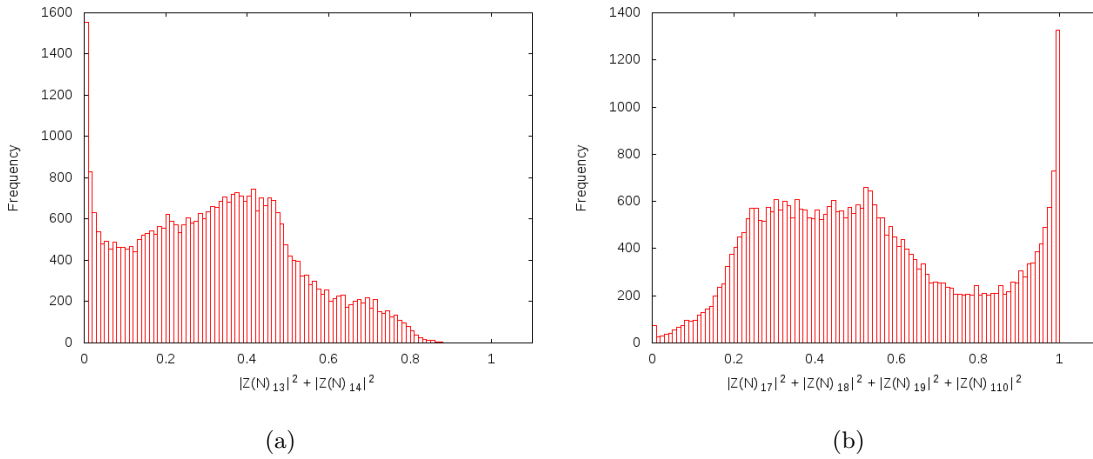


**Figure 8.17:** The frequency of sampled points containing Higgsino and inert Higgsino content respectively on a scale between 0 (no Higgsino content) and 1 (full Higgsino content).

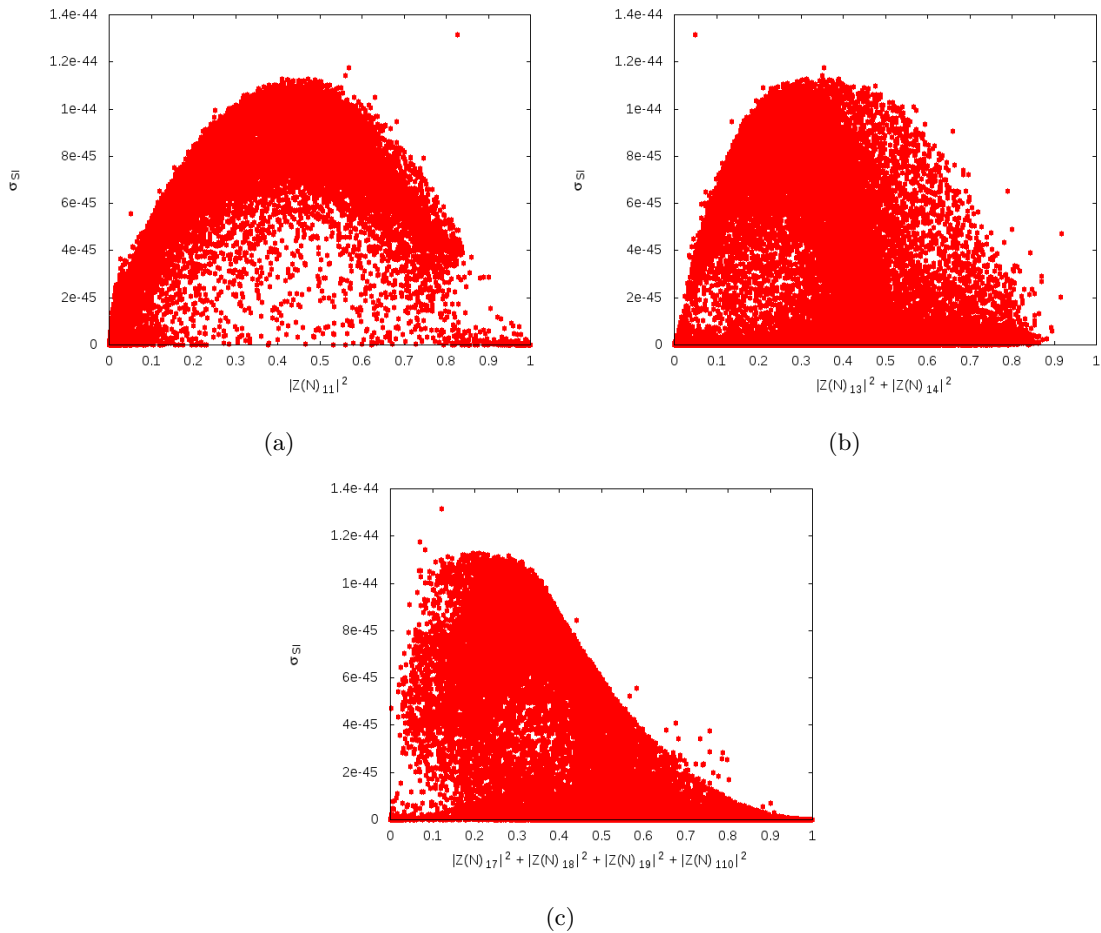


**Figure 8.18:** The SI cross section plotted against bino, Higgsino and inert Higgsino content respectively. This cross section tends to be largest with an admixture of bino and Higgsino content in the lightest neutralino.

## 8.4 Colour contours of SI cross sections

We must check for regions with sufficiently high neutralino-nucleon cross sections that are within reach of current detection according to LHC exclusions, compared with regions with cross sections that are high enough for detection in the near future yet still beyond the scope of current collider detection efforts. The couplings between Higgsinos and singlinos ( $x_{u1}$ ,  $x_{u2}$ ,  $x_{d1}$ ,  $x_{d2}$ ,  $\lambda_{11}$  and  $\lambda_{22}$ ) are displayed in Fig. 8.19.

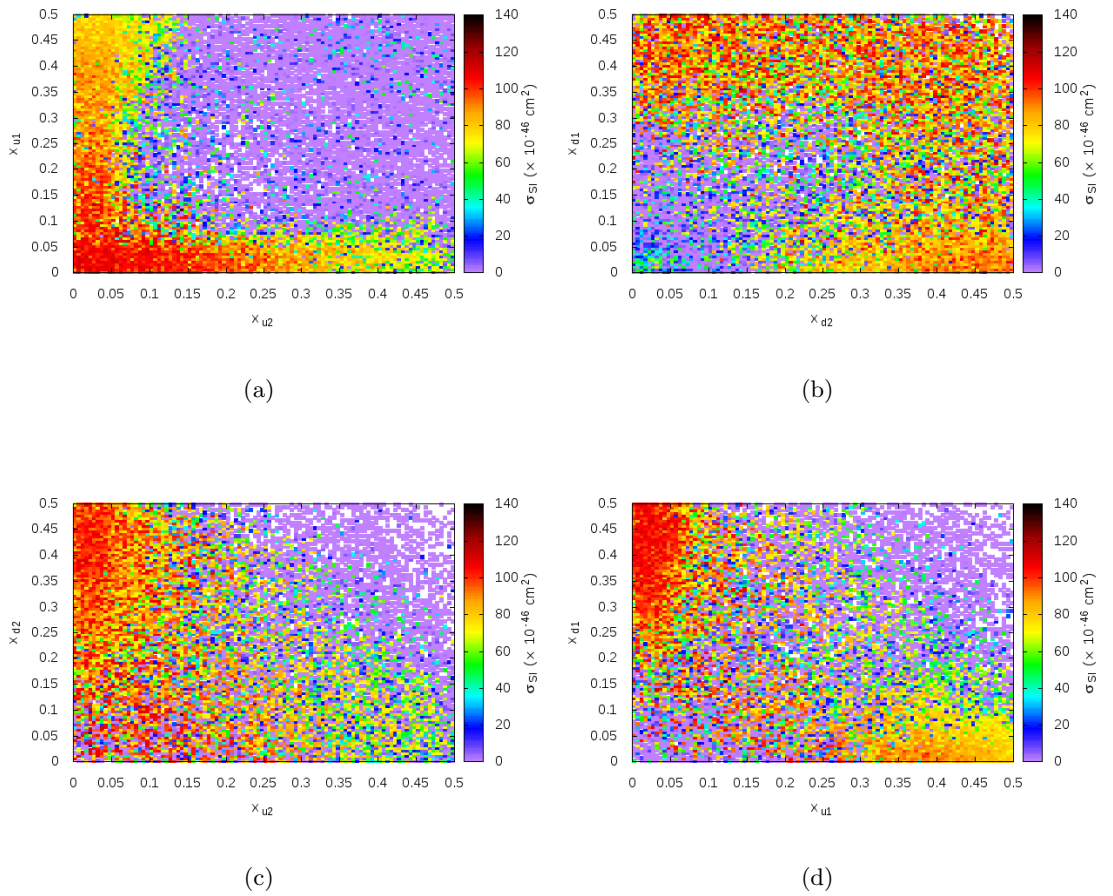


**Figure 8.19:** Maximum binned plots of the SI cross section from sweeps across  $x_{u2}$ ,  $x_{u1}$ ,  $x_{d2}$  and  $x_{d1}$ , with other parameters free to vary.

With ten freely varying parameters, the cross section is relatively weakly dependent on any given “ $x$ ” plane, as the scattered plots of Fig. 8.19 demonstrate. Generally, greater cross sections tend to be obtained for lower values of  $x_{u2}$  and  $x_{u1}$  and higher values of  $x_{d2}$  and  $x_{d1}$ . Fixing  $\sigma_S$  above  $60 \times 10^{-46} \text{ cm}^2$  makes these tendencies clearer (see Fig. 8.20).

Taking one particular variable (for instance,  $x_{u1}$ ) and plotting it against the neutralino

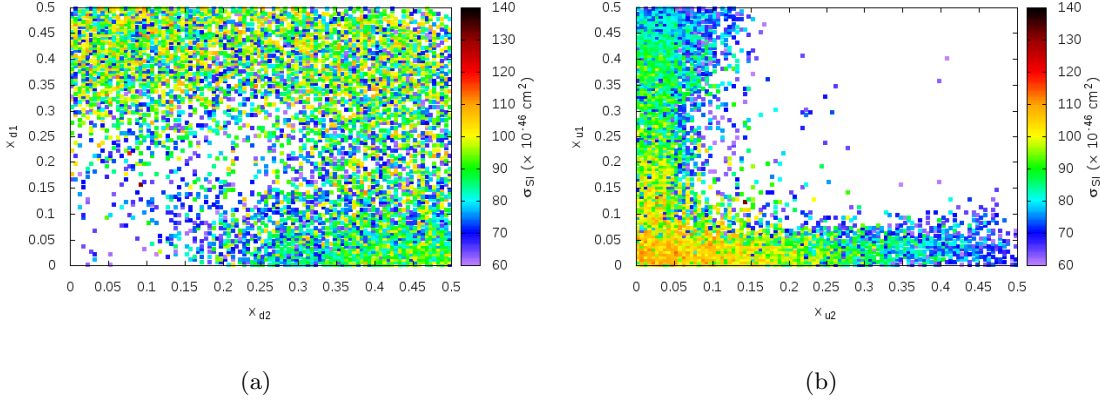


**Figure 8.20:** Repeating plots with the maximum binned  $\sigma_{SI}$  limited to lie above  $6 \times 10^{-45} \text{ cm}^2$ , demonstrating more clearly that larger cross sections tend to be found for higher values of  $x_{d1}$  and  $x_{d2}$  and lower values of  $x_{u1}$  and  $x_{u2}$ .

mass with the SI cross section as a heat map value enables us to spot the regions within detectability according to LUX limits. Fig. 8.22 shows that for a neutralino with mass between 400 GeV and 1 TeV, there is a distinct region between  $x_{u1} = 0$  and  $x_{u1} = 0.1$  in which cross sections reach levels above  $1 \times 10^{-44} \text{ cm}^2$ , well within the reach of current detection experiments.

As we can see in Fig. 8.21 and Fig. 8.23, similar correlation strengths are observed for  $\lambda_{11}$  and  $\lambda_{22}$  planes, with higher cross sections tending to cluster at higher values of either  $\lambda_{11}$  or  $\lambda_{22}$  - but not both simultaneously, as Fig. 8.24 shows. If both  $\lambda_{11}$  and  $\lambda_{22}$  approach 1, typically either the resultant Higgs mass or relic density lies outside of acceptable bounds, or the spectrum generator’s output becomes non-perturbative. This is due to the fact that the RGEs for the Yukawa couplings contain positive and negative contributions from the Yukawas and gauge couplings respectively. Increasing the former (as happens when both  $\lambda_{11}$  and  $\lambda_{22}$  are significantly boosted) may result in a Landau pole.

How favourable are these points in the context of our constructed “likelihood” using the LUX limit, Higgs mass and relic density? Fig. 8.25 plots  $\lambda_{11}$  and  $\lambda_{22}$  against the likelihood function of Eq. 8.1, demonstrating that these regions ( $\lambda_{11}$  or  $\lambda_{22}$  close to 0.8,  $\lambda_{11}$  or  $\lambda_{22}$  close to 0) generally coincide with the areas of greatest likelihood.

Fig. 8.26 demonstrates that the spin-independent cross section is heavily dependent on the unified soft gaugino mass  $M_{1/2}$ . A narrow band of  $M_{1/2}$  values up to 9 TeV are favoured

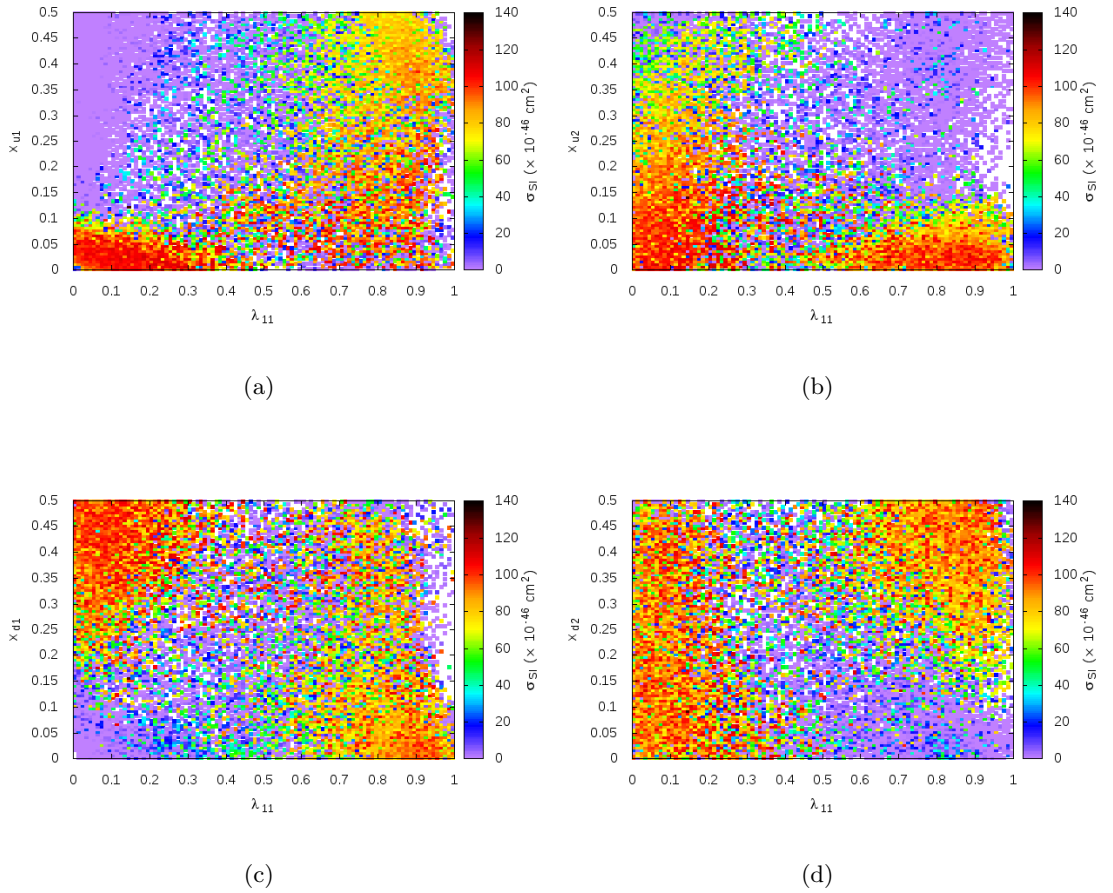


**Figure 8.21:** Maximum binned plots of the SI cross section from sweeps across  $\lambda_{11}$ , with other parameters free to vary.

for cross sections above  $20 \times 10^{-46} \text{ cm}^2$ , with the highest cross sections found between 3 and 7 TeV. These are well above the latest LHC exclusion limits of most supersymmetric models.

[105] found that lower  $M_{1/2}$  is weakly correlated with lower  $s$  and lower  $Z'$  masses; we similarly expect that higher cross sections are also obtained for the lower end of the  $s$  spread, and indeed this is the case as Fig. 8.27 shows.

When the unified trilinear coupling  $A_0$  is plotted against  $\mu_{\text{eff}} = \frac{\lambda s}{\sqrt{2}}$ , three distinct regions emerge, with high cross sections heavily corresponding to low values of  $\mu_{\text{eff}}$  (Fig. 8.28). This is not a particularly surprising result. We have already seen that lower values of  $s$  correspond to higher cross sections; plotting  $\lambda$  against  $x_{u1}$  (Fig. 8.29) demonstrates that lower values of  $\lambda$  are also correlated with higher cross sections, with a cluster centred on  $\lambda = -0.1$  being particularly prominent.

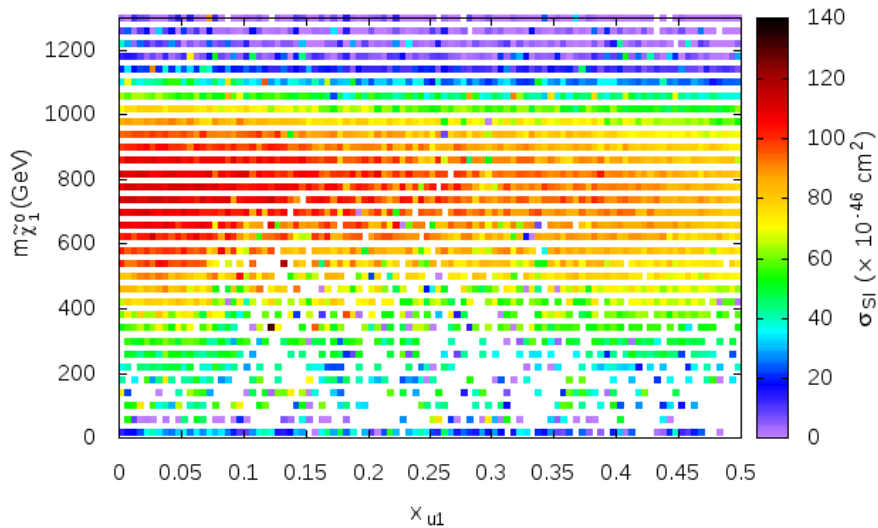


**Figure 8.22:** Plotting maximum binned values of the SI cross section against  $x_{u1}$  and  $m_{\tilde{\chi}_1^0}$ .

By plotting  $A_0$  alone against the neutralino mass with spin-independent cross section again plotted as a heat map, the regions within experimental detectability according to LUX can be made more apparent (see Fig. 8.30). Between  $A_0 = -10$  TeV and  $A_0 = 20$  TeV and  $m_{\tilde{\chi}_1^0}$  between 600 GeV and 900 GeV, the maximum obtainable cross section is extraordinarily high.

## 8.5 Benchmark points and discussion

The previous sections of this chapter have highlighted regions of the  $E_6$ SSM parameter space that are now within current experimental reach, in addition to areas with rich features with reasonably high cross sections for detection in the near future. The aim of this final section is to lay out a number of benchmark points close to the LUX exclusion limit, including different neutralino content. Of particular interest are benchmark points with neutralinos made up of significantly high inert Higgsino content, since these feature only in  $E_6$ SSM models with extended mixing matrices and thus aren't present in the  $cE_6$ SSM.

Firstly, what are the parameter ranges that have been shown to yield areas with high

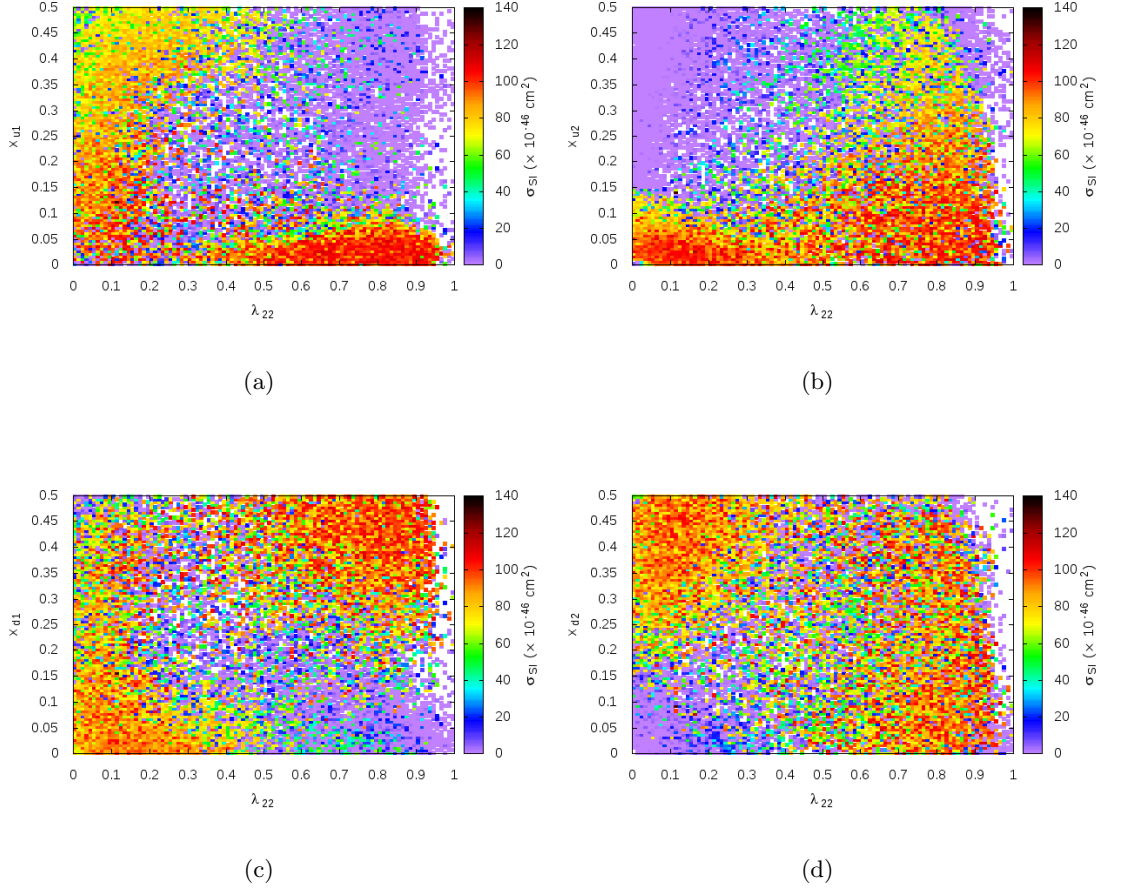


**Figure 8.23:** Maximum binned plots of the SI cross section from sweeps across  $\lambda_{22}$ , with other parameters free to vary.

potential SI cross sections? Based on Fig. 8.26,  $M_{1/2}$  should ideally fall under 9 TeV. For these values,  $m_0$  ranges from approximately 3.5 up to 30 TeV. The value of  $\tan\beta$  may take any value between 5 and 40 while still yielding a high cross section.  $\lambda$  tends to range between -0.2 and 0.2. The trilinear  $A_0$  yields high cross sections between approximately -10 TeV and 20 TeV.  $\mu_{\text{eff}}$  ranges between -0.5 and 0.5. As explained earlier, since the mass of the  $Z'$  boson is limited to values above 2.60 GeV,  $s$  must take values greater than 5.5 TeV.

Taking these constraints and regions of interest into account, twelve benchmark points have been selected based on their neutralino content (inert Higgsino, Higgsino, bino or a combination), displayed in Table 8.2 and Table 8.3. These points are consistent with all relevant data and represent phenomenologically viable scenarios. At the top of each column is the SI cross section and relic density, followed by four of the input parameters

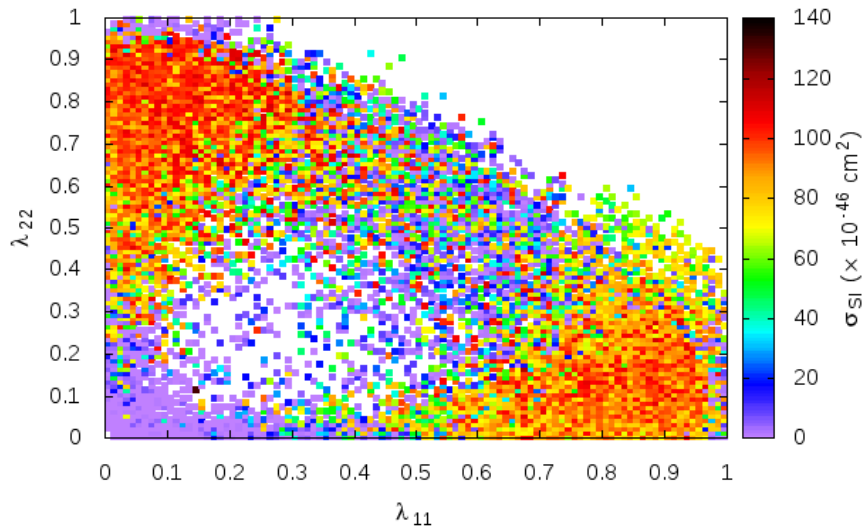


**Figure 8.24:** Maximum binned plot of the SI cross section, with  $\lambda_{11}$  and  $\lambda_{22}$  plotted against each other.

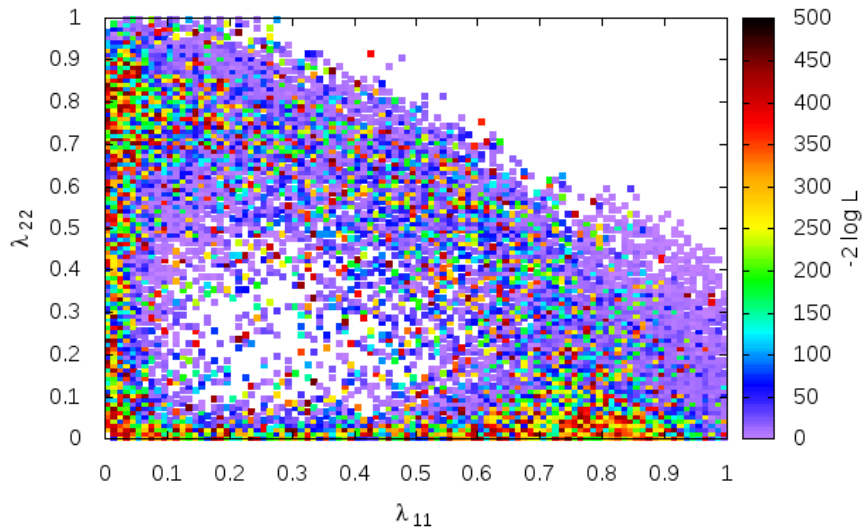


**Figure 8.25:** Mapping the maximum binned likelihood against  $\lambda_{11}$  and  $\lambda_{22}$ .

( $\lambda$ ,  $\tan\beta$ ,  $\kappa$  and  $s$ ). The mass spectrum follows next, including the mass of the lightest neutralino, the lightest Higgs, the universal scalar and gaugino masses  $m_0$  and  $M_{1/2}$ , the

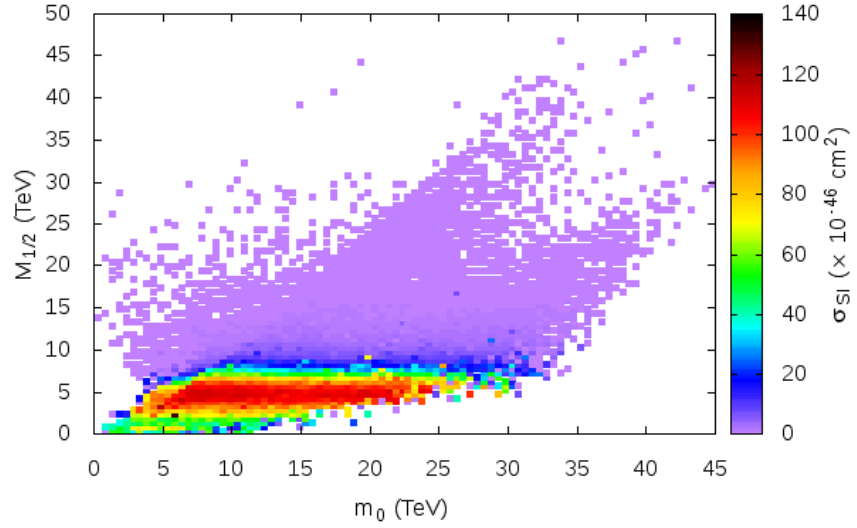


**Figure 8.26:** The maximum binned value of SI cross section plotted against  $m_0$  and  $M_{1/2}$ . A narrow band of  $M_{1/2}$  values up to 9 TeV are favoured for cross sections above  $20 \times 10^{-46} \text{ cm}^2$ , with the highest cross sections found between 3 and 7 TeV.

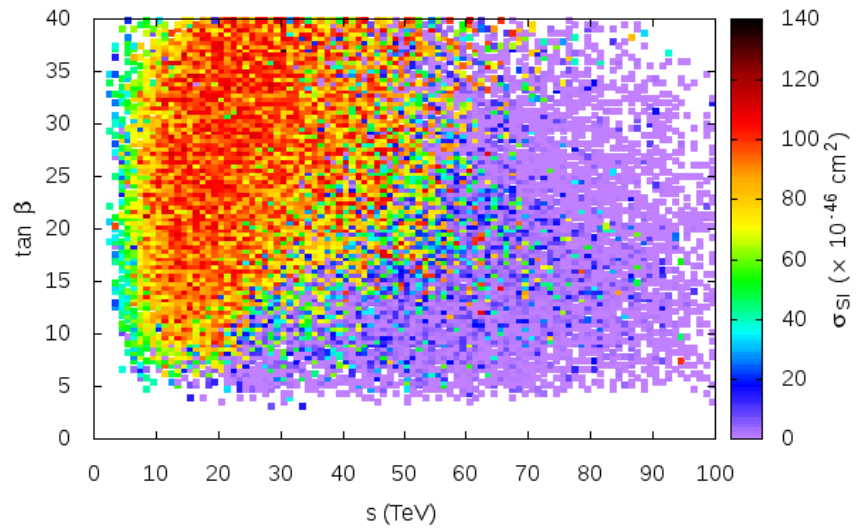


**Figure 8.27:** Maximum binned  $\sigma_{\text{SI}}$  plotted against  $s$  and  $\tan \beta$ .

exotic quarks (which are leptoquarks or diquarks), the first and second generation inert Higgsinos ( $\mu_{\tilde{H}_1}$  and  $\mu_{\tilde{H}_2}$ ), the gauginos, three of the squarks ( $m_{\tilde{t}_1}$ ,  $m_{\tilde{b}_1}$  and  $m_{\tilde{u}_L}$ ), and  $Z'$

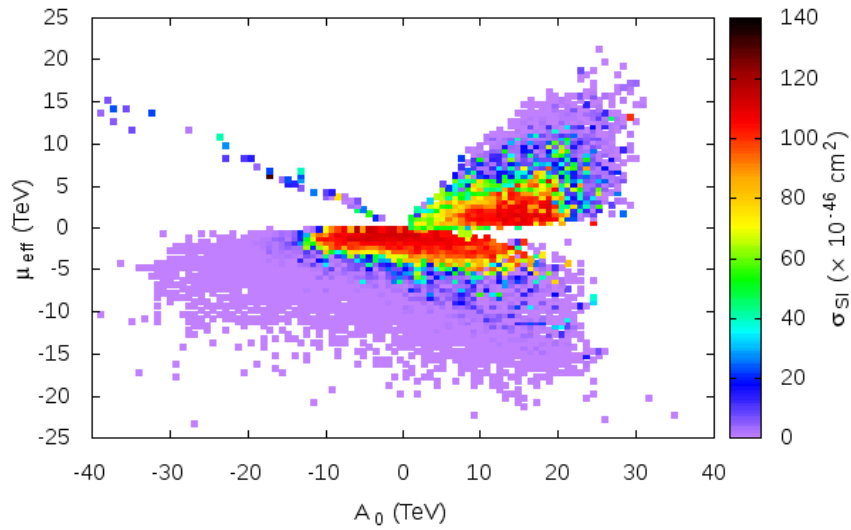


**Figure 8.28:**  $\mu_{\text{eff}}$  vs  $A_0$ . High cross sections heavily correspond to low values of  $\mu_{\text{eff}}$ .

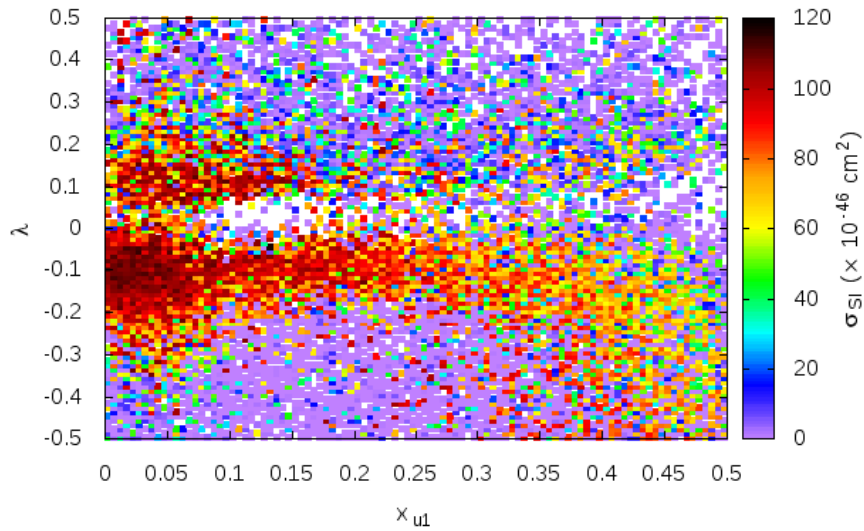


**Figure 8.29:**  $\lambda$  vs  $x_{u1}$ . High cross sections correspond with lower values of  $\lambda$ .

( $M_{Z'}$ ). The trilinears  $A_0$  and  $A_\lambda$  follow afterwards and finally the benchmark columns are rounded off with the content of the lightest neutralino.

In Fig. 8.31, each of these benchmark points are plotted against the LUX exclusion

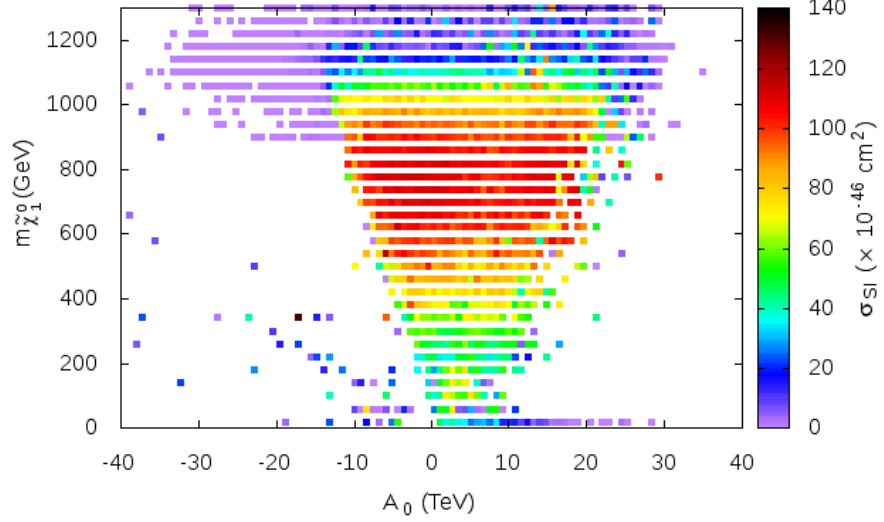


**Figure 8.30:** Plotting the  $A_0$  trilinear alongside neutralino mass to ascertain regions that have been ruled out by LUX.

limit used in the MultiNest likelihood. Only **BM10** falls within the blue shaded  $\pm 1\sigma$  variation region. If we were to compare these with the updated LUX limit from December 2015, **BM3** and **BM9** also fall within the new  $\pm 1\sigma$  shaded region, but all benchmarks are yet to be ruled out.

As mentioned, the exotic quarks ( $D$ -quarks)  $\mu_{D_i}$  have also been added to the spectrum output. These masses are given by:

$$\mu_{D_i} = \frac{\kappa_i}{\sqrt{2}} s, \quad i = 1, 2, 3. \quad (8.7)$$

Since a universal  $\kappa$  has been used, these are the same for each generation. These leptoquarks or diquarks have odd R-parity, and so are produced in pairs and decay into an LSP. Their presence provides a new avenue of discovery and detection for these benchmarks, as hypothetical exotic quarks may be detected via their missing energy when they decay. The production of exotic leptoquark cross sections are comparable to top-quark pair production at the LHC, as demonstrated by Athron et al. [107]. These enhance the cross sections of the  $pp \rightarrow t\bar{t}\tau^+\tau^- + E_T^{miss} + X$  and  $pp \rightarrow b\bar{b}\tau^+\tau^- + E_T^{miss} + X$  decays ( $X$  representing light quark/gluon jets). If the exotic fermions are diquarks, they enhance the

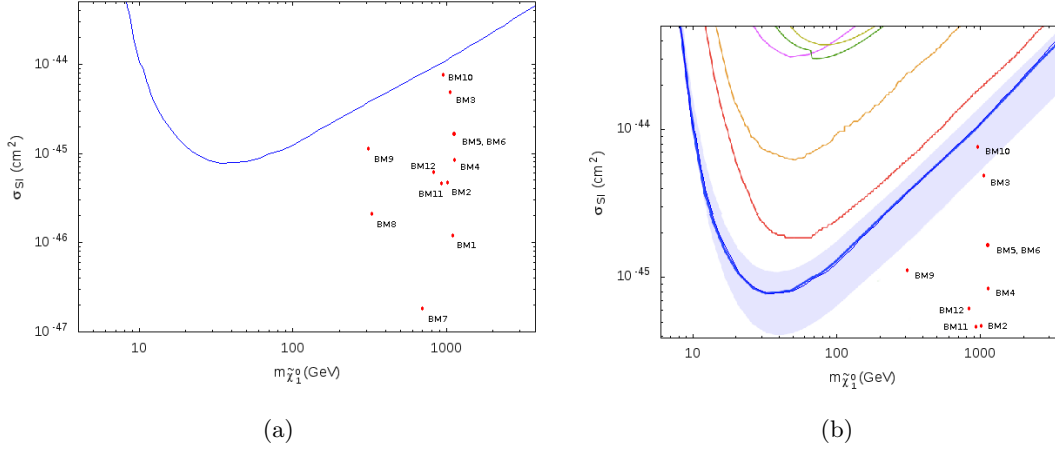


**Figure 8.31:** Benchmark points and the WIMP-nucleon SI cross section limit. (a) shows each of the ten benchmarks plotted relative to the LUX dark matter exclusion line used in these scans. (b) directly overlays this exclusion line and the ten benchmark points with the highest SI cross section over the LUX plot from [56]. Only **BM10** is in the blue exclusion region. Using updated figures from December 2015, **BM3** and **BM9** fall within the new blue region, but are still yet to be ruled out.

cross sections of  $pp \rightarrow t\bar{t}\bar{b}\bar{b} + E_T^{miss} + X$  and  $pp \rightarrow b\bar{b}\bar{b}\bar{b} + E_T^{miss} + X$ .

These  $D$ -fermion masses vary significantly between each of the following benchmark models, and they are not always light. Most of the heavier exotic quarks are not likely to be feasibly detected by the LHC at 13 TeV. However, **BM9** and **BM12** feature light exotic quark masses (702.2 GeV and 783.6 GeV, respectively), and thus have the best prospects for early discovery via exotic quark searches.

### 8.5.1 BM1 and BM2: inert Higgsino dark matter

Firstly, **BM1** is an inert Higgsino neutralino scenario with a SI cross section well below the current LUX limit for its WIMP mass (1104 GeV). Its relic density and Higgs mass (0.1190 and 124.8 GeV, respectively) place it in excellent agreement with the constraints on these values. Its high  $s$  value means that it yields a value of  $M_{Z'}$  that is not only well above the  $Z'$  limit, but also too high for detection at the LHC at 13 TeV. Its exotic quarks are also extremely heavy.

An attempt was made to find an inert Higgsino neutralino ( $> 90\%$ ) scenario with a cross section closer to the LUX limit and thus within the range of current detectability. However, although many such points exist, none yielded a Higgs mass and relic density that would make them suitable for a benchmark point. With the condition for inert

Higgsino content relaxed from 90% to 80%, more viable benchmark points were found, such as **BM2**. It is distinguished from **BM1** predominantly by having a cross section lying within the blue region below the LUX limit in Fig. 8.1, making it a point that could be detected in the near future. The parameter inputs  $\lambda$ ,  $\tan\beta$  and  $s$  are also very different from those of **BM1**, demonstrating that there is room to tune multiple parameters at once to achieve similar outcomes in terms of the light neutralino content. **BM2** features lower gluino and squark masses than **BM1**, but they are still well within LHC constraints. The second up-type inert Higgsino contributes more to the neutralino composition than **BM1**, which has large contributions from the two down-type inert Higgsinos. Like **BM2**, it has a heavy  $m_{Z'}$  which cannot be feasibly detected at the LHC in its current run.

### 8.5.2 BM3 and BM4: mixed Higgsino and inert Higgsino dark matter

Moving on from the overwhelmingly inert Higgsino benchmarks, **BM3** features a high contribution from the up-type Higgsino in addition to the reasonably large contribution from the inert Higgsinos (particularly the first generation up-type inert Higgsino). With a high SI cross section combined with a light neutralino mass of 1058 GeV, it lies close to the LUX upper exclusion limit and has high prospects for detection in the near-future. Its exotic  $D$ -quark mass is much lighter than those of **BM1** and **BM2**, but still reasonably heavy at 2.9 TeV.

**BM4** was chosen as a point that is in less danger of being ruled out, with a neutralino mass of 1123 GeV and SI cross section  $8.46 \times 10^{-46}$  cm<sup>2</sup>. It features a high Higgsino content to the lightest neutralino (just over 50%) with the rest mostly being made up of inert Higgsinos, making it a more equal admixture of Higgsino and inert Higgsino than **BM3**. Its exotic  $D$ -quark mass (1.57 TeV) is even lower than that of **BM3**, increasing its prospects for detection via exotic leptoquark and diquark searches.

### 8.5.3 BM5 and BM6: Higgsino dark matter

No suitable benchmark points with total active Higgsino content above 90%, with Higgs mass between 122.0 and 128.0 GeV and relic density between 0.1186 and 0.1206 could be found. Relaxing the condition for active Higgsino content to points about 80%, the next benchmark scenario is **BM5**, which with a neutralino mass of 1117 GeV and SI cross

section  $1.65 \times 10^{-45} \text{ cm}^2$  is on the cusp of detectability.

As with the previous benchmarks, a sister benchmark **BM6** with high Higgsino content was selected with a smaller cross section and lower chance of detectability at the LHC. It also differs from **BM5** by having a much larger  $Z'$  mass at 22 TeV, far too big for detection at the LHC in its current run. The exotic quarks of both these benchmarks are also extremely heavy, ruling them out for exotic quark searches.

#### 8.5.4 **BM7, BM8 and BM9: bino dark matter**

As in the constrained  $E_6$ SSM scenario, there are many points with high bino content. However, searching for points with bino content above 90% that fit the higgs mass and relic density requirements for a benchmark yielded relatively few with a high cross section. **BM7** is one of those few, with a neutralino mass 699.5 GeV and SI cross section  $1.85 \times 10^{-47} \text{ cm}^2$ , lower than the other benchmark points. Its cross section rules it out as a current direct detection candidate, but it notably has a relatively light first generation inert Higgsino mass of 172.9 GeV, making it an eligible point for detectability via exotics searches at the LHC.

Relaxing the bino content requirement to 80% yields points closer to the LUX detection limit, many with neutralino masses around 100-300 GeV. **BM8** was selected as a bino-like neutralino benchmark point on the edge of the LUX limit, while **BM9** lies slightly below it. **BM8** and **BM9** both feature a lighter neutralino mass than **BM7** (324.6 GeV and 307.6 GeV respectively). They also feature relatively low gluino and squark masses, increasing their prospects for detection at the LHC.

**BM8** and **BM9** are further differentiated from each other by their exotic masses, giving them different potential detection signals at a collider. **BM8** has a relatively light first generation inert Higgsino mass at 479.1 GeV, while **BM9** has a lighter exotic quark mass at 702.2 GeV.

#### 8.5.5 **BM10, BM11 and BM12: mixed bino, Higgsino and inert Higgsino dark matter**

Finally, some points with mixtures of bino, Higgsino and inert Higgsino contributing content were selected to round off the set of twelve benchmarks based on neutralino content.

**BM10** has the highest SI cross section and the best chance of direct detection at the LHC, lying within the blue exclusion region of the LUX curve in Fig. 8.1, while **BM11** and **BM12** lie well below it.

Furthermore, **BM12** (which has the highest bino content of these three mixed benchmarks) has the most eligibility for detection via exotic searches, as both its exotic quark and its first generation inert Higgsino lie below 1 TeV. It also features a lighter  $Z'$  mass at 4.4 TeV.

### 8.5.6 Light neutralino dark matter

Noticeably, each of these benchmarks has a neutralino mass that is relatively high (above 300 GeV), and most are around 1 TeV. How light can the lightest neutralino be? In the CMSSM parameter space, the Higgs and gluino mass limits result in a lower neutralino bound of 240 GeV [128]. In the extended  $E_6$ SSM parameter scan, it is possible to find points with lighter neutralino masses than this within the given constraints on Higgs mass and relic density. Three such scenarios are displayed in Table 8.4. They each have a negligibly small bino component, being predominantly composed of Higgsino and inert Higgsino. Their exotic quark masses are all very heavy. The third scenario features the lightest squark and gluino masses.

However, each of these scenarios are also accompanied by an unacceptably light chargino mass, being of the same approximate mass as the lightest neutralino. This therefore rules them out for future detection, and their inclusion in these results is for the sake of interest only.

## 8.6 Relic density discussion

Of course, we require that the lightest neutralino must account for the observed dark matter relic density. Reference [129] contains a discussion of neutralino relic density in the MSSM, including the contributions of co-annihilations (in which particle pairs, such as neutralinos and charginos, mutually annihilate). The particle density  $n$  evolves with

time as:

$$\frac{dn}{dt} = -\langle\sigma_{\text{eff}}v\rangle(n^2 - n_{\text{eq}}^2) - 3Hn, \quad (8.8)$$

$$\langle\sigma_{\text{eff}}v\rangle = \sum_{ij} \langle\sigma_{ij}v_{ij}\rangle \frac{n_i^{\text{eq}} n_j^{\text{eq}}}{n^{\text{eq}} n^{\text{eq}}}, \quad (8.9)$$

where  $n_{\text{eq}}$  is the equilibrium number density and relative velocity  $v_{ij}$  is defined by:

$$v_{ij} = \sqrt{\frac{(p_i \cdot p_j)^2 - m_i^2 m_j^2}{E_i E_j}}, \quad (8.10)$$

with  $p_i$  and  $E_i$  being the four-momentum and the energy respectively of particle  $i$ . The cold dark matter relic density is eventually demonstrated to have a direct proportionality to the mass of the stable dark matter particle,  $\Omega_\chi h^2 \propto m_\chi$  (see also the more generalised discussion about relic density calculations in Chapter 2 and Eq. (2.11)).

$s$ -channel annihilation occurs predominantly via  $Z$  boson (which couples to the inert Higgsino components of the neutralino) and Higgs exchange [130], particularly the former (see Fig. 8.32).

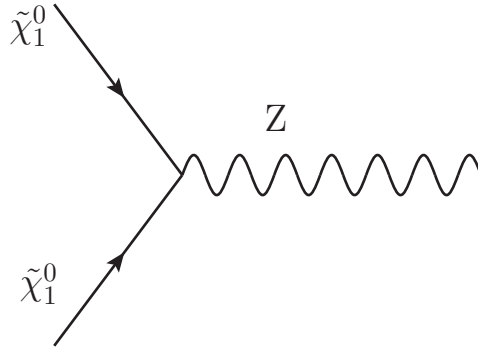


**Figure 8.32:**  $s$ -channel LSP annihilation to a  $Z$  boson.

The interactions of the neutralino states  $\chi_\alpha$  with  $Z$  bosons is described in the Lagrangian by:

$$\mathcal{L}_{Z\chi\chi} = \sum_{\alpha,\beta} \frac{M_Z}{2v} Z_\mu (\bar{\chi}_\alpha^0 \gamma_\mu \gamma_5 \chi_\beta^0) R_{Z\alpha\beta}, \quad (8.11)$$

where

$$R_{Z\alpha\beta} = R_{Z\alpha\alpha}\delta_{\alpha\beta}, \quad R_{Z\alpha\alpha} = \frac{v^2}{2m_{\chi_\alpha^\pm}^2} \left( f_\alpha^2 \cos^2\beta - \tilde{f}_\alpha^2 \sin^2\beta \right). \quad (8.12)$$

In the MSSM, in which the neutralino has four components (bino, wino and two Higgsinos), the lightest neutralino-neutralino- $Z$  Lagrangian is given by:

$$\mathcal{L}_{Z\tilde{\chi}_l^0\tilde{\chi}_n^0} = \frac{g_2}{2c_W} Z_\mu \tilde{\chi}_l^0 \gamma^\mu (N_{ln}^L P_L + N_{ln}^R P_R) \tilde{\chi}_n^0, \quad (8.13)$$

with:

$$N_{ln}^L = -\frac{1}{2} Z_{l3} Z_{n3}^* + \frac{1}{2} Z_{l4} Z_{n4}^*, \quad (8.14)$$

$$N_{ln}^R = -(N_{ln}^L)^*. \quad (8.15)$$

Two component neutralino mass eigenstate fields have been defined by:

$$\chi_l^0 = Z_{ln} \phi_n^0, \quad (8.16)$$

where  $Z$  is a  $4 \times 4$  unitary matrix that satisfies the diagonalisation of the neutralino mass matrix  $\mathcal{M}^n$ :

$$Z^* \mathcal{M}^n Z^{-1} = \mathcal{M}_n^D. \quad (8.17)$$

To extend this to our version of the  $E_6$ SSM, the neutralino mixing matrix must be extended to a  $10 \times 10$  spread, including columns for  $\tilde{S}$ ,  $\tilde{B}'$  and the four inert Higgsinos. How does this impact the neutralino mass and thus the relic density? Hall & King [130] performed a simple analytical estimate for the example of a  $12 \times 12$  mass matrix with the inert Higgsinos and singlinos being decoupled from the rest of the neutralino mass eigenstates. The lightest neutralino was then a superposition of three interaction states (where  $N_1^i$  are neutralino mixing matrix elements), being mostly singlino:

$$\tilde{\chi}_1^0 = N_1^1 \tilde{H}_{d1}^0 + N_1^2 \tilde{H}_{u1}^0 + N_1^3 \tilde{S}_1. \quad (8.18)$$

In our scenario,  $\tilde{S}_1$  and  $\tilde{S}_2$  are not considered to be part of the neutralino mass mixing

matrix. If the inert Higgsinos alone were to be decoupled from the neutralino mass matrix, this would lead to a  $4 \times 4$  matrix (including both first and second generations):

$$M_{\text{Inert Higgsinos}}^N = \begin{pmatrix} 0 & 0 & -\frac{\lambda_{11}s}{\sqrt{2}} & -\frac{\lambda_{12}s}{\sqrt{2}} \\ 0 & 0 & -\frac{\lambda_{21}s}{\sqrt{2}} & -\frac{\lambda_{22}s}{\sqrt{2}} \\ -\frac{\lambda_{11}s}{\sqrt{2}} & -\frac{\lambda_{12}s}{\sqrt{2}} & 0 & 0 \\ -\frac{\lambda_{21}s}{\sqrt{2}} & -\frac{\lambda_{22}s}{\sqrt{2}} & 0 & 0 \end{pmatrix}. \quad (8.19)$$

Using micrOMEGAs, we determined that the co-annihilation channels involving this neutralino can successfully yield the relic density desired. However, there is a very large number of these channels, many contributing less than 1% to  $(\Omega h^2)^{-1}$  - for some scenarios, the dominant channels do not contribute more than 8%. For the majority of the ten benchmark scenarios acquired, the dominant contributions to  $(\Omega h^2)^{-1}$  tend to occur via annihilation of the lightest neutralino with the lightest chargino, resulting in quark pair-production.

$$\tilde{\chi}_1^0 \tilde{\chi}^+ \rightarrow u \bar{d}, \quad (8.20)$$

$$\tilde{\chi}_1^0 \tilde{\chi}^+ \rightarrow c \bar{s}, \quad (8.21)$$

$$\tilde{\chi}_1^0 \tilde{\chi}^+ \rightarrow t \bar{b}. \quad (8.22)$$

However, in some points other processes dominate over  $\tilde{\chi}_1^0 \tilde{\chi}^+$  coannihilation. For example, in **BM7** and **BM12** the dominant contribution is derived instead from the second lightest neutralino with the first chargino:

$$\tilde{\chi}_2^0 + \tilde{\chi}^+ \rightarrow t \bar{b}, \quad (8.23)$$

$$\tilde{\chi}_2^0 + \tilde{\chi}^+ \rightarrow u \bar{d}, \quad (8.24)$$

$$\tilde{\chi}_2^0 + \tilde{\chi}^+ \rightarrow c \bar{s}. \quad (8.25)$$

For **BM9**, the two dominant contributions are by LSP coannihilation to produce  $t \bar{t}$  and

$W^+W^-$ :

$$\tilde{\chi}_1^0 \tilde{\chi}_1^0 \rightarrow t\bar{t}, \quad (8.26)$$

$$\tilde{\chi}_1^0 \tilde{\chi}_1^0 \rightarrow W^+W^-. \quad (8.27)$$

The top contributions of **BM11** stem from both the lightest neutralino and the second lightest neutralino with the first chargino:

$$\tilde{\chi}_2^0 \tilde{\chi}^+ \rightarrow t\bar{b}, \quad (8.28)$$

$$\tilde{\chi}_1^0 \tilde{\chi}^+ \rightarrow t\bar{b}, \quad (8.29)$$

$$\tilde{\chi}_2^0 \tilde{\chi}^+ \rightarrow u\bar{d}. \quad (8.30)$$

The three ruled out light neutralino scenarios do not generate top quark pairs via coannihilation. However, the second and third both feature noticeably large contributions from the lightest neutralino and positive chargino annihilating to quark pairs (excluding top and bottom quark production). The third is the only scenario that features large contributions from these chargino coannihilation channels:

$$\tilde{\chi}^+ \tilde{\chi}^- \rightarrow AA, \quad (8.31)$$

$$\tilde{\chi}^+ \tilde{\chi}^- \rightarrow e_1 \bar{e}_1, \quad (8.32)$$

$$\tilde{\chi}^+ \tilde{\chi}^- \rightarrow e_2 \bar{e}_2, \quad (8.33)$$

$$\tilde{\chi}^+ \tilde{\chi}^- \rightarrow e_3 \bar{e}_3. \quad (8.34)$$

## 8.7 Outlook

These results demonstrate that there are still significant regions of the  $E_6$ SSM that are compatible with relic abundance and the latest results from the LHC, including a 125 GeV Higgs boson. Now that these benchmark points have been laid out, they may also provide a map for colliders and dark matter detectors as they search for signs of increasingly elusive supersymmetric physics. The scattering data of particle collisions at the LHC may either confirm this model of the  $E_6$ SSM or conclusively eliminate more regions of its parameter space. Bounds on the squark and gluino masses will be particularly important.

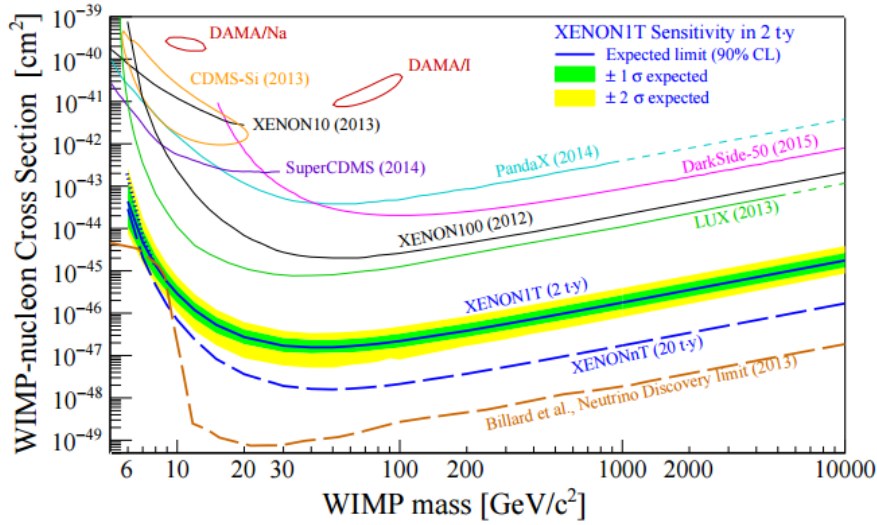


**Figure 8.33:** A plot from the XENON collaboration [134] demonstrating the XENON1T sensitivity (with 90% c.l.) compared to past experiments. This is a sensitivity easily great enough to detect most of the benchmark points given in this chapter.

When the LHC started its first operational run in 2012, it reached peak collision energies of 7 TeV. It has since reached a record breaking peak collision energy of 13 TeV and the next planned upgrade in 2017 will take it to new heights of 14 TeV. In the relatively near future, planned colliders may probe higher energy thresholds still, with the proposed Very Large Hadron Collider (VLHC) reaching collider energies up to a staggering 100 TeV. Such an energy would be sufficient to explore the majority of parameter values (and resulting particle spectra) of this scan.

At the present time, the initial run II results from the LHC have been made available, and the XENON1T experiment, the next evolution of XENON100, will soon begin to publish results. The sensitivity of this experiment is expected to reach a minimum spin-independent WIMP-nucleon cross section of  $1.6 \times 10^{-47} \text{ cm}^2$  at  $m_\chi = 50 \text{ GeV}$ , a factor of approximately 50 times better than the current LUX limit at the same WIMP mass [134]. As Fig. 8.33 demonstrates, this is sensitive enough to be able to detect almost all of the benchmark points above, with the exception of **BM7**.

	<b>BM1</b>	<b>BM2</b>	<b>BM3</b>	<b>BM4</b>	<b>BM5</b>	<b>BM6</b>
$\Omega h^2$	0.1190	0.1203	0.1199	0.1193	0.1196	0.1191
$\sigma_{SI}$ (cm <sup>2</sup> )	$1.20 \times 10^{-46}$	$4.73 \times 10^{-46}$	$4.91 \times 10^{-45}$	$8.46 \times 10^{-46}$	$1.65 \times 10^{-45}$	$3.31 \times 10^{-46}$
$\lambda$	-0.0655	-0.1167	-0.1058	-0.2176	0.2733	0.1367
$\kappa$	0.2211	0.2266	0.0906	0.1162	0.1156	0.0948
$\tan\beta$	29.3	16.2	28.0	23.1	16.0	18.5
$s$ (GeV)	52966.4	32388.8	17686.2	16671.1	59450.7	64162.7
$m_{\tilde{\chi}_1^0}$ (GeV)	1104.0	1013.3	1058.2	1123.3	1117.3	1130.3
$m_0$ (GeV)	19262.0	12142.6	10103.9	10234.8	24461.6	26233.7
$M_{1/2}$ (GeV)	7387.5	6621.6	7323.5	9104.0	8038.7	9503.8
$m_{h_1}$ (GeV)	124.8	125.4	125.6	125.2	125.5	125.2
$M_1$ (GeV)	1166.4	1035.9	1152.2	1445.1	1291.6	1519.1
$M_2$ (GeV)	2069.4	1834.7	2043.6	2543.6	2300.0	2706.5
$M'_1$ (GeV)	1193.4	1054.2	1166.9	1436.1	1310.8	1546.0
$M_3$ (GeV)	6163.5	5400.3	5839.3	7133.5	6718.1	7840.2
$m_{\tilde{t}_1}$	15185.3	10823.3	9967.8	11625.6	17138.6	18895.6
$m_{\tilde{b}_1}$	18541.2	13508.0	12228.3	14240.9	22835.7	24880.2
$m_{\tilde{d}L}$	21862.0	15261.7	14367.6	16293.3	26923.7	29409.5
$\mu_{D_i}$ (GeV)	20570.7	12248.8	2919.0	1568.2	9469.6	10390.2
$\mu_{\tilde{H}_1}$ (GeV)	9122.3	3452.2	5816.5	9217.8	14681.2	25331.3
$\mu_{\tilde{H}_2}$ (GeV)	1041.1	1184.3	7315.2	2042.6	31788.4	27637.3
$m_{Z'}$ (GeV)	19597.6	11983.9	6544.0	6168.4	21996.8	23740.2
$A_0$	6269.1	-1276.0	-3526.2	-9676.2	18481.5	18080.3
$A_\lambda$	-4027.3	-4188.6	-3293.1	-4995.1	2872.8	2146.5
$ Z(N)_{11} ^2$	0.0238	0.1410	0.0895	0.0082	0.0230	0.0048
$ Z(N)_{12} ^2$	0.0003	0.0004	0.0028	0.0015	0.0017	0.0010
$ Z(N)_{13} ^2$	$6.46 \times 10^{-6}$	0.0051	0.2292	0.0481	0.3813	0.4675
$ Z(N)_{14} ^2$	0.0497	0.0404	0.4465	0.4700	0.4241	0.3439
$ Z(N)_{15} ^2$	$1.72 \times 10^{-7}$	$3.97 \times 10^{-9}$	$1.50 \times 10^{-5}$	$1.75 \times 10^{-5}$	$1.37 \times 10^{-6}$	$6.63 \times 10^{-7}$
$ Z(N)_{16} ^2$	$1.36 \times 10^{-9}$	$8.03 \times 10^{-9}$	$9.03 \times 10^{-7}$	$1.26 \times 10^{-6}$	$7.57 \times 10^{-9}$	$3.88 \times 10^{-9}$
$ Z(N)_{17} ^2$	0.4886	0.4125	0.0493	0.4319	0.1081	0.0300
$ Z(N)_{18} ^2$	0.4250	0.0631	0.0010	0.0203	0.0381	0.0599
$ Z(N)_{19} ^2$	$9.80 \times 10^{-5}$	0.0135	0.1809	0.0174	0.0013	0.0010
$ Z(N)_{110} ^2$	0.0123	0.3240	0.0008	0.0027	0.0216	0.0919

**Table 8.2:** The first six benchmark points based on the lightest neutralino content. **BM1** and **BM2** feature a neutralino with a high inert Higgsino content. The lightest neutralino of **BM3** has a high Higgsino content and a reasonably large contribution from the inert Higgsinos. **BM4** has a high mixture of both Higgsino and inert Higgsino. **BM5** and **BM6** have high Higgsino content.

	<b>BM7</b>	<b>BM8</b>	<b>BM9</b>	<b>BM10</b>	<b>BM11</b>	<b>BM12</b>
$\Omega h^2$	0.1200	0.1187	0.1195	0.1202	0.1199	0.1195
$\sigma_{SI}$ (cm <sup>2</sup> )	$1.85 \times 10^{-47}$	$2.12 \times 10^{-46}$	$1.12 \times 10^{-45}$	$7.60 \times 10^{-45}$	$4.64 \times 10^{-46}$	$6.21 \times 10^{-46}$
$\lambda$	-0.0970	0.0579	0.1394	-0.1107	-0.0961	-0.6689
$\kappa$	0.2475	0.2116	0.0383	0.1297	0.1784	0.1517
$\tan\beta$	39.8	24.5	27.8	24.2	18.9	26.7
$s$ (GeV)	51923.7	34632.7	11306.1	33556.4	22557.4	11876.7
$m_{\tilde{\chi}_1^0}$ (GeV)	699.5	324.6	307.6	957.2	932.0	829.8
$m_0$ (GeV)	19733.4	14407.1	7707.2	12100.1	9412.9	7034.6
$M_{1/2}$ (GeV)	4330.4	2005.8	1926.2	6377.2	5977.0	5089.7
$m_{h_1}$ (GeV)	125.2	124.9	125.4	125.3	125.4	125.7
$M_1$ (GeV)	700.4	327.1	313.0	1008.6	939.6	835.1
$M_2$ (GeV)	1245.2	580.7	560.3	1789.6	1662.9	1450.8
$M_1'$ (GeV)	720.1	339.1	317.5	1023.7	949.7	796.9
$M_3$ (GeV)	3875.8	1917.6	1723.4	5199.9	4835.8	4118.4
$m_{\tilde{t}_1}$	13875.4	9442.8	4811.1	10792.4	8938.9	6990.3
$m_{\tilde{b}_1}$	16312.3	12147.1	6376.6	13168.4	11067.5	8558.7
$m_{\tilde{d}L}$	20654.0	14684.0	8166.6	15018.9	12573.0	9980.4
$\mu_{D_i}$ (GeV)	20538.4	13301.4	702.2	6453.8	5827.1	783.6
$\mu_{\tilde{H}_1}$ (GeV)	172.9	479.1	1208.7	2282.2	1684.2	903.5
$\mu_{\tilde{H}_2}$ (GeV)	5778.6	2460.8	6367.9	20566.4	10327.2	7105.7
$m_{Z'}$ (GeV)	19211.8	12814.2	4183.4	12415.9	8346.3	4394.5
$A_0$	14118.9	13490.4	7097.8	-2030.5	-3368.4	-3427.9
$A_\lambda$	-2046.3	2225.7	1605.2	-2722.5	-3203.2	-2142.0
$ Z(N)_{11} ^2$	0.9108	0.8850	0.8079	0.2279	0.3030	0.5574
$ Z(N)_{12} ^2$	$8.61 \times 10^{-6}$	0.0003	0.0013	0.0030	0.0001	0.0001
$ Z(N)_{13} ^2$	0.0028	0.0013	0.0887	0.0363	0.2188	0.2114
$ Z(N)_{14} ^2$	0.0003	0.0031	0.0152	0.3309	0.0148	0.0119
$ Z(N)_{15} ^2$	$9.94 \times 10^{-10}$	$2.74 \times 10^{-8}$	$1.47 \times 10^{-6}$	$2.96 \times 10^{-6}$	$4.80 \times 10^{-7}$	$1.24 \times 10^{-6}$
$ Z(N)_{16} ^2$	$1.45 \times 10^{-10}$	$8.63 \times 10^{-10}$	$1.17 \times 10^{-7}$	$4.47 \times 10^{-8}$	$1.77 \times 10^{-8}$	$1.93 \times 10^{-7}$
$ Z(N)_{17} ^2$	0.0033	$2.98 \times 10^{-5}$	0.0150	$4.62 \times 10^{-5}$	0.0416	$4.97 \times 10^{-5}$
$ Z(N)_{18} ^2$	0.0033	0.0419	0.0004	0.0124	0.0021	0.0035
$ Z(N)_{19} ^2$	0.0390	0.0598	0.0008	0.3558	0.0907	0.0123
$ Z(N)_{110} ^2$	0.0404	0.0086	0.0707	0.0337	0.3296	0.2033

**Table 8.3:** Six more benchmark points selected based on neutralino content. The lightest neutralino of **BM7**, **BM8** and **BM9** is heavily bino dominated. The lightest neutralino of **BM10**, **BM11** and **BM12** is a mixture of bino, Higgsino and inert Higgsino.

	Scenario 1 (ruled out)	Scenario 2 (ruled out)	Scenario 3 (ruled out)
$\Omega h^2$	0.1192	0.1193	0.1190
$\sigma_{SI}$ (cm <sup>2</sup> )	$5.89 \times 10^{-46}$	$1.1 \times 10^{-46}$	$2.98 \times 10^{-47}$
$\lambda$	0.1467	0.2430	0.4664
$\kappa$	0.1109	0.1133	0.1828
$\tan\beta$	32.1	18.3	8.5
$s$ (GeV)	25003.4	43719.5	77778.6
$m_{\tilde{\chi}_1^0}$ (GeV)	17.7	10.1	5.3
$m_0$ (GeV)	10718.9	19617.1	24282.2
$M_{1/2}$ (GeV)	2991.6	7634.5	10196.2
$m_{h_1}$ (GeV)	125.6	126.3	127.1
$M_1$ (GeV)	482.9	1221.0	1630.4
$M_2$ (GeV)	862.4	2171.6	2897.2
$M'_1$ (GeV)	492.0	1237.1	1658.9
$M_3$ (GeV)	2621.4	6314.0	8353.3
$m_{\tilde{t}_1}$ (GeV)	7553.8	14169.5	18147.8
$m_{\tilde{b}_1}$ (GeV)	9327.3	18775.6	24660.7
$m_{\tilde{d}_L}$ (GeV)	11509.1	22333.5	28164.4
$\mu_{D_i}$ ( $i = 1, 2, 3$ ) (GeV)	4428.5	7135.6	19332.3
$\mu_{\tilde{H}_1}$ (GeV)	3659.6	9841.1	22159.9
$\mu_{\tilde{H}_2}$ (GeV)	14127.9	22567.5	33311.6
$m_{Z'}$ (GeV)	9251.3	16176.3	28778.1
$A_0$	6937.4	13034.4	20732.4
$A_\lambda$	30.9	1678.9	1038.2
$ Z(N)_{11} ^2$	0.0029	0.0004	0.0003
$ Z(N)_{12} ^2$	0.0030	0.0005	0.0003
$ Z(N)_{13} ^2$	0.2828	0.3306	0.3328
$ Z(N)_{14} ^2$	0.3502	0.3875	0.2865
$ Z(N)_{15} ^2$	$5.89 \times 10^{-6}$	$2.27 \times 10^{-6}$	$2.96 \times 10^{-7}$
$ Z(N)_{16} ^2$	$1.93 \times 10^{-10}$	$5.20 \times 10^{-12}$	$1.51 \times 10^{-13}$
$ Z(N)_{17} ^2$	0.0195	0.1387	0.0323
$ Z(N)_{18} ^2$	0.0279	0.0112	0.0826
$ Z(N)_{19} ^2$	0.3100	0.1164	0.2227
$ Z(N)_{110} ^2$	0.0038	0.0147	0.0425

**Table 8.4:** Three light neutralino scenarios ( $< 100$  GeV). Each are low on bino content. Their lightest chargino is also lighter than 100 GeV, which rules them out for future detection.

	BM1	BM2	BM3	BM4	BM5	BM6
$\tilde{\chi}_1^0 \tilde{\chi}^+ \rightarrow t\bar{b}$	7.2%	7.1%	7.8%	7.5%	7.9%	7.6%
$\tilde{\chi}_1^0 \tilde{\chi}^+ \rightarrow u\bar{d}$	7.0%	6.9%	8.1%	7.8%	7.8%	7.5%
$\tilde{\chi}_1^0 \tilde{\chi}^+ \rightarrow c\bar{s}$	6.9%	6.9%	8.1%	7.7%	7.8%	7.5%
$\tilde{\chi}_1^0 \tilde{\chi}^+ \rightarrow n_1 \bar{e}_1$	2.4%	2.4%	2.8%	2.7%	2.7%	2.6%
$\tilde{\chi}_1^0 \tilde{\chi}^+ \rightarrow n_2 \bar{e}_2$	2.4%	2.4%	2.8%	2.7%	2.7%	2.6%
$\tilde{\chi}_1^0 \tilde{\chi}^+ \rightarrow n_3 \bar{e}_3$	2.4%	2.4%	2.8%	2.7%	2.7%	2.6%
$\tilde{\chi}_1^0 \tilde{\chi}^+ \rightarrow ZW^+$	1.0%	1.0%	1.6%	1.3%	1.4%	1.1%
$\tilde{\chi}_1^0 \tilde{\chi}^+ \rightarrow AW^+$	1.2%	1.2%	1.4%	1.3%	1.3%	1.3%
$\tilde{\chi}_1^0 \tilde{\chi}^+ \rightarrow h_1 W^+$	0.6%	0.6%	1.3%	1.0%	1.0%	0.9%
$\tilde{\chi}_2^0 \tilde{\chi}^+ \rightarrow t\bar{b}$	6.1%	5.7%	3.7%	4.8%	4.8%	5.4%
$\tilde{\chi}_2^0 \tilde{\chi}^+ \rightarrow u\bar{d}$	5.9%	5.6%	4.0%	5.0%	4.8%	5.3%
$\tilde{\chi}_2^0 \tilde{\chi}^+ \rightarrow c\bar{s}$	6.9%	5.5%	4.0%	5.0%	4.7%	5.3%
$\tilde{\chi}_2^0 \tilde{\chi}^+ \rightarrow n_1 \bar{e}_1$	2.1%	1.9%	1.4%	1.8%	1.7%	1.9%
$\tilde{\chi}_2^0 \tilde{\chi}^+ \rightarrow n_2 \bar{e}_2$	2.1%	1.9%	1.4%	1.8%	1.7%	1.9%
$\tilde{\chi}_2^0 \tilde{\chi}^+ \rightarrow n_3 \bar{e}_3$	2.1%	1.9%	1.4%	1.8%	1.7%	1.9%
$\tilde{\chi}_1^0 \tilde{\chi}_1^0 \rightarrow W^+ W^-$	1.8%	2.3%	4.7%	2.7%	3.1%	2.2%
$\tilde{\chi}_1^0 \tilde{\chi}_1^0 \rightarrow ZZ$	1.5%	1.9%	3.8%	2.2%	2.5%	1.8%
$\tilde{\chi}_1^0 \tilde{\chi}_1^0 \rightarrow t\bar{t}$	0.0%	0.1%	1.4%	0.1%	0.3%	0.0%
$\tilde{\chi}_1^0 \tilde{\chi}_2^0 \rightarrow d\bar{d}$	2.2%	2.1%	2.1%	2.0%	2.1%	2.0%
$\tilde{\chi}_1^0 \tilde{\chi}_2^0 \rightarrow s\bar{s}$	2.2%	2.1%	2.1%	2.0%	2.1%	2.0%
$\tilde{\chi}_1^0 \tilde{\chi}_2^0 \rightarrow b\bar{b}$	2.2%	2.1%	2.0%	2.0%	2.1%	2.0%
$\tilde{\chi}_1^0 \tilde{\chi}_2^0 \rightarrow u\bar{u}$	1.7%	1.7%	1.6%	1.6%	1.6%	1.6%
$\tilde{\chi}_1^0 \tilde{\chi}_2^0 \rightarrow c\bar{c}$	1.7%	1.7%	1.6%	1.6%	1.6%	1.6%
$\tilde{\chi}_1^0 \tilde{\chi}_2^0 \rightarrow t\bar{t}$	1.6%	1.6%	1.4%	1.3%	1.5%	1.5%
$\tilde{\chi}_2^0 \tilde{\chi}_2^0 \rightarrow W^+ W^-$	1.1%	1.0%	0.6%	0.8%	0.8%	0.9%
$\tilde{\chi}^+ \tilde{\chi}^- \rightarrow W^+ W^-$	2.7%	2.5%	1.9%	2.4%	2.2%	2.5%
$\tilde{\chi}^+ \tilde{\chi}^- \rightarrow u\bar{u}$	2.1%	2.0%	1.7%	2.1%	2.0%	2.1%
$\tilde{\chi}^+ \tilde{\chi}^- \rightarrow c\bar{c}$	2.1%	2.0%	1.7%	2.1%	2.0%	2.1%
$\tilde{\chi}^+ \tilde{\chi}^- \rightarrow t\bar{t}$	2.1%	2.0%	1.6%	2.0%	1.9%	2.1%
$\tilde{\chi}^+ \tilde{\chi}^- \rightarrow d\bar{d}$	1.4%	1.3%	1.1%	1.3%	1.2%	1.4%
$\tilde{\chi}^+ \tilde{\chi}^- \rightarrow s\bar{s}$	1.4%	1.3%	1.1%	1.3%	1.2%	1.4%
$\tilde{\chi}^+ \tilde{\chi}^- \rightarrow b\bar{b}$	1.3%	1.3%	0.9%	1.1%	1.2%	1.3%
$\tilde{\chi}^+ \tilde{\chi}^- \rightarrow e_1 \bar{e}_1$	1.1%	1.0%	0.8%	1.0%	1.0%	1.1%
$\tilde{\chi}^+ \tilde{\chi}^- \rightarrow e_2 \bar{e}_2$	1.1%	1.0%	0.8%	1.0%	1.0%	1.1%
$\tilde{\chi}^+ \tilde{\chi}^- \rightarrow e_3 \bar{e}_3$	1.1%	1.0%	0.8%	1.0%	1.0%	1.1%

**Table 8.5:** The coannihilation channels that contribute to  $(\Omega h^2)^{-1}$  for the first six benchmarks. There are many other contributing channels taking the total up to 100% for each benchmark, but for the sake of brevity they are not included in this table if they do not contribute at least 1% for at least one benchmark point. The same is true of Table 8.6.

	BM7	BM8	BM9	BM10	BM11	BM12	LN1	LN2	LN3
$\tilde{\chi}_1^0 \tilde{\chi}^+ \rightarrow t\bar{b}$	1.3%	5.3%	7.9%	8.4%	6.0%	4.7%	0.0%	0.0%	0.0%
$\tilde{\chi}_1^0 \tilde{\chi}^+ \rightarrow u\bar{d}$	1.2%	4.9%	6.7%	7.8%	5.8%	4.6%	21%	30%	5.6%
$\tilde{\chi}_1^0 \tilde{\chi}^+ \rightarrow c\bar{s}$	1.2%	4.9%	6.6%	7.8%	5.8%	4.6%	21%	29%	5.5%
$\tilde{\chi}_1^0 \tilde{\chi}^+ \rightarrow u\bar{s}$	0.1%	0.3%	0.3%	0.4%	0.3%	0.2%	1.1%	1.5%	0.3%
$\tilde{\chi}_1^0 \tilde{\chi}^+ \rightarrow \bar{d}c$	0.1%	0.3%	0.3%	0.4%	0.3%	0.2%	1.1%	1.5%	0.3%
$\tilde{\chi}_1^0 \tilde{\chi}^+ \rightarrow c\bar{c}$	0.0%	0.0%	0.0%	0.0%	0.0%	0.0%	0.0%	0.8%	0.0%
$\tilde{\chi}_1^0 \tilde{\chi}^+ \rightarrow u\bar{u}$	0.0%	0.0%	0.0%	0.0%	0.0%	0.0%	0.0%	0.6%	0.0%
$\tilde{\chi}_1^0 \tilde{\chi}^+ \rightarrow n_1 \bar{e}_1$	0.4%	1.7%	2.3%	2.7%	2.0%	1.6%	7.5%	10%	2.0%
$\tilde{\chi}_1^0 \tilde{\chi}^+ \rightarrow n_2 \bar{e}_2$	0.4%	1.7%	2.3%	2.7%	2.0%	1.6%	7.5%	10%	2.0%
$\tilde{\chi}_1^0 \tilde{\chi}^+ \rightarrow n_3 \bar{e}_3$	0.4%	1.7%	2.3%	2.7%	2.0%	1.6%	7.4%	10%	1.9%
$\tilde{\chi}_1^0 \tilde{\chi}^+ \rightarrow AW^+$	0.2%	0.9%	1.2%	1.4%	1.0%	0.8%	0.0%	0.0%	0.0%
$\tilde{\chi}_1^0 \tilde{\chi}^+ \rightarrow ZW^+$	0.2%	0.7%	1.1%	1.6%	0.8%	0.7%	0.0%	0.0%	0.0%
$\tilde{\chi}_1^0 \tilde{\chi}^+ \rightarrow h_1 W^+$	0.1%	0.7%	1.3%	1.4%	0.5%	0.5%	0.0%	0.0%	0.0%
$\tilde{\chi}_2^0 \tilde{\chi}^+ \rightarrow t\bar{b}$	6.4%	4.0%	1.7%	3.3%	6.0%	5.8%	0.0%	0.0%	0.0%
$\tilde{\chi}_2^0 \tilde{\chi}^+ \rightarrow u\bar{d}$	6.3%	4.2%	1.9%	3.4%	5.9%	5.8%	0.0%	0.0%	0.0%
$\tilde{\chi}_2^0 \tilde{\chi}^+ \rightarrow c\bar{s}$	6.3%	4.2%	1.9%	3.4%	5.9%	5.8%	0.0%	0.0%	0.0%
$\tilde{\chi}_2^0 \tilde{\chi}^+ \rightarrow n_1 \bar{e}_1$	2.2%	1.5%	0.7%	1.2%	2.1%	2.0%	0.0%	0.0%	0.0%
$\tilde{\chi}_2^0 \tilde{\chi}^+ \rightarrow n_2 \bar{e}_2$	2.2%	1.5%	0.7%	1.2%	2.1%	2.0%	0.0%	0.0%	0.0%
$\tilde{\chi}_2^0 \tilde{\chi}^+ \rightarrow n_3 \bar{e}_3$	2.2%	1.5%	0.7%	1.2%	2.1%	2.0%	0.0%	0.0%	0.0%
$\tilde{\chi}_2^0 \tilde{\chi}^+ \rightarrow AW^+$	1.1%	0.7%	0.3%	0.6%	1.0%	1.0%	0.0%	0.0%	0.0%
$\tilde{\chi}_3^0 \tilde{\chi}^+ \rightarrow t\bar{b}$	5.5%	3.1%	1.1%	0.2%	1.2%	2.4%	0.0%	0.0%	0.0%
$\tilde{\chi}_3^0 \tilde{\chi}^+ \rightarrow u\bar{d}$	5.4%	3.2%	1.2%	0.1%	1.1%	2.3%	0.0%	0.0%	0.0%
$\tilde{\chi}_3^0 \tilde{\chi}^+ \rightarrow c\bar{s}$	5.4%	3.2%	1.2%	0.1%	1.1%	2.3%	0.0%	0.0%	0.0%
$\tilde{\chi}_3^0 \tilde{\chi}^+ \rightarrow n_1 \bar{e}_1$	1.9%	1.1%	0.4%	0.0%	0.4%	0.8%	0.0%	0.0%	0.0%
$\tilde{\chi}_3^0 \tilde{\chi}^+ \rightarrow n_2 \bar{e}_2$	1.9%	1.1%	0.4%	0.0%	0.4%	0.8%	0.0%	0.0%	0.0%
$\tilde{\chi}_3^0 \tilde{\chi}^+ \rightarrow n_3 \bar{e}_3$	1.9%	1.1%	0.4%	0.0%	0.4%	0.8%	0.0%	0.0%	0.0%
$\tilde{\chi}_1^0 \tilde{\chi}_1^0 \rightarrow t\bar{t}$	0.0%	2.0%	13%	4.0%	0.1%	0.2%	0.0%	0.0%	0.0%
$\tilde{\chi}_1^0 \tilde{\chi}_1^0 \rightarrow b\bar{b}$	0.0%	0.0%	0.0%	0.0%	0.0%	0.0%	6.8%	2.2%	0.6%
$\tilde{\chi}_1^0 \tilde{\chi}_1^0 \rightarrow s\bar{s}$	0.0%	0.0%	0.0%	0.0%	0.0%	0.0%	4.6%	0.8%	0.1%
$\tilde{\chi}_1^0 \tilde{\chi}_1^0 \rightarrow c\bar{c}$	0.0%	0.0%	0.0%	0.0%	0.0%	0.0%	3.8%	0.8%	0.2%
$\tilde{\chi}_1^0 \tilde{\chi}_1^0 \rightarrow d\bar{d}$	0.0%	0.0%	0.0%	0.0%	0.0%	0.0%	4.6%	0.8%	0.1%
$\tilde{\chi}_1^0 \tilde{\chi}_1^0 \rightarrow u\bar{u}$	0.0%	0.0%	0.0%	0.0%	0.0%	0.0%	3.6%	0.6%	0.1%
$\tilde{\chi}_1^0 \tilde{\chi}_1^0 \rightarrow e_1 \bar{e}_1$	0.0%	0.0%	0.0%	0.0%	0.0%	0.0%	1.0%	0.2%	0.0%
$\tilde{\chi}_1^0 \tilde{\chi}_1^0 \rightarrow e_2 \bar{e}_2$	0.0%	0.0%	0.0%	0.0%	0.0%	0.0%	1.0%	0.2%	0.0%
$\tilde{\chi}_1^0 \tilde{\chi}_1^0 \rightarrow e_3 \bar{e}_3$	0.0%	0.0%	0.0%	0.0%	0.0%	0.0%	1.2%	0.3%	0.1%
$\tilde{\chi}_1^0 \tilde{\chi}_1^0 \rightarrow n_1 \bar{n}_1$	0.0%	0.0%	0.0%	0.0%	0.0%	0.0%	2.1%	0.4%	0.1%
$\tilde{\chi}_1^0 \tilde{\chi}_1^0 \rightarrow n_2 \bar{n}_2$	0.0%	0.0%	0.0%	0.0%	0.0%	0.0%	2.1%	0.4%	0.1%
$\tilde{\chi}_1^0 \tilde{\chi}_1^0 \rightarrow n_3 \bar{n}_3$	0.0%	0.0%	0.0%	0.0%	0.0%	0.0%	2.1%	0.4%	0.1%
$\tilde{\chi}_1^0 \tilde{\chi}_1^0 \rightarrow W^+ W^-$	0.1%	2.3%	8.1%	5.7%	1.6%	1.3%	0.0%	0.0%	0.0%
$\tilde{\chi}_1^0 \tilde{\chi}_1^0 \rightarrow ZZ$	0.1%	1.8%	6.2%	4.6%	1.4%	1.1%	0.0%	0.0%	0.0%
$\tilde{\chi}_1^0 \tilde{\chi}_2^0 \rightarrow d\bar{d}$	0.4%	1.4%	1.6%	2.0%	1.9%	1.5%	0.0%	0.0%	0.0%
$\tilde{\chi}_1^0 \tilde{\chi}_2^0 \rightarrow s\bar{s}$	0.4%	1.4%	1.6%	2.0%	1.9%	1.5%	0.0%	0.0%	0.0%
$\tilde{\chi}_1^0 \tilde{\chi}_2^0 \rightarrow b\bar{b}$	0.4%	1.4%	1.6%	2.0%	1.8%	1.4%	0.0%	0.0%	0.0%
$\tilde{\chi}_1^0 \tilde{\chi}_2^0 \rightarrow u\bar{u}$	0.3%	1.1%	1.3%	1.6%	1.5%	1.2%	0.0%	0.0%	0.0%
$\tilde{\chi}_1^0 \tilde{\chi}_2^0 \rightarrow c\bar{c}$	0.3%	1.1%	1.3%	1.6%	1.5%	1.2%	0.0%	0.0%	0.0%
$\tilde{\chi}_1^0 \tilde{\chi}_2^0 \rightarrow t\bar{t}$	0.3%	1.1%	1.4%	1.7%	1.4%	1.2%	0.0%	0.0%	0.0%
$\tilde{\chi}_1^0 \tilde{\chi}_3^0 \rightarrow W^+ W^-$	0.4%	1.2%	1.2%	0.1%	0.4%	0.6%	0.0%	0.0%	0.0%
$\tilde{\chi}_2^0 \tilde{\chi}_2^0 \rightarrow W^+ W^-$	1.2%	0.7%	0.3%	0.6%	1.1%	1.1%	0.0%	0.0%	0.0%
$\tilde{\chi}_2^0 \tilde{\chi}_3^0 \rightarrow d\bar{d}$	1.7%	1.0%	0.3%	0.0%	0.4%	0.7%	0.0%	0.0%	0.0%
$\tilde{\chi}_2^0 \tilde{\chi}_3^0 \rightarrow s\bar{s}$	1.7%	1.0%	0.3%	0.0%	0.4%	0.7%	0.0%	0.0%	0.0%
$\tilde{\chi}_2^0 \tilde{\chi}_3^0 \rightarrow b\bar{b}$	1.7%	1.0%	0.3%	0.0%	0.3%	0.7%	0.0%	0.0%	0.0%
$\tilde{\chi}_2^0 \tilde{\chi}_3^0 \rightarrow u\bar{u}$	1.4%	0.7%	0.2%	0.0%	0.3%	0.6%	0.0%	0.0%	0.0%
$\tilde{\chi}_2^0 \tilde{\chi}_3^0 \rightarrow c\bar{c}$	1.4%	0.7%	0.2%	0.0%	0.3%	0.6%	0.0%	0.0%	0.0%
$\tilde{\chi}_2^0 \tilde{\chi}_3^0 \rightarrow t\bar{t}$	1.3%	0.5%	0.2%	0.1%	0.3%	0.6%	0.0%	0.0%	0.0%
$\tilde{\chi}^+ \tilde{\chi}^- \rightarrow W^+ W^-$	2.9%	2.1%	1.1%	1.6%	2.7%	2.6%	0.0%	0.0%	0.0%
$\tilde{\chi}^+ \tilde{\chi}^- \rightarrow u\bar{u}$	2.2%	1.6%	0.9%	1.5%	2.1%	2.1%	0.0%	0.0%	14%
$\tilde{\chi}^+ \tilde{\chi}^- \rightarrow c\bar{c}$	2.2%	1.6%	0.9%	1.5%	2.1%	2.1%	0.0%	0.0%	14%
$\tilde{\chi}^+ \tilde{\chi}^- \rightarrow t\bar{t}$	2.2%	1.5%	0.8%	1.4%	2.1%	2.0%	0.0%	0.0%	0.0%
$\tilde{\chi}^+ \tilde{\chi}^- \rightarrow d\bar{d}$	1.4%	1.0%	0.6%	0.9%	1.3%	1.3%	0.0%	0.0%	3.4%
$\tilde{\chi}^+ \tilde{\chi}^- \rightarrow s\bar{s}$	1.4%	1.0%	0.6%	0.9%	1.3%	1.3%	0.0%	0.0%	3.4%
$\tilde{\chi}^+ \tilde{\chi}^- \rightarrow b\bar{b}$	1.4%	1.0%	0.5%	0.8%	1.3%	1.3%	0.0%	0.0%	3.1%
$\tilde{\chi}^+ \tilde{\chi}^- \rightarrow e_1 \bar{e}_1$	1.1%	0.8%	0.4%	0.7%	1.0%	1.0%	0.0%	0.0%	11%
$\tilde{\chi}^+ \tilde{\chi}^- \rightarrow e_2 \bar{e}_2$	1.1%	0.8%	0.4%	0.7%	1.0%	1.0%	0.0%	0.0%	11%
$\tilde{\chi}^+ \tilde{\chi}^- \rightarrow e_3 \bar{e}_3$	1.1%	0.8%	0.4%	0.7%	1.0%	1.0%	0.0%	0.0%	11%
$\tilde{\chi}^+ \tilde{\chi}^- \rightarrow AA$	1.0%	0.7%	0.4%	0.6%	0.9%	0.9%	0.0%	0.0%	12%

**Table 8.6:** The coannihilation channels that contribute to  $(\Omega h^2)^{-1}$  for the last six benchmarks in addition to the three ruled out light neutralino scenarios (LN1, LN2 and LN3).



---

# Summary and outlook

---

The search for the mysterious dark matter of the universe continues around the world. Based on a wide array of cosmological evidence, the most likely candidate for this missing matter is a slow-moving, weakly interacting and stable particle, dubbed a WIMP. Many extensions of the standard model to incorporate this WIMP have been proposed, including supersymmetric models. Although supersymmetry has yet to be discovered at the LHC, models such as the NMSSM and  $E_6$ SSM still hold substantial predictive power in providing a suitable WIMP candidate in the form of a neutralino that may be detected in the near-future.

Supersymmetric models solve many outstanding problems of the current standard model, but are not without drawbacks of their own. The NMSSM is an extension of the MSSM that solves the  $\mu$  problem of the latter via the introduction of a new singlet superfield  $\hat{S}$ . In chapter 5, representing an early portion of my thesis based on older data, I investigated the constrained NMSSM, showing that it may still plausibly produce a viable candidate for dark matter in the form of its lightest neutralino, although the parameter space must be finely tuned. This has since been superseded by more recent work and data from the LHC in its latest run.

After this work, I moved on to the  $E_6$ SSM, which is a more complex model than the NMSSM with a much greater parameter space. The mixing mass matrix of the neutralinos in the extended  $E_6$ SSM has ten contributing fields - bino, wino, higgsinos, inert higgsinos, singlino and  $\tilde{B}'$ . The lightest neutralino tends to be either bino-dominated, higgsino-dominated or inert higgsino-dominated.

In chapter 7, I outlined the computational tools MultiNest, micrOMEGAs and FlexibleSUSY used in this part of my research. In the following chapter 8, I presented the results of my research investigating the extended  $E_6$ SSM by conducting the most extensive

scan of it to date. I demonstrated that despite increasingly stringent bounds from LHC data and dark matter detection experiments, there are still many regions of this supersymmetric model that yield a suitable dark matter candidate, and fifteen benchmark models were provided with a range of neutralino compositions and masses. Many yield heavy squarks, gluinos and exotic quarks that are well beyond the detectability of the LHC in its current run. Despite many of these masses lying beyond the reach of the LHC, the neutralino itself may well be discovered in the near-future by a dark matter experiment such as the upcoming XENON1T, which is the next evolution of the XENON100 experiment.

---

# Bibliography

---

- [1] G. Jungman, M. Kamionkowski, & K. Griest, *Phys. Rept.* **267**, 195 (1996).  
[arXiv:hep-ph/9506380]
- [2] F. Zwicky, *Helvetica Physica Acta* **6**, 110 (1993).
- [3] V. C. Rubin & W. K. J. Ford, *ApJ* **159**, 379 (1970).
- [4] University of Iowa Astronomy and Astrophysics, <http://astro.physics.uiowa.edu/~rlm/mathcad/addendum%2011%20galaxy%20rotation%20curves,dark%20matter.htm> [Accessed online April 2016]
- [5] V. C. Rubin, W. K. J. Ford, & N. Thonnard, *ApJ* **238**, 471 (1980).
- [6] J. F. Navarro, C. S. Frenk, & S. D. M. White, *ApJ* **462**, 563 (1996). [arXiv:astro-ph/9508025]
- [7] A. Burkert & J. Silk, *ApJ* **488**, L55 (1997). [arXiv:astro-ph/9707343]
- [8] G. Battaglia, A. Helmi, H. Morrison, *et al.*, *MNRAS* **364**, 433 (2005). [arXiv:astro-ph/0506102]
- [9] Image credit: Michael Sachs.
- [10] T. Treu, P. J. Marshall, & D. Clowe, *American Journal of Physics*, **80**, 753 (2012).  
[arXiv:1206.0791 [astro-ph.CO]]
- [11] J. P. Kneib & P. Natarajan, *Astron. Astrophys. Rev.*, **19**, 47 (2011). [arXiv:1202.0185 [astro-ph.CO]]
- [12] B. Paczynski, *Ann. Rev. Astron. Astrophys.* **34**, 419 (1996). [arXiv:astro-ph/9604011]
- [13] D. Clowe, M. Bradač, A. H. Gonzalez, *et al.*, *ApJ* **648**, L109 (2006). [arXiv:astro-ph/0608407]

- [14] W. L. Freedman, “Measuring and Modeling the Universe: Volume 2,” Carnegie Astrophysics Series, Cambridge, UK: Cambridge University Press (2004).
- [15] D. J. Fixsen, *ApJ* **707**, 916 (2009). [arXiv:0911.1955 [astro-ph.CO]]
- [16] M. Giovannini, “A Primer on the Physics of the Cosmic Microwave Background,” ISBN 978-981-279-142-9. Published by World Scientific Publishing Co., Pte. Ltd., Singapore (2008).
- [17] Image credit: NASA / WMAP Science Team, <http://map.gsfc.nasa.gov/media/060913/index.html> [Accessed December 2015]
- [18] D. G. York, J. Adelman, J. E. Anderson, Jr., *et al.*, *AJ* **120**, 1579 (2000). [arXiv:astro-ph/0006396]
- [19] D. J. Eisenstein, I. Zehavi, D. W. Hogg, *et al.*, *ApJ* **633**, 560 (2005). [arXiv:astro-ph/0501171]
- [20] B. W. Carroll and D. A. Ostlie, “An Introduction to Modern Astrophysics,” Reading, USA: Addison-Wesley Publishing Company (1996).
- [21] Particle Data Group, [http://pdg.lbl.gov/2014/html/Condensed\\_Reviews\\_Booklet\\_2014.pdf](http://pdg.lbl.gov/2014/html/Condensed_Reviews_Booklet_2014.pdf) [Accessed December 2015].
- [22] K. Freese, B. Fields and D. Graff (2000). [arXiv:0007444 [astro-ph]]
- [23] J. Yoo, J. Chanamé and A. Gould, *ApJ* **601**, 311 (2004). [arXiv:astro-ph/0307437]
- [24] M. Milgrom, *ApJ* **270**, 365 (1983).
- [25] R. H. Sanders, *MNRAS* **363**, 459 (2005). [arXiv:astro-ph/0502222]
- [26] S. S. McGaugh, *Canadian Journal of Physics* **93**, 250 (2015). [arXiv:1404.7525 [astro-ph.CO]]
- [27] G. Servant and T. M. P. Tait, *New Jour. Phys.* **4**, 99 (2002). [arXiv:hep-ph/0209262]
- [28] S. Weinberg, *Phys. Rev. Lett.* **40**, 223 (1978).
- [29] F. Wilczek, *Phys. Rev. Lett.* **40**, 279 (1978).

- 
- [30] S. Dodelson and L. M. Widrow, *Phys. Rev. Lett.* **72**, 17 (1994). [arXiv:9303287 [hep-ph]]
- [31] G. Brooijmans, B. Gripcios, F. Moortgat, *et al.* (2012). [arXiv:1203.1488 [astro-ph]]
- [32] P. Gondolo and G. Gelmini, *Nucl. Phys. B* **360**, 145 (1991).
- [33] Planck Collaboration, P. A. R. Ade, N. Aghanim, *et al.*, *Astron. Astrophys.* **571**, A16 (2014). [arXiv:1303.5076 [astro-ph]]
- [34] Image credit: Max Planck Institute for Physics. [[https://www.mpi-hd.mpg.de/lin/research\\_DM.en.html](https://www.mpi-hd.mpg.de/lin/research_DM.en.html)] (Accessed December 2015).
- [35] D. Akimov, *Nucl. Instrum. Meth. A* **628**, 50 (2011).
- [36] R. Agnese, A. J. Anderson, M. Asai, *et al.*, *Phys. Rev. Lett.* **112**, 241302 (2014). [arXiv:1402.7137 [hep-ex]]
- [37] P. Belli, R. Bernabei, A. Bottino, F. Cappella, R. Cerulli, N. Fornengo and S. Scopel, *Phys. Rev. D* **84**, 055014 (2011). [arXiv:1106.4667 [hep-ph]]
- [38] E. Daw *et al.*, *EAS Publ. Ser.* **53**, 11 (2012). [arXiv:1110.0222 [physics.ins-det]]
- [39] E. Armengaud *et al.* [EDELWEISS Collaboration], *Phys. Lett. B* **702**, 329 (2011). [arXiv:1103.4070 [astro-ph.CO]]
- [40] S. Archambault *et al.*, *Phys. Lett. B* **682**, 185 (2009). [arXiv:0907.0307 [hep-ex]]
- [41] M. Felizardo *et al.*, *Phys. Rev. Lett.* **105**, 211301 (2010). [arXiv:1003.2987 [astro-ph.CO]]
- [42] A. Zani, *Adv. High Energy Phys.* **2014**, 205107 (2014).
- [43] E. Aprile *et al.* [XENON100 Collaboration], *Phys. Rev. Lett.* **109**, 181301 (2012). [arXiv:1207.5988 [astro-ph.CO]]
- [44] K. Abe *et al.* [XMASS Collaboration] (2015). [arXiv:1511.04807 [astro-ph.CO]].
- [45] D. Y. Akimov *et al.*, *Phys. Lett. B* **709**, 14 (2012). [arXiv:1110.4769 [astro-ph.CO]]

- [46] M. Ackermann, A. Albert, B. Anderson, *et al.*, Phys. Rev. D **89**, 042001 (2014).  
[arXiv:1310.0828 [astro-ph.HE]]
- [47] P. Picozza, L. Marcelli, O. Adriani, *et al.*, American Institute of Physics Conference Series, **1166**, 141 (2009).
- [48] A. Morselli, Prog. Part. Nucl. Phys. **66**, 208 (2011).
- [49] R. Abbasi, Y. Abdou, T. Abu-Zayyad, *et al.*, Phys. Rev. D, **85**, 042002 (2012).  
[arXiv:1112.1840 [astro-ph.HE]]
- [50] V. Bertin & ANTARES Collaboration, J. Phys. Conf. Ser. **315**, 012030 (2011).
- [51] T. Saab, “The Dark Secrets of the Terascale (TASI 2011) - Proceedings of the 2011 Theoretical Advanced Study Institute in Elementary Particle Physics,” Edited by M. Konstantin *et al.*, World Scientific Publishing Co. Pte. Ltd., pp. 711-738, **711** (2013).
- [52] LUX Dark Matter, [http://lux.brown.edu/LUX\\\_dark\\\_matter/Home.html](http://lux.brown.edu/LUX\_dark\_matter/Home.html) (Accessed December 2015).
- [53] E. Aprile, A. E. Bolotnikov, A. I. Bolozdynya, & T. Doke, “Noble Gas Detectors,” Weinheim, Germany: WILEY-VCH (2006).
- [54] V. Chepel & H. Araújo, Journal of Instrumentation, **8**, R04001 (2013).  
[arXiv:1207.2292 [physics.ins-det]]
- [55] LUX Collaboration, D. S. Akerib, H. M. Araújo, *et al.* (2015). [arXiv:1512.03506 [astro-ph]]
- [56] LUX Collaboration, D. S. Akerib, H. M. Araújo, *et al.* (2013). [arXiv:1310.8214 [astro-ph]]
- [57] Image credit: NASA/DOE/Fermi LAT Collaboration, <http://fermi.gsfc.nasa.gov/ssc/observations/types/allsky/> (Page accessed: December 2015).
- [58] T. Daylan, D. P. Finkbeiner, D. Hooper, *et al.*, Physics of the Dark Universe, **12**, 1 (2016). [arXiv:1402.6703 [astro-ph]]

- 
- [59] I. Cholis, D. P. Finkbeiner, L. Goodenough & N. Weiner, *JCAP* **12**, 007 (2009).  
[arXiv:0810.5344 [astro-ph]]
- [60] The IceCube Collaboration, M. G. Aartsen, K. Abraham, *et al.* (2015).  
[arXiv:1510.05226 [astro-ph]]
- [61] ANTARES Collaboration, *JCAP* **11**, 032 (2013). [arXiv:1302.6516 [astro-ph]]
- [62] G. Aad, G., T. Abajyan, B. Abbott, *et al.*, *Physics Letters B*, **716**, 1 (2012).  
[arXiv:1207.7214 [hep-ex]]
- [63] S. Chatrchyan, V. Khachatryan, A. M. Sirunyan, *et al.*, *Physics Letters B*, **716**, 30  
(2012). [arXiv:1207.7235 [hep-ex]]
- [64] S. L. Glashow, *Nuclear Physics A*, **22**, 579 (1961).
- [65] S. Weinberg, *Physical Review Letters*, **19**, 1264 (1967).
- [66] A. Salam, N. Svartholm, ed. “Elementary Particle Physics: Relativistic Groups and Analyticity”. Eighth Nobel Symposium. Stockholm: Almquist and Wiksell, 367, (1968).
- [67] S. F. King, *Reports on Progress in Physics*, **67**, 107 (2004). [arXiv:hep-ph/0310204]
- [68] P. Braun-Munzinger, V. Koch, T. Schäfer, & J. Stachel, *Physics Reports*, **621**, 76  
(2016). [arXiv:1510.00442 [nucl-th]]
- [69] F. Englert & R. Brout, *Physical Review Letters*, **13**, 321 (1964).
- [70] P. W. Higgs, *Physical Review Letters*, **13**, 508 (1964).
- [71] G. S. Guralnik, C. R. Hagen, & T. W. Kibble, *Physical Review Letters*, **13**, 585  
(1964).
- [72] Particle Data Group, “Grand Unified Theories” (2011). <http://pdg.lbl.gov/2015/reviews/rpp2015-rev-guts.pdf>
- [73] S. Coleman and J. Mandula, *Phys. Rev.*, **159**, 1251 (1967).
- [74] R. Haag, M. Sohnius and J. T. Lopuszanski, *Nuclear Physics B*, **88**, 257 (1975).

- [75] M. Drees, R. Godbole, & P. Roy, “Theory and Phenomenology of Sparticles,” Hackensack, USA: World Scientific Publishing Company (2004).
- [76] S. P. Martin (1997). [arXiv: hep-ph/9709356]
- [77] R. N. Mohapatra, “Unification and Supersymmetry: The Frontiers of Quark-Lepton Physics,” New York, USA: Springer-Verlag (1986).
- [78] F. Quevedo, S. Krippendorff & O. Schlotterer, (2010). [arXiv:1011.1491 [hep-th]]
- [79] G. F. Giudice & R. Rattazzi, *Physics Reports*, **322**, 419 (1999). [arXiv:hep-ph/9801271]
- [80] L. Randall & R. Sundrum, *Nuclear Physics B*, **557**, 79 (1999). [arXiv:hep-th/9810155]
- [81] S. Dimopoulos & H. Georgi, *Nucl. Phys. B* **193**, 150 (1981).
- [82] K. A. Olive, *Journal of Physics Conference Series*, **315**, 012021 (2011). [arXiv:1009.0232 [hep-ph]]
- [83] S. J. Underwood, J. Giedt, A. W. Thomas, & R. D. Young, *Phys. Rev. D*, **86**, 035009 (2012). [arXiv:1203.1092 [hep-ph]]
- [84] A. Djouadi *et al.*, *JHEP* **0807**, 002 (2008). [arXiv:0801.4321 [hep-ph]]
- [85] U. Ellwanger, C. Hugonie and A. M. Teixeira, *Phys. Rept.* **496**, 1 (2010). [arXiv:0910.1785 [hep-ph]]
- [86] J. R. Ellis, K. A. Olive, Y. Santoso and V. C. Spanos, *Phys. Rev. D* **71**, 095007 (2005). [arXiv:hep-ph/0502001]
- [87] J. R. Ellis, K. A. Olive and C. Savage, *Phys. Rev. D* **77**, 065026 (2008). [arXiv:0801.3656 [hep-ph]]
- [88] M. A. Shifman, A. I. Vainshtein and V. I. Zakharov, *Nucl. Phys. B* **147**, 385 (1979).
- [89] J. Giedt, A. W. Thomas and R. D. Young, *Phys. Rev. Lett.* **103**, 201802 (2009). [arXiv:0907.4177 [hep-ph]]

- 
- [90] R. D. Young and A. W. Thomas, Phys. Rev. D **81**, 014503 (2010). [arXiv:0901.3310 [hep-lat]]
- [91] D. Toussaint and W. Freeman [MILC Collaboration], Phys. Rev. Lett. **103**, 122002 (2009). [arXiv:0905.2432 [hep-lat]]
- [92] A. E. Nelson and D. B. Kaplan, Phys. Lett. B **192**, 193 (1987).
- [93] B. Borasoy and U. G. Meissner, Annals Phys. **254**, 192 (1997). [arXiv:hep-ph/9607432]
- [94] G. Blanger, F. Boudjema, P. Brun, A. Pukhov, S. Rosier-Lees, P. Salati, & A. Semenov, Comput. Phys. Commun. **182**, 842 (2011). [arXiv:1004.1092 [hep-ph]]
- [95] G. W. Bennett *et al.* [Muon G-2 Collaboration], Phys. Rev. D **73**, 072003 (2006). [arXiv:hep-ex/0602035]
- [96] P. E. Shanahan, A. W. Thomas and R. D. Young, Phys. Rev. Lett. **107**, 092004 (2011). [arXiv:1106.2851 [nucl-th]]
- [97] B. Herrmann, PoS **IDM2010**, 123 (2011). [arXiv:1011.6550 [hep-ph]]
- [98] E. Komatsu *et al.* [WMAP Collaboration], Astrophys. J. Suppl. **192**, 18 (2011). [arXiv:1001.4538 [astro-ph.CO]]
- [99] S. Chatrchyan *et al.* [CMS Collaboration], Phys. Rev. Lett. **107**, 221804 (2011). [arXiv:1109.2352 [hep-ex]]
- [100] Y. B. Zel'Dovich, I. Y. Kobzarev, & L. B. Okun', Soviet Journal of Experimental and Theoretical Physics, **40**, 1 (1975).
- [101] K. Hamaguchi, K. Nakayama, & N. Yokozaki, Physics Letters B, **708**, 100 (2012). [arXiv:1107.4760 [hep-ph]]
- [102] J. P. Hall & S. F. King, Journal of High Energy Physics, **1**, 76 (2013). [arXiv:1209.4657 [hep-ph]]
- [103] P. Athron, J. P. Hall, S. F. King, *et al.*, (2011). [arXiv:1109.6373 [hep-ph]]

- [104] P. Athron, S. F. King, D. J. Miller, S. Moretti, & R. Nevzorov, *Journal of Physics Conference Series* **110**, 072001 (2008). [arXiv:0708.3248 [hep-ph]]
- [105] P. Athron, S. F. King, D. J. Miller, S. Moretti, & R. Nevzorov, *Phys. Rev. D.* **80**, 035009 (2009). [arXiv:0904.2169 [hep-ph]]
- [106] P. Athron, S. F. King, D. J. Miller, S. Moretti, & R. Nevzorov, *Physics Letters B* **681**, 448 (2009). [arXiv:0901.1192 [hep-ph]]
- [107] P. Athron, S. F. King, D. J. Miller, S. Moretti, & R. Nevzorov, *Phys. Rev. D.* **84**, 055006 (2011). [arXiv:1102.4363 [hep-ph]]
- [108] J. P. Hall & S. F. King, *Journal of High Energy Physics* **6**, 6 (2011). [arXiv:1104.2259 [hep-ph]]
- [109] P. Athron, D. Harries, R. Nevzorov, & A. G. Williams, (2015). [arXiv:1512.07040 [hep-ph]]
- [110] J. P. Hall, S. F. King, R. Nevzorov, S. Pakvasa, & M. Sher, (2010). [arXiv:1012.5365 [hep-ph]]
- [111] P. Athron, S. F. King, D. J. Miller, S. Moretti, & R. Nevzorov, (2009). [arXiv:0910.0705 [hep-ph]]
- [112] J. P. Hall, S. F. King, R. Nevzorov, S. Pakvasa, & M. Sher, *Phys. Rev. D.* **83**, 075013 (2011). [arXiv:1012.5114 [hep-ph]]
- [113] Planck Collaboration, [[http://planck.caltech.edu/pub/2015results/Planck\\_2015\\_Results\\_XIII\\_Cosmological\\_Parameters.pdf](http://planck.caltech.edu/pub/2015results/Planck_2015_Results_XIII_Cosmological_Parameters.pdf)] (Accessed April 2016)
- [114] K. N. Abazajian, K. Arnold, J. Austermann, J., et al., *Astroparticle Physics*, **63**, 66 (2015). [arXiv:1309.5383 [astro-ph.CO]]
- [115] CMS Collaboration, “Search for a Narrow Resonance Produced in 13 TeV pp Collisions Decaying to Electron Pair or Muon Pair Final States” (2015).
- [116] The ATLAS Collaboration, “Search for new phenomena in the dilepton final state using proton-proton collisions at  $\sqrt{s} = 13$  TeV with the ATLAS detector” (2015).

- 
- [117] P. Athron, J. h. Park, D. Steckinger, & A. Voigt, *Comput. Phys. Commun.* **190**, 139 (2015). [arXiv:1406.2319 [hep-ph]]
- [118] F. Feroz, M. P. Hobson, & M. Bridges, *Mon. Not. Roy. Astron. Soc.* **398**, 1601 (2009). [arXiv:0809.3437 [astro-ph]]
- [119] F. Feroz & M. P. Hobson, *Mon. Not. Roy. Astron. Soc.* **384**, 449 (2008). [arXiv:0704.3704 [astro-ph]]
- [120] F. Feroz, M. P. Hobson, E. Cameron, & A. N. Pettitt, (2013). [arXiv:1306.2144 [astro-ph.IM]]
- [121] F. Staub, *Comput. Phys. Commun.* **185**, 1773 (2014). [arXiv:1309.7223 [hep-ph]]
- [122] B. C. Allanach, *Comput. Phys. Commun.* **143**, 305 (2002) [hep-ph/0104145].
- [123] G. Guennebaud, B. Jacob, *et al.*, Eigen v3 (2010). <http://eigen.tuxfamily.org>
- [124] ATLAS & CMS Collaborations, (2015). [arXiv:1503.07589 [hep-ex]]
- [125] K. A. Olive *et al.* (Particle Data Group), *Chin. Phys. C* **38**, 090001 (2014). [<http://pdg.lbl.gov>]
- [126] ATLAS Collaboration, [arXiv: 1507.05525 [hep-ex]]
- [127] A. C. Kraan, *Fundamental Interactions: Proceedings of the 20th Lake Louise Winter Institute*, **20**, 129 (2006). [arXiv:hep-ex/0505002]
- [128] W. Abdallah & S. Khalil, (2015). [arXiv:1509.07031 [hep-ph]]
- [129] J. Edsjö & P. Gondolo, *Phys. Rev. D*, **56**, 1879 (1997). [arXiv:hep-ph/9704361]
- [130] J. P. Hall & S. F. King, *Journal of High Energy Physics*, **8**, 088 (2009). [arXiv:0905.2696 [hep-ph]]
- [131] T. Han, Z. Liu, & S. Su, *Journal of High Energy Physics*, **8**, 93 (2014). [arXiv:1406.1181 [hep-ph]]
- [132] P. Athron, S. F. King, D. J. Miller, S. Moretti, & R. Nevzorov, *Phys. Rev. D*, **86**, 095003 (2012). [arXiv:1206.5028 [hep-ph]]

- [133] G. Aad, B. Abbott, J. Abdallah, *et al.* Journal of High Energy Physics, **7**, 157 (2015). [arXiv:1502.07177 [hep-ex]]
- [134] E. Aprile, J. Aalbers, F. Agostini, *et al.* Journal of Cosmology and Astroparticle Physics, **4**, 027 (2016). [arXiv:1512.07501 [physics.ins-det]]